
OPTIMAL QUANTUM CONTROL OF ATOMIC WAVE PACKETS IN OPTICAL LATTICES

Dissertation

zur

Erlangung des Doktorgrades (Dr. rer. nat.)

der

Mathematisch-Naturwissenschaftlichen Fakultät

der

Rheinischen Friedrich-Wilhelms-Universität Bonn

vorgelegt von

Natalie Peter

aus

Wiesbaden-Dotzheim

Bonn, 2018

Angefertigt mit Genehmigung der Mathematisch-Naturwissenschaftlichen
Fakultät der Rheinischen Friedrich-Wilhelms-Universität Bonn

- | | |
|-----------------|----------------------------------|
| 1. Gutachter: | Prof. Dr. Dieter Meschede |
| 2. Gutachterin: | Priv.-Doz. Dr. Elisabeth Soergel |

Tag der mündlichen Prüfung:

Erscheinungsjahr: 2019

Manuel und meinen Eltern

Abstract

In this work, I investigate the motional control and the transport of single neutral atoms trapped in an optical conveyor belt. The main goal is to prepare the atoms in the vibrational ground state of the trapping potential with high efficiency and keep the atoms in this state after fast non-adiabatic transport. In this group, the conveyor belt is used in two systems: (i) In an atom-cavity system, the three-dimensional ground state is prepared by means of carrier-free Raman sideband cooling for the first time. (ii) I use one-dimensional microwave sideband cooling in a state-dependent optical lattice and analyze with a new temperature model the influence of the anharmonic shape of the trapping potential. In the next step, I present a numerical simulation of atom transport. Optimal quantum control theory is used to find transport sequences for different durations without heating atoms out of the ground state. The measurements with these new sequences demonstrate that atoms can be transported by a factor two faster, with higher fidelity and robustness against experimental imperfections. Additionally, I analyze the dynamics of atom transport for sequences of multiple transport steps, which are required for quantum walk experiments. A proof-of-principle measurement demonstrates open-loop live feedback optimization of transport sequences with the experiment. This technique can further compensate experimental imperfections that are not taken into account in the numerical calculation. In the last part, I examine the fundamental limit of fast atom transport, the so-called quantum speed limit. It is defined as the minimum time that a quantum state requires to evolve into an orthogonal one. I investigate the dependencies of this boundary on different trap depths and the finite radial temperature.

CONTENTS

| | | |
|-----|--|----|
| 1 | INTRODUCTION | 7 |
| 2 | SINGLE ATOMS IN A DIPOLE TRAP | 11 |
| 2.1 | Cooling atoms from a thermal background gas | 11 |
| 2.2 | Neutral atoms in a conveyor belt dipole trap | 14 |
| 3 | CAVITY ELECTRODYNAMICS WITH NEUTRAL ATOMS | 17 |
| 3.1 | Atom-cavity experimental system | 17 |
| 3.2 | Non-destructive state detection using an optical cavity | 19 |
| 4 | THREE-DIMENSIONAL RAMAN GROUND STATE COOLING INSIDE A CAVITY | 23 |
| 4.1 | Fundamentals of Raman sideband cooling | 24 |
| 4.2 | Raman laser system | 29 |
| 4.3 | Three-dimensional carrier-free Raman sideband cooling | 31 |
| 4.4 | Conclusion | 39 |
| 5 | STATE-DEPENDENT LATTICE TRANSPORT WITH NEUTRAL ATOMS | 41 |
| 5.1 | Atom transport | 41 |
| 5.2 | State-dependent lattice | 42 |
| 5.3 | Atom loading and state manipulation | 44 |
| 5.4 | Experimental setup of the state-dependent lattices | 46 |
| 5.5 | Phase and intensity control systems | 48 |
| 6 | MICROWAVE SIDEBAND COOLING OF NEUTRAL ATOMS | 53 |
| 6.1 | Fundamentals of microwave sideband cooling in a state-dependent lattice | 53 |
| 6.2 | One-dimensional temperature model | 55 |
| 6.3 | Measurement of one-dimensional microwave ground state cooling . . | 57 |
| 6.4 | Conclusion and outlook | 59 |
| 7 | OPTIMAL QUANTUM CONTROL FOR FAST ATOM TRANSPORT | 61 |
| 7.1 | The transport of an atomic wave packet in optical lattices | 62 |
| 7.2 | Theoretical model of the transport fidelity | 64 |
| 7.3 | Measurement of the transport fidelity | 67 |

| | | |
|-------|--|-----|
| 7.4 | Optimal control theory for high transport fidelity | 69 |
| 7.5 | Measurement of optimal control transport | 75 |
| 7.6 | Multiple step optimal control transport | 79 |
| 7.7 | Live optimal control | 83 |
| 7.8 | Conclusion | 86 |
| 8 | THE QUANTUM SPEED LIMIT | 87 |
| 8.1 | Quantum speed limit of atom transport | 88 |
| 8.2 | Direct vibrational state detection scheme | 93 |
| 8.3 | Conclusion | 98 |
| 8.4 | Outlook: Quantum speed limit of a static system | 99 |
| 9 | CONCLUSION | 103 |
| A | APPENDIX | 105 |
| A.1 | State-dependent lattice potential of the $ \downarrow\rangle$ -state | 105 |
| A.1.1 | Calculation of $\{U^\downarrow, \varphi^\downarrow\}$ from $\{U^{\sigma^-}, \varphi^{\sigma^-}\}$ and $\{U^{\sigma^+}, \varphi^{\sigma^+}\}$ | 105 |
| A.1.2 | Iterative approach to derive $\{U^{\sigma^-}, \varphi^{\sigma^-}\}$ from $\{U^{\sigma^+}, \varphi^{\sigma^+}\}$ | 106 |
| A.2 | Wannier states and eigenenergies of a standing wave potential | 108 |
| A.3 | Symmetries of optimal control transport | 111 |
| A.3.1 | Time-reversal invariance | 111 |
| A.3.2 | Ramp symmetry and $\hat{P}\hat{\Theta}\hat{T}$ invariance | 112 |

CHAPTER 1

INTRODUCTION

The simulation of quantum systems on conventional computer often fails, since the complexity scales exponentially with the dimension of the Hilbert space [1]. To overcome this, Feynman proposed to operate a quantum system instead that intrinsically follows the laws of quantum mechanics [2]. The field of quantum simulations explores quantum effects of materials of fundamental or technical interest, such as solid-state topological insulators [3], by investigating model systems, such as cold atoms in optical lattices [4]. In these systems a mathematically equivalent Hamiltonian can be engineered, but with much better controllability and measurability of all parameters. Since there is still no universal quantum simulator, various quantum systems are proposed to investigate different aspects and regimes. A commonly used platform is the field of quantum optics.

Photons offer the unique property of being mobile over free space or optical waveguides, and low decoherences due to their weak interactions with the environment. They can be controlled by an uncomplicated architecture through the use of well-developed components at room temperature. Therefore, they are well suited to transport quantum information and interconnect different platforms [5]. Coupled to a form a matter, a quantum simulator can be built. The quantum particles in these simulators are represented by neutral [6] or charged atoms [7] in traps and cavity systems, circuit excitations in superconducting circuits [8], Josephson junctions [9] on cavity optomechanical systems [10], nitrogen-vacancy centers in diamonds [11], or semiconductor quantum dots [12]. In order to study the interaction between particles, they have to be well isolated from the environment. In case of single atoms, they are placed in ultra-high vacuum with typical pressures down to 10^{-11} mbar. The interactions can be tuned by the coupling strength with photon fields. In contrast, the nature of nanofabricated systems, such as superconducting circuits allows a high flexibility of interactions strengths with lithographic techniques. The complete wavefunction of a few-body system can be determined. In order to describe the dynamics of a many-body systems, one typically analyzes certain physical properties like densities, magnetization per

lattice site or few-body correlations instead [13]. In general, a quantum simulator should be able to prepare a known quantum state, to engineer a series of interactions with external fields or between constituents with adjustable values and to provide a reproducible detection scheme.

Ground state cooling of single neutral atoms in a lattice

Unlike ion traps, which use the strong Coulomb interaction with an electromagnetic field [14, 15], the confinement of neutral atoms in space is controlled by much weaker dipole interactions. In the last decades, three main types of trapping techniques have been developed for neutral atoms: The radiation-pressure traps utilize the effect of strong photon scattering of near-resonant light [16, 17]. The strong dissipation allows the cooling and accumulation of atoms from a thermal gas. These traps are well suited to initially collect cold atoms. However, in order to isolate single atoms and to manipulate their internal state, typically magnetic [18] and optical dipole [19] traps are used, which do not continuously scatter photons and thus do not decohere the internal and oscillatory states of the atoms. These traps are based on the interaction between the magnetic or electric dipole moment of the atom and an inhomogeneous magnetic or electric field. For example, magnetic traps are used for evaporative cooling [20] of atomic clouds towards Bose-Einstein condensation [21]. The optical dipole trap offers a mostly state-independent trapping mechanism and leaves the internal dynamics of the atom almost undisturbed [22].

The vibrational ground state marks the quantum-mechanically lowest energy state of a tightly bound atom. As part of the preparation of a well-defined initial quantum states, I have investigated two different methods for cooling neutral atoms to the oscillatory ground state of optical potentials: Microwave and Raman sideband cooling. Raman sideband cooling is much broader applicable, and I demonstrate three-dimensional ground state cooling in a high-finesse optical cavity system. In case a blue-detuned dipole trap is used, the cooling efficiency can be increased by a carrier-free sideband cooling technique. Microwave sideband cooling is the simpler and more robust method, but it requires a state-dependent displacement of the trapping potential. I use a one-dimensional state-dependent optical lattice and analyze with a new model the influence of the anharmonic shape of the trapping potential.

Optimal control of atom transport

The number of coherent quantum operations in our systems are limited by the coherence time divided by the amount of time each operation lasts. There are two

ways to increase this number: First, the coherence time can be improved by reducing noise sources. In this work, I demonstrate the second approach of reducing the time of an operation down to the fundamental limit through optimal control theory. In case of quantum walk experiments with atoms in a state-dependent lattice, the coherent operations are coin and shift operations. The coin operation creates a superposition of the internal states of the cesium atoms. The shift operation is the coherent, state-dependent transport and thus a delocalization of different parts of the atomic wavefunction. In order to observe the interference of the spreading wave packet in position space, it is necessary, that no vibrational excitations are introduced by the quantum transport. In the past, we used a simple non-adiabatic linear transport scheme [23]. A sudden acceleration at the beginning excites the atom into a coherent state. The atom is relaxed into the initial state at the end of the transport, if the transport time is chosen an integer multiple of the atom oscillation period in transport direction. With precise knowledge of the system parameters and dynamics, an advanced transport method can be developed. Together with the high controllability of the system [24] we can use optimal control theory to generate more complex transport sequences with significantly higher transport fidelities and shorter transport durations. I present two measurement techniques to determine the ground state population before and after transport, which defines the transport fidelity. Furthermore, I characterize the robustness of the new transport ramps and verify the dependency on the trapping potential and the spin state. Finally, I investigate the fundamental minimum time for the shift operation, which is the so-called quantum speed limit.

CHAPTER 2

SINGLE ATOMS IN A DIPOLE TRAP

Laser cooling and positional control of atoms is an essential requirement for experiments studying isolated neutral atoms in an optical dipole trap on a time scale of seconds. Since the main goal of this work is the investigation of isolated neutral atoms in optical lattices, a fundamental understanding of those crucial components is necessary. Preceding experiments on cooling and positional control of atoms have laid a solid basis for my work. The necessary condition for the experiments is reached by the commonly used magneto-optical trap (MOT) in combination with the conveyor belt dipole trap, a technique pioneered in this group [25].

2.1 Cooling atoms from a thermal background gas

Cesium atoms

In my experiments, cesium atoms are used to study light-matter interaction. Several advantages favor the choice of this atom for quantum optics: the availability of laser diodes with the appropriate wavelength, a sufficient vapor pressure at room temperature and a well accessible hyperfine splitting between two ground states in the microwave regime [26], which is used in frequency standards.

In 1860 cesium was discovered by R. Bunsen and G. Kirchhoff. The name of this alkali metal originates from the blue color during flame spectroscopy (latin: caesius = bluish-gray) [27]. Already in 1897, P. Zeeman discovered the spectral line splitting in alkali metals in the presence of a static magnetic field [28]. The outermost of those Zeeman states of the hyperfine ground states are used for the measurements in this work. The quantum number of the hyperfine states is depicted with F and the quantum number of the corresponding Zeeman states with m_F . In Fig. 2.1 the states with a hyperfine splitting of $2\pi \cdot 9.2$ GHz [26] used in the two experiments are sketched. Since the outermost Zeeman states of

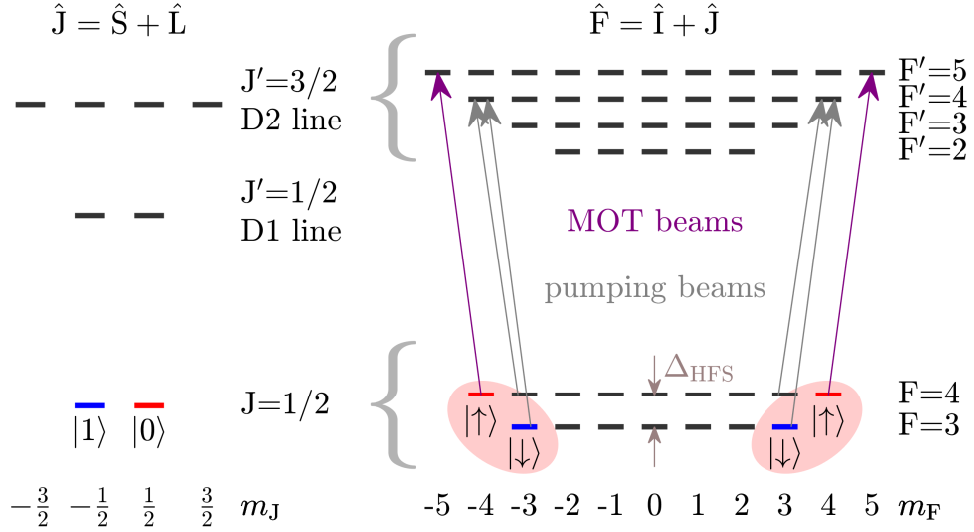


Figure 2.1: Level scheme of cesium: The fine structure shows the ground state $L = 0$ ($J = 1/2$) and the first excited state $L = 1$ ($J' = 1/2$ and $J' = 3/2$). In the hyperfine structure representation, the outermost Zeeman states form a quasi two-level system with a hyperfine splitting Δ_{HFS} of $2\pi \cdot 9.2$ GHz. For the state-dependent lattice we use the states $|\downarrow\rangle = |F = 3, m_F = +3\rangle$ and $|\uparrow\rangle = |F = 4, m_F = +4\rangle$. It is equally possible to use the $|\downarrow\rangle = |F = 3, m_F = -3\rangle$ and $|\uparrow\rangle = |F = 4, m_F = -4\rangle$ states, which is applied in the atom-cavity experiment. The choice of the Zeeman states decides, which polarization of the MOT and pumping beams has to be used. The purple arrows indicate the closed cycling transition with the state $|F' = 5, m_F = +5 \text{ or } -5\rangle$ of the D2 line for atom trapping and molasse cooling. The pumping beams (gray) for state preparation couple all states $|F = 3 \text{ or } 4\rangle \rightarrow |F' = 4\rangle$ (here exemplarily shown only for the outermost states).

a hyperfine state have the same coupling efficiency, it is equally possible to choose the left or right states. In particular, we use:

- for the state-dependent lattice the right states:
 $|\downarrow\rangle = |F = 3, m_F = +3\rangle$ and $|\uparrow\rangle = |F = 4, m_F = +4\rangle$
- for the atom-cavity experiment the left states:
 $|\downarrow\rangle = |F = 3, m_F = -3\rangle$ and $|\uparrow\rangle = |F = 4, m_F = -4\rangle$.

These Zeeman sublevels are tunable with an external magnetic field. Following the selection rules, the $|\uparrow\rangle$ -state forms a closed cycling transition with the excited state $|F' = 5, m_F = +5\rangle$ or $|F' = 5, m_F = -5\rangle$, respectively, of the D2-line and can consequently be treated as a quasi-two-level atomic system. The $|\uparrow\rangle$ -state is

prepared with high efficiency of $> 99\%$ [29] with the help of a repumping beam on the $|F = 3\rangle \rightarrow |F' = 4\rangle$ transition and an optical pumping beam on the $|F = 4\rangle \rightarrow |F' = 4\rangle$ transition, both σ -polarized as shown in Fig. 2.1. The choice of the Zeeman states decides, which polarization of the MOT beams, pumping beams and further auxiliary fields has to be used. The $|\downarrow\rangle$ -state can be initialized with a coherent state transfer on the hyperfine transition with an efficiency up to 98% [30].

MOT

As a first cooling step, our experiments use the robust technique of a magneto-optical trap (MOT) to cool cesium atoms from a thermal background gas. A building block of the MOT is the molasse cooling as proposed by Hänsch and Schawlow [16]. In each direction a pair of counter-propagating laser beams is locked to the crossover signal $|F = 4\rangle \rightarrow |F' = 3\rangle \times |F' = 5\rangle$ by Doppler-free laser polarization spectroscopy [31] and shifted with an acousto-optic modulator (AOM) close to the $|F = 4\rangle \rightarrow |F' = 5\rangle$ transition as shown in Fig. 2.1. The laser beam is red-detuned by a few multiples of the natural linewidth of the excited state $\Gamma_{D2} = 2\pi \cdot 5.2$ MHz. Due to the Doppler shift, the scattering probability is strongest for the beam counter-propagating the atoms' movement. Since the photons are scattered in arbitrary direction, the net momentum transfer of many scattering events damps the atomic motion. For cesium atoms this technique is limited by the Doppler temperature of $T_D = \hbar\Gamma_{D2}/(2k_B) = 125\ \mu\text{K}$, with the Boltzmann constant k_B . However, off-resonant scattering and polarization impurities of the MOT beams can pump the atoms from $|F = 4\rangle \rightarrow |F' = 4\rangle \rightarrow |F = 3\rangle$ out of the cooling cycle. In the presence of the repumping beam on the $|F = 3\rangle \rightarrow |F' = 4\rangle$ transition, the atoms are pumped back into the $|\uparrow\rangle$ -state.

The optical molasse can be extended to a magneto-optical trap by using circularly polarized molasse beams and a quadrupole field to obtain a position-dependent Zeeman splitting [17]. The introduced force towards the zero field position strongly confines the atoms to several tens of micrometers. The atom loading time, which is the operating time of the MOT, of a few seconds is a trade off between a high number of trapped atoms and the shortest time possible in order to reduce the total measurement time. Additional polarization gradient cooling [32] lowers the temperature below the Doppler cooling limit to around $T_{SD} = 10\ \mu\text{K}$. After a desired number of atoms is trapped, the MOT is switched off and the atoms are released with nearly 100% efficiency into the standing wave potential of around $k_B \cdot 400\ \mu\text{K}$ depth.

2.2 Neutral atoms in a conveyor belt dipole trap

Standing wave conveyor belt

The atoms cooled down by the MOT are to be transferred into an optical conveyor belt dipole trap. The idea of an isolating periodic crystal-like potential structure was realized for neutral atoms by Anderson in the form of a non-dissipative optical lattice [22]. This static dipole trap was further developed in this group to a conveyor belt to transport atoms over macroscopic distances.

Two counter-propagating laser beams form a standing wave potential. The frequency of the laser beams ω_{DT} is detuned from the atomic resonance ω_0 . The detuning $\Delta = \omega_{\text{DT}} - \omega_0$ reduces the scattering forces. They scale with $1/\Delta^2$ [33] and subsequently are dominated by the dipole force, which scales with $1/\Delta$. The dipole force between the induced electric dipole moment $\hat{\mathbf{d}}$ of a neutral atom and the electric field \mathbf{E} of the optical lattice results in a spatially varying energy shift, the so-called ac-Stark shift. The dipole potential U_{DT} of the ground state $|g\rangle$ is the sum of the contributions of all coupled excited states $|e_i\rangle$

$$U_{\text{DT}}(\rho, z_{\text{DT}}) = \sum_i \frac{|\langle g | \hat{\mathbf{d}} \mathbf{E} | e_i \rangle|^2}{\hbar \Delta} \quad , \quad (2.1)$$

$$\mathbf{F}_{\text{DT}}(\rho, z_{\text{DT}}) = -\nabla U_{\text{DT}}(\rho, z_{\text{DT}}) \quad ,$$

with the dipole operator $\hat{\mathbf{d}}$ and cylindric coordinates ρ and z_{DT} , where z_{DT} corresponds to the beam axis. Depending on the detuning Δ the atoms experience an attractive or repulsive force \mathbf{F}_{DT} . It is necessary to operate at least one red-detuned dipole trap ($\Delta < 0$), in which the atoms are trapped in the intensity maximum. Additional traps are most beneficial blue-detuned, since the atoms are trapped in an intensity minimum, which reduces the heating by photon scattering. In order to avoid interference between different dipole traps, they are decoupled in frequency or polarization.

The electric field of two counter-propagating laser beams is given by the sum of its components and the polarization unit vector $\boldsymbol{\epsilon}$:

$$\mathbf{E} = \frac{1}{2} \boldsymbol{\epsilon} (E_1 e^{i(k_1 z_{\text{DT}} - \omega_1 t + \varphi)} + E_2 e^{i(-k_2 z_{\text{DT}} - \omega_2 t)} + c.c.) e^{-\rho^2/w(z_{\text{DT}})^2} \quad , \quad (2.2)$$

with the wavenumber $k_j = \frac{2\pi}{\lambda_j}$, wavelength λ_j , the electric field amplitude E_j , the frequency ω_j and the Gaussian beam radius $w(z_{\text{DT}})$. The index j refers to the respective laser beam. In the static dipole trap the laser beams are not detuned such that $k = k_1 = k_2$ and $\omega_{\text{DT}} = \omega_1 = \omega_2$. The relative phase between the counter-propagating laser beams is depicted by φ . A sinusoidal lattice potential

with the intensity $I(t) = c\epsilon_0 \mathbf{E}^2/2$, with the electric constant ϵ_0 and a damping rate Γ is formed:

$$\begin{aligned} U_{\text{DT}}(\rho, z_{\text{DT}}) &\approx \frac{3\pi c^2}{2\omega_0^3} \frac{\Gamma}{\Delta} I(t) \\ &= U \cos^2((kz_{\text{DT}} - \varphi)/2) e^{-2\rho^2/w^2} . \end{aligned} \quad (2.3)$$

To keep atoms as long as possible in the trap, the noise is reduced by an intensity stabilization. In the harmonic approximation, the trapping frequency along the beam direction depends only on the effective trap depth amplitude U and the mass of the cesium atom m_{Cs} :

$$\Omega_{\text{trap}} = 2\pi \sqrt{\frac{2U}{m_{\text{Cs}}\lambda_{\text{DT}}^2}} . \quad (2.4)$$

In the experiments presented in the following, the trapping frequencies are in the order of 2π (100 – 400) kHz. Along the radial direction ρ , the atoms are weaker confined. The radial trapping frequency is given by:

$$\Omega_{\text{rad}} = \sqrt{\frac{4U}{m_{\text{Cs}}w_{\text{DT}}^2}} . \quad (2.5)$$

For the dipole traps used in this work, the radial trapping frequency is two orders of magnitude smaller than Ω_{trap} . The derived potential describes the trapping behavior of the static standing-wave dipole trap.

In order to transport atoms with the lattice, either a frequency difference $\Delta\omega_1$ or phase difference $\varphi(t)$ between the two counter-propagating laser beams has to be introduced. This way a moving standing wave is produced, which acts as a well controllable conveyor belt for the atoms. The initial position of the atoms in the trap is determined from a CCD camera image. Depending on the chosen parameters of the laser beams, we can generate two special kinds of conveyor belts: a state-dependent lattice is used in the corresponding experiment and a state-independent conveyor belt is used in the atom-cavity experiment.

CHAPTER 3

CAVITY ELECTRODYNAMICS WITH NEUTRAL ATOMS

Cavity electrodynamics describes the interaction between matter and photons inside a cavity. Optical cavity platforms realize a textbook-like situation to study properties of light-atom interactions [34] or other quantum systems, such as quantum dots [35], silicon-vacancy centers [36] or carbon nanotubes [37]. A single or a few atoms are placed at rest between two highly reflective mirrors. The Purcell effect can enhance or suppress radiative decay of the atom into the cavity mode. The strong coupling regime, where the interaction dominates loss channels, allows the study of fundamental phenomena in a cavity, such as the generation of single photons [38] and quantum logic gates [39].

A deeper understanding of the single cavity system is necessary, to use it as a building block for a quantum computing architecture. Cavity systems are well suited as such a building block, since it is an atom-photon quantum interface. A scalable quantum computing architecture could use individual atoms at rest inside an optical cavity as quantum memories and single flying photons as an interconnection [40–42]. A second potential application is quantum cryptography. Long-distance quantum cryptography and networks promise high security and efficient algorithms. In order to prevent the loss of information that is carried by photons in fibers, a quantum repeater formed by an optical cavity is proposed [43].

In my work, I extend an existing, well-studied cavity experiment with neutral atoms, which I briefly introduce in this chapter. Details on this setup can be found in earlier theses [44–47].

3.1 Atom-cavity experimental system

The experiment shown in Fig. 3.1 uses a red-detuned state-independent conveyor belt to transport atoms from the position of a magneto-optical trap inside an optical high-finesse cavity. The red-detuned trap is formed by a Nd:Yag laser with a frequency of 1032 nm. It is so far detuned that the transport is independent of the

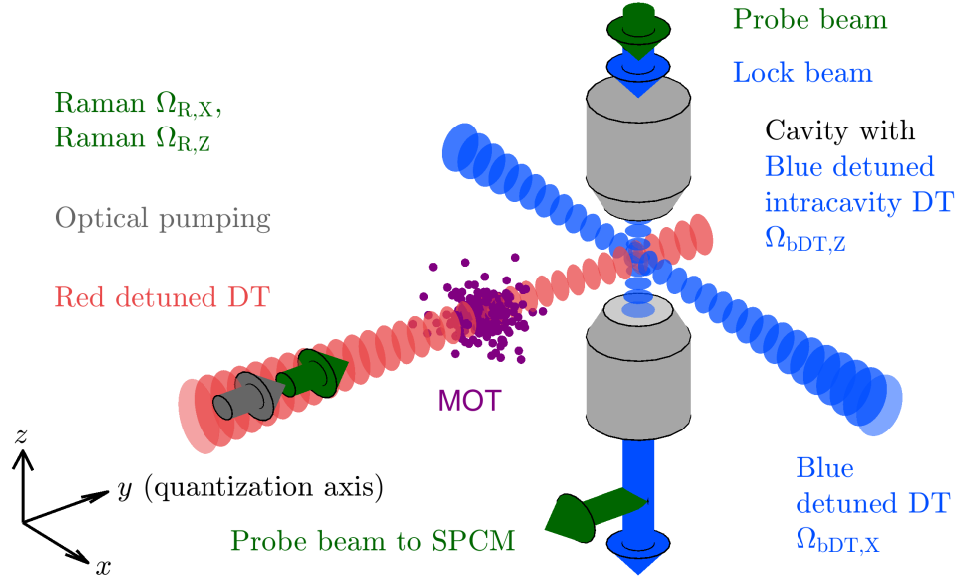


Figure 3.1: Illustration of the atom-cavity experimental system: A single atom is transported in a conveyor belt (red-detuned dipole trap) from the MOT into a high-finesse optical cavity. Inside the cavity, the atom is tightly confined in all three dimensions by two additional blue-detuned dipole traps. An atom in the $|\uparrow\rangle$ -state strongly interacts with the intra-cavity field generated by a $(\sigma^+ + \sigma^-)$ -polarized probe beam. In the strong coupling regime, it suppresses the probe transmission, which is detected with a single photon counting module (SPCM). The non-destructive hyperfine state detection is based on mapping the $|\downarrow\rangle$ - or $|\uparrow\rangle$ -state onto the high or low probe transmission without destroying the state.

two ground states $|\uparrow\rangle$ and $|\downarrow\rangle$. It allows controllable placement of the atom in the center of the cavity mode with submicrometer precision [48]. Inside the resonator, two additional blue-detuned dipole traps with a wavelength of 845.5 nm create a three-dimensional lattice. It confines the atoms to a region of about 100 nm radius in each lattice site. A summary of the trap parameters is given in Tab. 3.1.

The cavity in our laboratory consists of a pair of polished mirror substrates with highly reflective coatings resulting in a finesse of 10^6 . The distance between the mirrors of $160\ \mu\text{m}$ is actively stabilized with a lock laser. The fundamental cavity mode has a waist of $23\ \mu\text{m}$ and the maximum coupling strength describing the atom-cavity interaction is $g = 2\pi \cdot 8\ \text{MHz}$. It is larger than the two loss channels: the cavity field decay rate is $\kappa = 2\pi \cdot 0.4\ \text{MHz}$ and the atomic dipole decay rate is $\gamma = 2\pi \cdot 2.6\ \text{MHz}$. Thus the cavity system operates in the so-called strong coupling regime. In this domain, a reversible transfer of quantum states is enabled between atoms and photons in the cavity mode. Already the interaction of a single atom

| Setup | | Atom-cavity setup | | | |
|-----------------------|------------------------|----------------------|------|-------|----------------------------------|
| Direction | | x | y | z | |
| Trap wavelength | λ_{DT} | 845.5 | 1032 | 845.5 | nm |
| Detuning from D2 line | Δ_{R} | +3 | -60 | +3 | $2\pi \cdot \text{THz}$ |
| Trapping frequency | Ω_{trap} | 114 | 360 | 180 | $2\pi \cdot \text{kHz}$ |
| Lamb-Dicke parameter | η | 0.14 | 0.06 | 0.10 | |
| Trap depth | U | 74 | 1103 | 185 | $k_{\text{B}} \cdot \mu\text{K}$ |
| Waist | w_{DT} | 48 | 33 | 23 | μm |
| Powers | P_{DT} | 18 | 2000 | 10 | mW |

Table 3.1: Summary of the trap properties in the atom-cavity system. In the cavity experiment a three-dimensional spin-independent trap of one red dipole trap in y -direction for transport and two static blue-detuned traps for strong confinement are used.

with the cavity mode field changes significantly the system's properties. As an example, the cavity transmission of this system is sketched in Fig. 3.2 (a). Here a numerical calculation shows that the transmission peak of an empty cavity is shifted significantly in frequency, even with a single coupled atom.

3.2 Non-destructive state detection using an optical cavity

To get information about conducted experiment, we detect the quantum state of the atom inside the cavity. The detection of a quantum state should be fast, with low atom losses and a high detection fidelity. In general, there are several techniques that could be employed:

(i) The state-dependent fluorescence detection is based on different laser-induced scattering rates of the qubit states [49, 50]. Typical fluorescence collection efficiencies of a few percent require a large number of scattering events and result in high detection efficiencies of 99.99 % within $145 \mu\text{s}$ [51]. The energy gained from the process of photon recoil is a negligible heating effect for ions in such deep traps. However, neutral atoms confined in optical dipole traps suffer from atom loss before recording a sufficient number of scattered photons. In order to keep the atoms trapped, lower detection efficiencies and longer readout times must be accepted. With the help of high numerical aperture lenses, readout efficiencies of 98.6 % in 1.5 ms [50] and 95 % in $300 \mu\text{s}$ [49] were obtained.

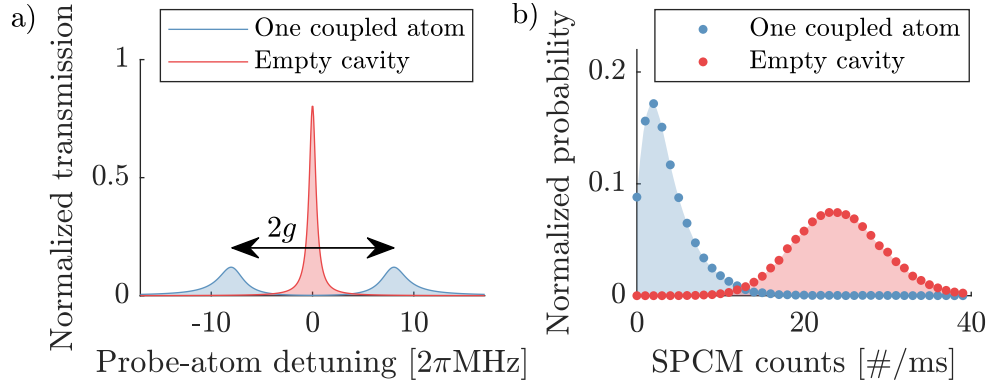


Figure 3.2: Modified cavity transmission in the strong-coupling regime: (a) In the strong coupling regime a coupling-induced normal-mode splitting occurs already for one intra-cavity atom in the weak excitation regime (numerical calculation with our system parameters). (b) The measurement of the cavity transmission detected by the SPCM shows, that we can distinguish between a coupled and empty cavity with a detection fidelity of 98.5 %. The transmission is the same for an uncoupled atom in the cavity or an empty cavity.

(ii) An alternative is the state-selective push-out followed by fluorescence imaging with high detection efficiencies of $> 99\%$ in 500 ms [52]. This destructive method is not a good choice for our single atom experiments with atom loading times of several seconds.

(iii) The cavity offers another more efficient and faster state detection technique without atom loss and high fidelities up to 99.4 % in $85\mu\text{s}$ [53]. The main idea is to map the internal state onto the cavity transmission signal while preserving the internal state of the atom. Our system is designed such that the $|\uparrow\rangle$ -state is strongly interacting while the $|\downarrow\rangle$ -state stays unaffected by the intra-cavity field. The empty optical cavity is resonant to a weak probe laser beam with frequency ω_p and the $|F = 4\rangle \rightarrow |F' = 5\rangle$ transition of the atom. The absolute frequency of the probe beam is stabilized to a cesium transition by polarization spectroscopy with a cesium vapor cell [31] and forms the intra-cavity field as shown in Fig. 3.1. The light behind the cavity is measured with a single photon counting module (SPCM, Perkin Elmer SPCM-AQRH-13) and set to a count rate of $R_{\text{bright}} = 25\text{ kHz}$ as demonstrated in Fig. 3.2 (b). The probability of having zero or one photon in the cavity mode is 98%. Due to selection rules, the $|\downarrow\rangle$ -state does not couple to the cavity mode and the count rate is indistinguishable from an empty cavity. However, the coupling of the $|\uparrow\rangle$ -state with the intra-cavity field dispersively shifts the cavity resonance frequency by several cavity linewidths 2κ as depicted in Fig. 3.2 (a). The atom-cavity system is shifted out of resonance and the probe laser is not transmitted through the cavity. The SPCM count rate of the probe laser reduces

to $R_{\text{dark}} = 2$ kHz. Since the distinguishability between one or more coupled atoms to the cavity is very low in this regime, the measurements are triggered, when a single atom is detected in the MOT by fluorescence counting with an avalanche photodiode.

After each measurement, the presence of an atom inside the cavity is verified for postselection. For that purpose, the σ^- -polarized repumping beam keeps the atom in the coupled $|\uparrow\rangle$ -state to distinguish between a coupled system and an empty cavity through the probe transmission. Efficient control of the vibrational degree of freedom of trapped neutral atoms is crucial to ensure long lifetimes in the trap and stable position-dependent coupling to the cavity field mode. The atom-cavity detuning is chosen to be $\Delta_{\text{ac}} = \omega_0 - \omega_c = 20$ MHz, which allows additional sub-Doppler Sisyphus-like cavity cooling [54] with a temperature of $T_{\text{SD}} = 45 \mu\text{K}$. The atoms are stored in the cavity for seconds. In the next chapter, I describe in detail further cooling by means of carrier-free Raman sideband cooling into the vibrational ground state of the trapping potential, which defines the lowest energy state.

CHAPTER 4

THREE-DIMENSIONAL RAMAN GROUND STATE COOLING INSIDE A CAVITY

Control over the vibrational degree of freedom is crucial for neutral atom experiments to allow for optimal localization, reproducibility of indistinguishable states, stable qubit manipulation and high atomic densities. The lowest temperatures of trapped atoms are achieved by evaporative cooling to sub micro-Kelvin temperatures, which opens the rich field of Bose-Einstein condensation [55]. While this technique is well suited for large atomic ensembles, single atom experiments require other methods with less atom losses. A widely used approach is the sideband cooling method, which was first demonstrated with ions in the so-called resolved sideband regime due to the macro-motion of the atom in the trap [56]. Strongly confined atoms are laser or microwave cooled within milliseconds and brought into their vibrational ground state.

Two main techniques have evolved in the recent decades: microwave and Raman sideband cooling. (i) Microwave sideband cooling is the more robust cooling method with less effort in maintenance, but it requires a spatial displacement of the atomic state during the transition. This displacement has already been demonstrated in experiments such as state-dependent lattices in a relative shift of different lattices [57, 58] or nanofiber-trapped atoms with a Zeeman state dependent displacement from the trap minimum by inhomogeneous magnetic fields [59]. In our cavity experiment, the microwave field is not recommended because it interferes with the sensitive cavity lock. The microwave radiation interacts with electrical components, such as the shear-piezoelectric transducers, which stabilizes the cavity length. (ii) Raman sideband cooling allows for higher coupling strengths in the MHz regime. Furthermore, Raman beams can be more easily extended to three dimensions and generalized to different ion or atom species compared to microwave sideband cooling [60–62].

I demonstrate three-dimensional carrier-suppressed Raman ground state cooling

as an expansion of the cavity experiment described in chapter 3. First, I present the concept of Raman sideband cooling and the already existing realization of the Raman laser system. In the second part, I describe the principle of two-dimensional carrier-free Raman cooling. It is optimized for setups with restricted optical access by using a minimal number of additional Raman lasers. A second refinement of this technique is the use of the present blue-detuned dipole traps as Raman beams, which suppresses the carrier transition and results in a five times lower fundamental temperature limit [63]. In this work, I extend this scheme to three dimensions with minimal additional resources.

4.1 Fundamentals of Raman sideband cooling

In the optical regime two laser beams stimulate the electric dipole transition of the ground states $|\uparrow\rangle$ and $|\downarrow\rangle$ to the same excited state as shown in Fig. 4.1 (a). The electric field of those so-called Raman beams \mathbf{E}_R couples to the electric dipole moment $\hat{\mathbf{d}}$ of the atom [64] via an intermediate virtual state. The virtual state is separated from the D2 line by a detuning Δ_R . The detuning is much larger than the atomic linewidth of the excited states and the Rabi frequencies Ω_{bDT} and Ω_{Raman} of the single-photon transitions. The frequency difference between the lasers is chosen according to the hyperfine splitting of the ground states. The population in the excited state is negligible and can be mathematically eliminated. The system is approximated to an effective two-level system with the bare two-photon coupling strength $\Omega_0 = \Omega_{\text{bDT}}\Omega_{\text{Raman}}/(2\Delta_R)$. During the transition, a photon is scattered from one laser beam into the other Raman beam. This two-photon method can drive an efficient population transfer between states even though the single-photon electric dipole transition is forbidden. The strength of this effective coupling between the ground states is characterized by the atomic transition Hamiltonian \hat{H}_{F,m_F} :

$$\hat{H}_{F,m_F} = \hat{\mathbf{d}}\mathbf{E}_R. \quad (4.1)$$

In order to conduct Raman spectroscopy, one Raman beam is additionally detuned by the two-photon detuning δ_R . The basic transition with $\delta_R = 0$ is called the carrier transition.

The temperature of the atom in a sinusoidal lattice potential as defined in eq. (2.3) is determined by the occupation of the vibrational states. In order to determine the eigenenergies E_n and eigenstates $|n\rangle$, where n defines the vibrational quantum number for each direction, the one-dimensional stationary Schrödinger equation is solved

$$\hat{H}|n\rangle = \left(\frac{\hat{\mathbf{p}}^2}{2m_{\text{Cs}}} + U \cos^2(kz_{\text{DT}}) \right) |n\rangle = E_n |n\rangle \quad . \quad (4.2)$$

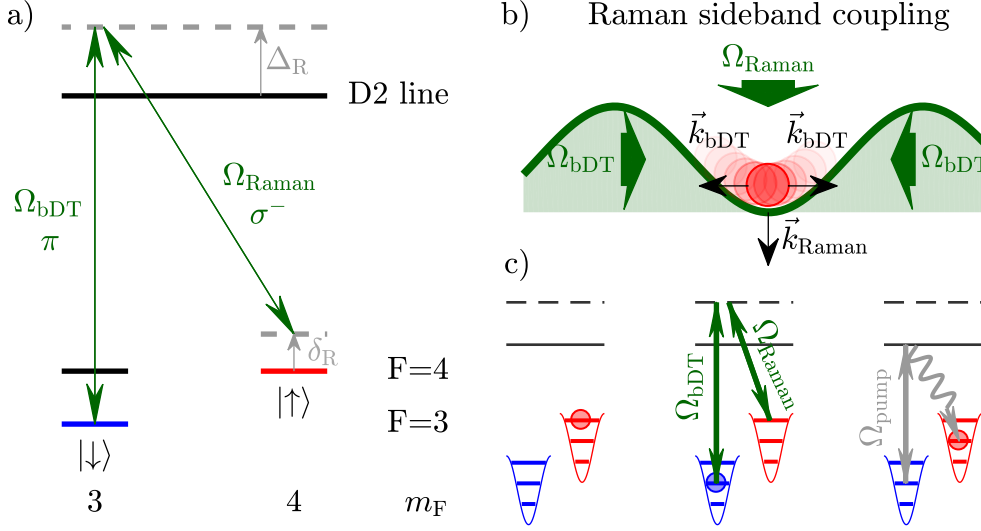


Figure 4.1: Raman sideband cooling: (a) The two qubit states, $|\uparrow\rangle$ and $|\downarrow\rangle$, are coherently coupled by two far-detuned Raman beams Ω_{bDT} and Ω_{Raman} with a two-photon detuning δ_R . (b) The principle of Raman sideband cooling is based on the removal of vibrational quanta by momentum transfer Δk in a two-photon recoil process during the qubit state transfer. The atom is located in the intensity minimum of the blue-detuned dipole trap, which leads to a suppression of the carrier transition. However, the atomic motion in the potential gives rise for a sideband coupling. (c) A Raman cooling cycle consists of a cooling sideband transition from the $|\uparrow\rangle$ to the $|\downarrow\rangle$. A strong optical pumping beam transfers the atom back without changing the vibrational state.

In Fig. 4.2 the result of a numerical simulation for our system is shown. A comparison of the eigenenergies and eigenstates between a sinusoidal and harmonic trapping potential shows a good agreement for the first excited state. A detailed description of the derivation of the so-called Wannier states in a periodic sinusoidal lattice is given in appendix A.2.

The Franck-Condon principle allows the separation of the wavefunction into the product state of a spin state $|\uparrow\rangle$ and a vibrational state $|n\rangle$ [65]. Our qubit states are described by $|\uparrow, n\rangle = |\uparrow\rangle \otimes |n\rangle$ and $|\downarrow, n'\rangle = |\downarrow\rangle \otimes |n'\rangle$. The principle describes that the electronic transition occurs in a negligible short time compared to the period of the atomic vibration. The strength of the coupling $\Omega_{n,n'}$ between the states $|\uparrow, n\rangle$ and $|\downarrow, n'\rangle$ is described in two terms:

$$\hbar\Omega_{n,n'} = \underbrace{\langle\downarrow|\hat{H}_{F,m_F}|\uparrow\rangle}_{\hbar\Omega_0} \langle n'|\hat{H}_{\text{FC}}|n\rangle \neq 0. \quad (4.3)$$

The first term describes the bare two-photon Rabi frequency Ω_0 and the second term gives the contribution of the coupling of the vibrational states $|n\rangle$ and $|n'\rangle$ by the Franck-Condon Hamiltonian \hat{H}_{FC} .

The simplest case is the carrier transition, which couples the same vibrational states. However, the desired sideband cooling occurs on the transitions described by the two orthogonal states $|n\rangle$ and $|n-1\rangle$. Two conditions must be fulfilled in the system: First, we need the ability to address vibrational states individually. This means that the sidebands are resolved. This is given in the so-called Lamb-Dicke regime. The second requirement is the appropriate design of a coupling of two orthogonal states. This is done in form of the Franck-Condon Hamiltonian such that the second term in eq. (4.3) is not zero.

Lamb-Dicke regime

The Lamb-Dicke regime is reached, if the extension of the atomic wave packet x_0 due to the strong confinement is significantly smaller than the laser wavelength λ_{DT} of the lattice. The recoil energy E_{rec} due to scattering of a lattice photon must be smaller than energy spacing E_{vib} between the vibrational levels:

$$\eta = \frac{2\pi}{\lambda_{\text{DT}}} x_0 = \sqrt{\frac{E_{\text{rec}}}{E_{\text{vib}}}} \ll 1 \quad (4.4)$$

is called the Lamb-Dicke parameter [66]. However, since the sideband coupling strength scales with $\sqrt{n}\eta$ the parameter should not be too small for efficient cooling.

Sideband coupling with Raman beams

In the case of Raman sideband coupling, the atom receives a momentum kick during the net momentum transfer $\Delta\mathbf{k} = \mathbf{k}_{\text{bDT}} - \mathbf{k}_{\text{Raman}}$ with the wave vectors of the respective Raman beams. The momentum transfer effectively breaks the orthogonality of the vibrational states. This allows the coupling of sidebands due to a residual overlap of the wave functions. The Franck-Condon Hamiltonian is described by the shape of the electric field operator, which depends on the net momentum transfer $\Delta\mathbf{k}$ and the position operator of the atomic center-of-mass motion $\hat{\mathbf{r}}$. The coupling is maximal for counter-propagating running wave Raman beams due to the net momentum of two photon recoil energies. Since we want to cool all directions with minimal technical effort, we choose orthogonal Raman beams along the dipole traps to simultaneously cool different directions with a net momentum of one photon recoil in each direction.

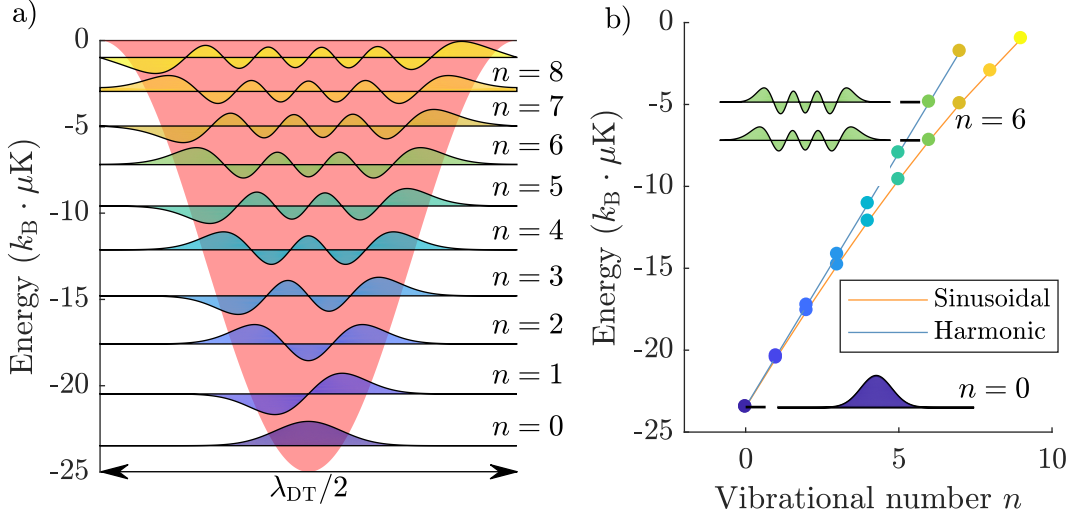


Figure 4.2: Vibrational states in a sinusoidal potential: (a) shows a numeric simulation of the probability densities of the vibrational eigenstates $|n\rangle$ with eigenenergies E_n in a red-detuned sinusoidal dipole trap with a potential depth of $k_B \cdot 25 \mu\text{K}$. (b) shows a comparison of the eigenenergies and eigenstates in an harmonic and sinusoidal potential. They agree well close to the ground state, but for high excitations the approximation is not valid anymore.

Boozer proposed a Raman coupling generated by a blue-detuned standing wave and a running-wave Raman beam [67]. We use the existing intra-cavity standing wave as one Raman beam to circumvent optical access limitations. The scheme is shown in Fig. 4.3. Even though the atoms are confined in the intensity minimum of the trap, the residual motion of the atoms gives rise to a coupling to the light field that is used for sideband cooling. The electric field of the Raman standing wave inside the cavity resonator along the z -direction is well described by a sine due to the high reflectivity of $\mathcal{R} \approx 1$. The field of the running wave Raman beam along the y -direction is represented in the conventional complex exponential form. The Franck-Condon factor $\hat{H}_{\text{FC}}^{\Delta \mathbf{k}}$ is then defined by the Raman photon momentum transfer $\Delta \mathbf{k}_z$ and $\Delta \mathbf{k}_y$ along the cooling axes x and y :

$$\begin{aligned} \hat{H}_{\text{FC}}^{\Delta \mathbf{k}} &= \sin(\Delta \mathbf{k}_x \hat{\mathbf{x}}) e^{i \Delta \mathbf{k}_y \hat{\mathbf{y}}} \\ &\approx (\Delta \mathbf{k}_x \hat{\mathbf{x}}) (\hat{\mathbf{1}}_y + i \Delta \mathbf{k}_y \hat{\mathbf{y}}) \\ \text{with } \hat{\mathbf{x}}/\hat{\mathbf{y}} &= \sqrt{\frac{\hbar}{2m_{\text{Cs}}\Omega_{\text{trap},x/y}}} (\hat{b}_{x/y}^\dagger + \hat{b}_{x/y}) \boldsymbol{\epsilon}_{x/y} \quad . \end{aligned} \tag{4.5}$$

The expression is approximated by the Taylor expansion and the position operators are rewritten in harmonic approximation by the raising and lowering operators

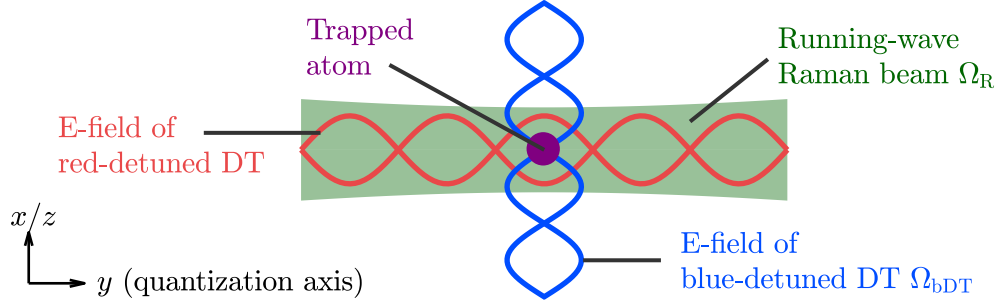


Figure 4.3: Setup for carrier-free Raman sideband cooling: A single cesium atom is trapped in a three-dimensional lattice potential. The behavior in x - and z -directions is qualitatively the same. Consequently, for the sake of this scheme, they are shown together in the same image plane. The red-detuned conveyor belt overlaps with two running-wave Raman beams along the quantization axis. The two static blue-detuned dipole traps along the x - and z -direction have a slight frequency difference of $2\pi \cdot 160$ MHz to prevent interference. A blue-detuned trap and a running-wave Raman beam form a set of Raman beams to couple the $|\uparrow\rangle$ - and $|\downarrow\rangle$ -state transition. The carrier transition is suppressed, since the atom is trapped in the zero-crossing of the blue-detuned dipole trap.

along the unit vector $\epsilon_{x/y}$, which fulfill $\sqrt{n} |n+1\rangle = \hat{b}^\dagger |n\rangle$ and $\sqrt{n-1} |n-1\rangle = \hat{b} |n\rangle$:

$$\hat{H}_{\text{FC}}^{\Delta \mathbf{k}} \approx \eta_x (\hat{b}_x^\dagger + \hat{b}_x) + \eta_x \eta_y i (\hat{b}_x^\dagger \hat{b}_y^\dagger + \hat{b}_x^\dagger \hat{b}_y + \hat{b}_x \hat{b}_y^\dagger + \hat{b}_x \hat{b}_y) \quad . \quad (4.6)$$

The carrier transition is suppressed, since all terms include a raising or lowering of the vibrational state. The first two terms $\hat{b}_x^\dagger, \hat{b}_y$ describe heating and cooling along the blue-detuned dipole trap axis only. The other four represent a coupled cooling and heating along both directions simultaneously. For a perfect sinusoidal standing wave without an imbalance of the intensity of the two counter-propagating beams we expect six first order sideband transitions. However, if such an imbalance occurs, we can account for this by the additional coupling of a weak running wave along the sinusoidal potential, which drives two photon-transitions with the running-wave Raman beam:

$$\begin{aligned} \hat{H}_{\text{FC}}^{\Delta \mathbf{k}} &= e^{i\Delta \mathbf{k}_x \hat{x}} e^{i\Delta \mathbf{k}_y \hat{y}} \\ &= \hat{\mathbf{1}}_x \hat{\mathbf{1}}_y + \eta_x (\hat{b}_x^\dagger + \hat{b}_x) + \eta_y (\hat{b}_y^\dagger + \hat{b}_y) + \eta_x \eta_y i (\hat{b}_x^\dagger \hat{b}_y^\dagger + \hat{b}_x^\dagger \hat{b}_y + \hat{b}_x \hat{b}_y^\dagger + \hat{b}_x \hat{b}_y) \end{aligned} \quad (4.7)$$

In a sideband spectrum, we expect the nine peaks which includes a carrier transition $\hat{\mathbf{1}}_x \hat{\mathbf{1}}_y$.

Raman sideband cooling cycle

The main concept of sideband cooling relies on removing a vibrational quanta in each successive cooling cycle until the ground state is populated and decoupled from the resonant laser excitation. A cooling cycle shown in Fig. 4.1 (c) consists of two processes: A coherent coupling at the cooling transition is accomplished between the two orthogonal states $|\uparrow, n\rangle$ and $|\downarrow, n-1\rangle$. The second process is an incoherent optical pumping on the $|F=3\rangle \rightarrow |F'=4\rangle$ transition, which irreversibly recycles the atoms from the $|\downarrow, n-1\rangle$ back to the $|\uparrow, n-1\rangle$. The $|\uparrow, 0\rangle$ ground state satisfies the definition of a dark state. The cooling cycle is most efficient when both coupling strengths are of the same order of magnitude. For simplicity, both transitions are driven continuously in parallel in our experiment. The efficiency can be increased by alternately applying a π -pulse on the cooling transition and a pumping pulse. In the following, I describe the Raman laser system, which allows cooling in three dimensions.

4.2 Raman laser system

Laser sources

High Raman coupling strength in the MHz regime can be achieved, since powerful laser diodes are available. In the cavity experiment, the Raman beams are supplied from two interference-filter stabilized external cavity diode lasers as shown in Fig. 4.4. They provide an optical output power of up to 150 mW. The wavelength of the lock laser is actively locked to the wavelength of the probe beam to allow simultaneously coupling of the beams into the cavity. The lock laser wavelength of 845.5 nm corresponds to a detuning of $\Delta_R = 2\pi \cdot 3$ THz from the cesium D2 line. The first laser is used for both π -polarized blue-detuned dipole traps along x - and z -direction. The second laser supplies two σ^- -polarized running-wave Raman beams along the quantization axis y .

The blue-detuned Raman dipole traps

The already existing intra-cavity standing wave along the z -direction has a trap depth of $k_B \cdot 180 \mu\text{K}$. In this work, we expand the setup by a new blue-detuned dipole trap along the third direction x with a trap depth of $k_B \cdot 70 \mu\text{K}$ respectively. The implementation is challenging due to limited optical access of the atom-cavity system. To avoid an additional Raman lock, we want to use the same laser frequency as the existing blue-detuned dipole trap. However, a slight constant shift in frequency with an AOM can circumvent interference between the different traps. In the case of the new blue-detuned dipole trap, it is not possible to split light from

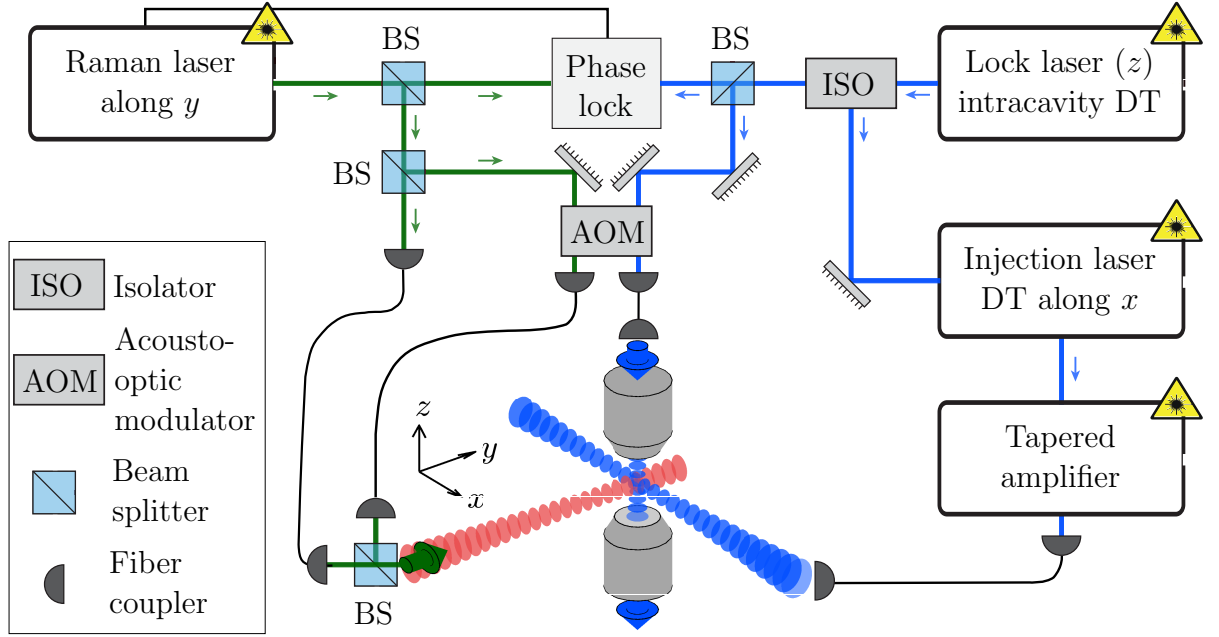


Figure 4.4: Raman locking system: The Raman laser is locked in phase to a lock laser. The lock laser supplies the intracavity dipole trap along z - and the blue-detuned dipole trap along x -direction. The lock laser power is enhanced by an injection locked laser, which is feeding a tapered amplifier. A relative frequency difference of $2\Delta = 2\pi \cdot 160$ MHz from an AOM double pass decouples the traps to avoid interference. The Raman laser is split into an undisturbed and a frequency shifted beam. They are recombined and send along the y -direction. The intracavity dipole trap and the frequency shifted running wave Raman beam cool the y - and z -direction simultaneously, while the other pair cool the x -direction.

the same laser source due to the three orders of magnitude higher required power. The power is amplified using the laser injection locking technique [68]. Injection locking is a phenomena of two oscillators with similar frequency. Within a certain frequency range, which is called the capture range the oscillators synchronize with each other. The chosen oscillator standard, on which the second oscillator is locked to, is called the master oscillator.

In this work, we extended the experiment by locking two lasers with this method. A fraction of the lock laser beam is injected into a free-running identical laser diode. An isolator prevents a back coupling of light from the injection laser diode into the lock laser. Within the capture range of the lock, the injection laser follows the frequency of the master laser and has the same narrow linewidth of a few kHz. An active lock is not required. It is sufficient to tune the free-running frequency of the injection laser by the temperature stabilization into the capture range of the lock.

This new blue-detuned dipole trap shows a slight imbalance between incoming and back-reflected beam due to lossy optical components, such as the vacuum glass cell, lenses and filtering optics. As a consequence, the atoms trapped in the intensity minima of the standing wave experience a small offset field of a running wave.

The running-wave Raman beams

In our experiment, a precise optical phase lock stabilizes the relative frequency difference of the two laser frequencies to the hyperfine splitting of the ground states plus a controllable two-photon detuning δ_R [69]. One blue-detuned dipole trap and one running-wave beam defines one set of Raman beams. The first set cools the yz -direction and the second set is used for cooling along the x -direction. In order to avoid interference between different Raman beams, they have different frequencies. To achieve that, one set of Raman beams is guided spatially separated through the same AOM double pass applying a frequency shift of $2\Delta = 2\pi \cdot 160$ MHz. The running-wave Raman beams are intensity stabilized to a power of $100 \mu\text{W}$ at the cavity position to reduce fluctuations of the Raman coupling strength.

4.3 Three-dimensional carrier-free Raman sideband cooling

Two-dimensional temperature model

The temperature of a trapped atomic ensemble can be measured by a variety of techniques, such as the time-of-flight method [70] or the Doppler broadening of Raman transitions between the ground states [71]. In this work, the temperature in two dimensions y and z is quantified by a resolved Raman sideband spectrum. Precise knowledge about the parameters of the trapping potential is essential for the positional and temperature control of the atoms in an optical lattice. In most previous works, a simple Gaussian curve fit of the resonance peaks of a sideband spectrum is chosen to determine the trapping frequency and the temperature. However, this is an approximation and only valid for harmonic potentials. Therefore, I derive a new model, which considers the anharmonicity of a sinusoidal potential. Furthermore, the model includes also the dynamics of Raman sideband transitions described by the Franck-Condon Hamiltonian. It leads to the expected suppression of the carrier transition for a Raman beam formed by a blue-detuned dipole trap.

We can attribute a temperature T_x^* , T_y^* and T_z^* in each respective dimension. The spectrum is an average over several hundreds of atoms and determines the mean

temperature T^* . If the atoms are in thermal equilibrium, the occupation of the vibrational states $p_B(n, T^*)$ is distributed according to a Boltzmann distribution.

$$p_B(n, T^*) = \frac{e^{-\frac{E_n}{k_B T^*}}}{\sum_{n=0}^{\infty} e^{-\frac{E_n}{k_B T^*}}} \approx \frac{\bar{n}^n}{(\bar{n} + 1)^{n+1}} \quad . \quad (4.8)$$

The Boltzmann distribution is valid for both directions and thus is shown without directional indices. By approximating the trap potential by an harmonic potential, the distribution depends only on the mean vibrational occupation number \bar{n} [66]. This approximation is suitable for atoms close to the ground state.

In order to determine the temperature, we need to know the distribution $p_B(n, T^*)$. This is achieved with a two-dimensional Raman sideband spectroscopy in x , y - and y , z -direction. The state under study is described by the eigenstates $|n_x\rangle$ and $|n_y\rangle$ in the ground state $|\uparrow\rangle$ and the probabilities $p_B(n_x, T_x^*) = |c_{n_x}|^2$ and $p_B(n_y, T_y^*) = |c_{n_y}|^2$:

$$\begin{aligned} |\psi(0)\rangle &= \sum_{n_x=0}^{\infty} \sum_{n_y=0}^{\infty} c_{n_x} |n_x\rangle \otimes c_{n_y} |n_y\rangle \otimes |\uparrow\rangle \\ &= \sum_{n_x, n_y} c_{n_x} c_{n_y} |n_x, n_y, \uparrow\rangle \quad . \end{aligned} \quad (4.9)$$

The sideband spectroscopy technique is based on the fact, that the coupling strength of a Raman transition between ground states depends on the vibrational state number n . By driving this state with coherent radiation on a transition, the state under study is mapped onto the internal state $|n'_x\rangle \otimes |n'_y\rangle \otimes |\downarrow\rangle$. The operation with the Raman coupling strength $\Omega_{n_x, n'_x, n_y, n'_y}$ and a phase θ has the general form of a Rabi oscillation:

$$\begin{aligned} |\psi(t)\rangle &= \sum_{n_x, n'_x, n_y, n'_y} c_{n_x} c_{n_y} \cos\left(\frac{\Omega_{n_x, n'_x, n_y, n'_y}}{2} t\right) |n_x, n_y, \uparrow\rangle \\ &\quad + e^{i\theta} c_{n_x} c_{n_y} \sin\left(\frac{\Omega_{n_x, n'_x, n_y, n'_y}}{2} t\right) |n'_x, n'_y, \downarrow\rangle \quad . \end{aligned} \quad (4.10)$$

The dependency is used to map the vibrational state of the atoms onto the internal state in the resolved sideband regime. The internal state can be read out with standard techniques as a measure for the mapped state. The probability, that the

state under study ends up in the $|\downarrow\rangle$ -state is given by

$$\begin{aligned}
 P_{\downarrow}(t) &= |\langle \psi(t) | n'_x, n'_y, \downarrow \rangle|^2 \\
 &= \sum_{n_x, n'_x, n_y, n'_y} |c_{n_x}|^2 |c_{n_y}|^2 \sin^2 \left(\frac{\Omega_{n_x, n'_x, n_y, n'_y}}{2} t \right) \\
 &= \sum_{n_x, n'_x, n_y, n'_y} p_B(n_x, T_x^*) p_B(n_y, T_y^*) \sin^2 \left(\frac{\Omega_{n_x, n'_x, n_y, n'_y}}{2} t \right) .
 \end{aligned} \tag{4.11}$$

The coupling strength $\Omega_{n_x, n'_x, n_y, n'_y}$ follows from eq. (4.3) and eq. (4.5)

$$\begin{aligned}
 \hbar \Omega_{n_x, n'_x, n_y, n'_y} &= \langle \downarrow | \hat{H}_{F, m_F} | \uparrow \rangle \cdot \langle n'_x | \sin(\Delta \mathbf{k}_x \hat{\mathbf{x}}) | n_x \rangle \cdot \langle n'_y | e^{i \Delta \mathbf{k}_y \hat{\mathbf{y}}} | n_y \rangle \\
 &= \hbar \Omega_0 \cdot FC_{n_x, n'_x} \cdot FC_{n_y, n'_y} .
 \end{aligned} \tag{4.12}$$

The Franck-Condon factors FC_{n_x, n'_x} and FC_{n_y, n'_y} describe the overlap between the corresponding eigenstates. They are determined numerically for a certain trap depth U_x and U_y and the well-known frequency of the dipole trap beams, which determines the momentum transfer $\Delta \mathbf{k}_x$ and $\Delta \mathbf{k}_y$ of one photon recoil. The eigenstates as well as the atomic transition frequencies ν_{n_x, n'_x} and ν_{n_y, n'_y} are calculated by solving the stationary Schrödinger equation from eq. (4.2). In eq. (4.12), we assume a perfect sinusoidal standing wave without an imbalance of the intensity of two counter-propagating beams. However, if such an imbalance occurs, we can account for this by the additional coupling term:

$$\begin{aligned}
 \hbar \Omega_{n_x, n'_x, n_y, n'_y} &= \langle \downarrow | \hat{H}_{F, m_F} | \uparrow \rangle \cdot \langle n'_x | e^{i \Delta \mathbf{k}_x \hat{\mathbf{x}}} | n_x \rangle \cdot \langle n'_y | e^{i \Delta \mathbf{k}_y \hat{\mathbf{y}}} | n_y \rangle \\
 &= \hbar \Omega_0 \cdot FC'_{n_x, n'_x} \cdot FC'_{n_y, n'_y} .
 \end{aligned} \tag{4.13}$$

The probability $P_{\downarrow}(t)$ in eq. (4.11) describes the maximum transfer probability for a resonant driving. For simplicity, I assume Gaussian shaped resonance peaks. The measured spectrum is then determined by

$$\mathcal{S}(\nu) = A \cdot \sum_{n_x, n'_x, n_y, n'_y} P_{\downarrow}(t) \cdot \exp \left(- \frac{(\nu - \nu_{n_x, n'_x} - \nu_{n_y, n'_y} - \nu_0)^2}{2\sigma^2} \right) . \tag{4.14}$$

The Gaussian widths depend on the driven transition. The sum of the Gaussian curves result in an asymmetric profile of each sideband. In previous models only symmetric sidebands are described. In case, no carrier transition is driven in both directions, the Gaussian width results from a convolution of two Gaussian curves with the widths σ_x and σ_y :

$$\sigma = \begin{cases} \sigma_z & n'_x = n_x, \ n'_y \neq n_y, \\ \sigma_y & n'_x = n_x, \\ \sqrt{\sigma_y^2 + \sigma_x^2} & \text{otherwise} \end{cases} . \tag{4.15}$$

The free parameters of the spectrum fit are the bare Rabi frequency Ω_0 , two Gaussian widths σ_x and σ_y , the trap depths U_x and U_y and the temperatures in each direction x and y and a general frequency offset ν_0 of the carrier transition and the amplitude A .

The first blue and red sideband have proven to be very useful to determine the distribution of the vibrational state occupation. In the following, I describe how we measure the Raman sideband spectrum for the first order sidebands and determine the temperature with this derived model.

Measurement of two-dimensional carrier-free Raman ground state cooling

In order to determine the temperature distribution, we conduct a Raman sideband spectrum in the atom-cavity system. First, a single atom inside the cavity is prepared in the $|\uparrow\rangle$ -state. We are interested in the temperature distribution $p(n, T)$ of this state under study. After a Raman transfer pulse, we map the vibrational state onto the $|\downarrow\rangle$ -state as described before. The population is detected with the non-destructive state detection technique. For a sideband spectrum, the two-photon detuning δ_R from the carrier transition is varied for the transfer pulse. As mentioned before, the pulse is optimized for a maximum transfer probability on the first sideband. The resulting spectrum with just cavity cooling is shown in Fig. 4.5(a) for a detuning range of 1 MHz. The first observation is, that the spectrum shows six resonance peaks with positions symmetric around the carrier frequency. A fit of the two-dimensional temperature model to the experimental data is shown as a red line. The constituting sidebands are shown in yellow. As expected, the carrier transition is strongly suppressed. The six peaks correspond to the six terms in eq. (4.6):

$$\hat{H}_{\text{FC}}^{\Delta k} = \eta_z(\hat{b}_z^\dagger + \hat{b}_z) + \eta_y\eta_z i(\hat{b}_z^\dagger\hat{b}_y^\dagger + \hat{b}_z^\dagger\hat{b}_y + \hat{b}_z\hat{b}_y^\dagger + \hat{b}_z\hat{b}_y) \quad , \quad (4.16)$$

with the Lamb-Dicke parameters being $\eta_z = 0.1$ and $\eta_y = 0.06$. In order to identify the correspondence between the terms and the peaks, we can vary the intensity of one dipole trap. This leads to a change of the trap frequencies, which results in a shift of the position of the corresponding peak.

In order to cool the atoms simultaneously in y - and z -direction, we need to overlap two sidebands. We adjust the trap frequencies such, that they fulfill the condition $\nu_y = 2 \cdot \nu_z$. Figure 4.5(b) shows the spectrum, where this condition is fulfilled. Here, the cooling transition \hat{b}_z overlaps with the transition $\hat{b}_z^\dagger\hat{b}_y$. The ladder heats along the z -direction and cools along the y -direction. The coupling strength in z -direction $\Omega_0\eta_z$ is stronger than the coupled transition strength $\Omega_0\eta_z\eta_y$ and atoms are effectively cooled along the blue-detuned trap axis z . If the atoms are

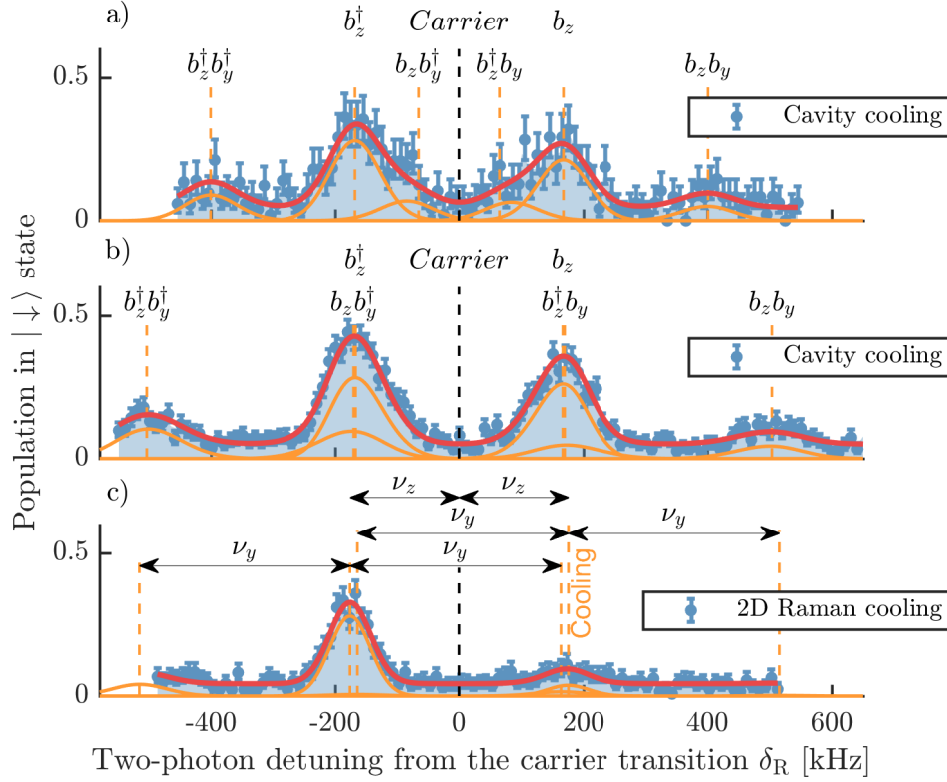


Figure 4.5: Measurement of two-dimensional carrier-free Raman sideband cooling: (a) and (b) shows a spectrum with cavity cooling. The carrier transition is strongly suppressed due to the nature of the cavity standing-wave Raman beam along the z -direction and a running-wave Raman beam along the y -direction. Six Raman couplings are observed and adjusted such that the cooling sideband peaks $b_z^\dagger b_y$ and b_z are overlapped by choosing $\nu_y = 2 \cdot \nu_z$. The constituting sidebands are shown in yellow. (c) shows the spectrum with additional two-dimensional Raman sideband cooling in y - and z -direction. Efficient ground state cooling is indicated by the vanishing cooling sideband peaks.

in the two-dimensional ground state, they are decoupled from all Raman couplings and form a dark state of this system.

The sideband heights are proportional to the corresponding coupling strengths. For a negligible ground state population, we expect a similar height of the heating and the corresponding cooling sideband. If more atoms populate the ground state, the cooling sideband height decreases. This is already observed in both discussed spectra without Raman sideband cooling.

A fit of the two-dimensional temperature model in eq. (4.14) determines the ground state population $p(0)$ and the mean vibrational state number \bar{n} . These

parameters are the commonly used quantities to describe the atomic temperature, since they are comparable between different experiments. In the presence of just cavity cooling (spectrum in Fig. 4.5(b)), we determine a ground state population of $p_y(0) = (54.6 \pm 8.7) \%$ in y -direction and $p_z(0) = (10.0 \pm 4.4) \%$ in the z -direction, which corresponds to a mean vibrational occupation number of $\bar{n}_y = 0.14 \pm 0.11$ and $\bar{n}_z = 0.83 \pm 0.30$ (see eq. (4.8)).

In the next experiment, we apply two-dimensional Raman sideband cooling as previously discussed. The atom is prepared in the $|\uparrow\rangle$ -state and cooled with a single Raman sideband cooling pulse with a two-photon detuning $\delta_R = 180 \text{ kHz}$ of and a duration of 1 ms, which is long enough to reach a thermal equilibrium. Figure 4.5(c) shows the resulting sideband spectrum. In comparison to the spectra without Raman sideband cooling, we immediately observe a reduction of the sideband peak heights of \hat{b}_z and $\hat{b}_z^\dagger \hat{b}_y$. The ground state population in z -direction increases drastically to $(89.8 \pm 9.7) \%$ and reduces the mean vibrational occupation number to $\bar{n}_z = 0.14 \pm 0.11$. Thus, the additional Raman sideband cooling lowers the temperature significantly.

An additional observation is that the sidebands in the spectrum just with cavity cooling show a stronger asymmetric shape, a broader linewidth and a position closer to the carrier transition. This can be attributed to the fact, that the trapping potential close to the ground state can be approximated by a harmonic potential. However, for higher temperatures the anharmonicity can not be neglected. This shows, that the developed two-dimensional temperature model is able to determine the properties of trapped atoms with higher accuracy, since it takes the anharmonicity into account.

Cooling efficiency with carrier suppression

Raman sideband cooling with a suppressed carrier leads to a higher cooling efficiency compared to conventional Raman sideband cooling. The cooling efficiency is described by the rate equation in harmonic approximation [66]. For the final stage of the cooling, the rate equation is restricted to the vibrational ground and the first excited state with the probabilities of the respective states $p_0 + p_1 = 1$:

$$\dot{p}_0 = p_1 \underbrace{\frac{(\eta\Omega)^2}{\Gamma_{\text{rep}}}}_{\text{cooling rate}} + p_0 \underbrace{\left(\left(\frac{\Omega}{2\Omega_z} \right)^2 \cancel{(\eta^2 \Gamma_{\text{rep}})} + \left(\frac{\eta\Omega}{4\Omega_z} \right)^2 \Gamma_{\text{rep}} \right)}_{\text{heating rate}} . \quad (4.17)$$

The first term describes the cooling rate with the Rabi frequency $\Omega = \Omega_{0,0} \approx \Omega_{1,1}$. It is defined by the probability of the atom being pumped into the first excited state $(\eta\Omega)^2/\Gamma_{\text{rep}}^2$ times the spontaneous decay rate on the carrier transition Γ_{rep} . The second term involves the off-resonant driving on the Raman carrier transition

$(\Omega/2\Omega_z)^2$ with a detuning Ω_z and the spontaneous decay on the heating transition with the rate $\eta^2\Gamma_{\text{rep}}$. The last term describes the off-resonant excitation of the Raman heating sideband $(\eta\Omega/4\Omega_z)^2$ with a detuning of $2\Omega_z$ and the spontaneous decay on the carrier transition. If the Raman carrier transition is suppressed, the second term vanishes. In steady state, which is defined by $\dot{p}_0 = 0$, the mean vibrational occupation yields

$$\bar{n} \approx p_1 = \left(\frac{\Gamma_{\text{rep}}}{2\Omega_z} \right)^2 (\chi + 1/4) \quad . \quad (4.18)$$

The mean vibrational occupation in steady state defines the cooling limit. With carrier suppression it is five times lower. In the following, the carrier-suppressed Raman sideband cooling is extended to the third direction x to cool all dimensions simultaneously.

Three-dimensional Raman ground state cooling

So far, the carrier-free Raman sideband cooling was applied to two spatial directions. In this work, the setup is extended by the second standing-wave blue-detuned dipole trap along the x -direction for strong confinement in all directions. An additional running-wave Raman beam along the y -direction allows for simultaneous three-dimensional Raman sideband cooling. The details of this injection locked trap and the new running-wave Raman beam are described in chapter 4.1.

The slight imbalance of the incoming and back-reflected beam of the new blue-detuned dipole trap leads additionally to the sinusoidal trapping potential to a small offset field of a running wave. As a consequence, the carrier suppression is not as strong as for the intra-cavity standing-wave Raman beam. Due to this, we expect in the Raman sideband spectrum three additional transition peaks. The nine transition peaks are described in eq. (4.7) by the terms:

$$\begin{aligned} H_{\text{FC}}^{\Delta k'} = & \hat{\mathbb{1}}_x \hat{\mathbb{1}}_y + \eta_x (\hat{b}_x^\dagger + \hat{b}_x) + \eta_y (\hat{b}_y^\dagger + \hat{b}_y) \\ & + \eta_x \eta_y i (\hat{b}_x^\dagger \hat{b}_y^\dagger + \hat{b}_x^\dagger \hat{b}_y + \hat{b}_x \hat{b}_y^\dagger + \hat{b}_x \hat{b}_y) \end{aligned} \quad (4.19)$$

The Lamb-Dicke parameters are $\eta_x = 0.14$ and $\eta_y = 0.06$. The measurement of the Raman sideband spectrum in x, y -direction is performed as in the previous experiment with two-dimensional ground state cooling. The atoms are prepared in the $|\uparrow\rangle$ -state. The state under study is cooled by two-dimensional Raman cooling in y - and z -direction. To determine the spectrum along the x, y -direction, the new Raman beams are used to map the vibrational state onto the internal ground state $|\downarrow\rangle$. Figure 4.6(a) shows the resulting spectrum with two-dimensional Raman sideband cooling. The x -direction is not cooled, which leads to two strong

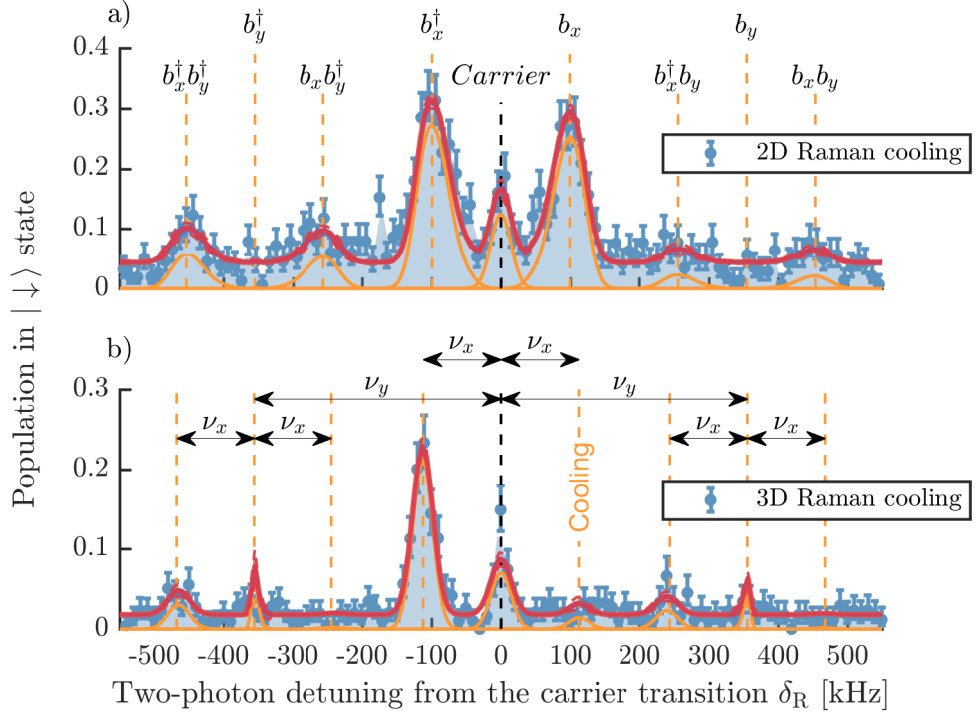


Figure 4.6: Measurement of three-dimensional Raman sideband cooling: The spectra determine the cooling dynamics along the x - and y -direction with a second set of Raman beams. In the top figure, the atoms are cooled in y, z -direction by two-dimensional carrier-free Raman sideband cooling. In the lower figure, the x -direction is simultaneously cooled, which is indicated by the vanishing cooling sideband b_x and brings the atoms into the three-dimensional ground state.

sidebands b_x and \hat{b}_x . As expected, we observe a small carrier transition in the center. A fit of the two-dimensional temperature model is shown as a red line with the constituting peaks (yellow). From the fit parameters we can extract the ground state population of $p_x(0) = (10.1 \pm 6.9)\%$ in x -direction and a mean occupation number of $\bar{n}_x = 8.3 \pm 8.1$. The ground state population in y -direction is $p_y(0) = (60.5 \pm 17.9)\%$ with a mean occupation number of $\bar{n}_y = 0.66 \pm 0.53$.

In the next step, we apply additional cooling along the x -direction at a two-photon detuning $\delta_R = 114$ kHz. Figure 4.6(b) shows the resulting Raman sideband spectrum. The sideband b_x significantly reduces. From the fit parameters we extract a ground state population of $p_x(0) = (94.8 \pm 3.4)\%$ in x -direction and a mean occupation number of $\bar{n}_x = 0.06 \pm 0.04$. For three-dimensional ground state cooling we observe a significant reduction of the background noise. As for the cooling spectra in y, z -direction, the sideband peaks become narrower, more symmetric and shifted towards higher detunings from the carrier transition with

| Direction | Mean vibrational occupation \bar{n} | Ground state population |
|-----------|---------------------------------------|-------------------------|
| x | 0.06 ± 0.04 | $(94.8 \pm 3.4)\%$ |
| y | 0.66 ± 0.53 | $(60.5 \pm 17.8)\%$ |
| z | 0.14 ± 0.11 | $(89.8 \pm 9.7)\%$ |

Table 4.1: Summary of three-dimensional ground state cooling.

applied cooling. A summary of the achieved results of three-dimensional cooling is shown in Tab. 4.1.

4.4 Conclusion

In this chapter, I described the experimental apparatus for two-dimensional carrier-free Raman sideband cooling and showed measurements with this existing setup. The measurement were interpreted with a newly developed model. The model considers the anharmonic shape of the lattice and is based on the full Hamiltonian of the system leading to a better fit of the model to the measured Raman sideband spectrum.

The two-dimensional trap was extended by a new blue-detuned dipole trap to strongly confine the atoms also in the third dimension. Challenged by the limited optical access of the cavity experiment, this carrier-free Raman sideband cooling scheme is extended along the new dipole trap axis without the need of additional lasers and allows efficient ground state cooling in all three dimensions. The ground state occupation of $(94.5, 60.5, 89.8)\%$ in x, y, z -direction respectively is achieved within a few milliseconds and an atom can be repeatedly recooled. Recently, the scheme developed for this system has been adapted by the new fiber cavity experiment in our group.

CHAPTER 5

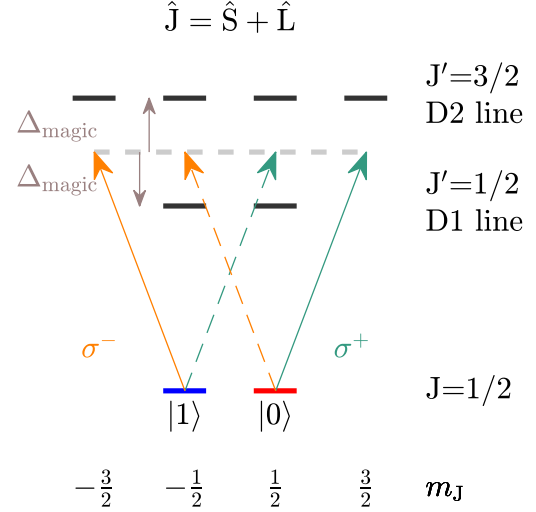
STATE-DEPENDENT LATTICE TRANSPORT WITH NEUTRAL ATOMS

In this chapter, I introduce the experimental apparatus for state-dependent lattice transport, which allows to apply microwave sideband cooling in one dimension. This is a prerequisite for an optimal control transport of atoms while maintaining their vibrational ground state occupation. Further details on this experimental setup can also be found in earlier dissertations [23, 30, 72, 73]. To accomplish the main goal of this work – optimal control transport – it is crucial to characterize the system response of the lock system in detail. I gain a deep understanding of the system by means of signal processing theory, in order to experimentally reproduce arbitrary transport ramps.

5.1 Atom transport

Position controlling and transport of neutral atoms in optical traps are crucial for a number of seminal experiments in quantum optics. Atom transport has been demonstrated by a variety of techniques. A very successful one is the use of optical tweezers. As an example they have been used to move Bose-Einstein condensates by means of translating a focusing lens [74]. Even a shift register architecture is realized with microtraps by shifting the angle of the incident beam through a microlens array [75]. Optical tweezers are also combined with a spatial light modulator [76, 77] or an acousto-optic deflector [78] to generate low entropy states. Another approach of atomic position control is based on moving optical lattices. This technique shows high precision of the relative position between the lattices of 1.2 \AA [24]. The movement of the lattices can be achieved by frequency [79] and phase modulation of the lattice beams. With phase modulation to move an optical lattice, we realize quantum walk experiments [57], a digital atom interferometer [80] as well as controlled collisions for multi-particle entanglement [81].

Figure 5.1: Principle of the state-dependent lattice: Two overlapped lattices are blue-detuned with respect to the D1 line and red-detuned with respect to the D2 line. The resulting potentials cancel out for one polarization component such that the $|0\rangle$ ($|1\rangle$) state is effectively trapped by σ^+ (σ^-)-polarized lattice.



5.2 State-dependent lattice

The multilevel structure of cesium allows the design of a state-dependent lattice [82]. To gain an intuitive understanding of the principle of a state-dependent lattice, we use the two degenerate ground states $|0\rangle$ and $|1\rangle$ in the fine structure representation

$$\begin{aligned} |0\rangle &= |J = 1/2, m_J = 1/2\rangle \quad , \\ |1\rangle &= |J = 1/2, m_J = -1/2\rangle \quad . \end{aligned} \quad (5.1)$$

The total angular momentum J represents the interaction of the orbital momentum of the electrons with their total electronic spin. It leads to the fine structure splitting described with the quantum number m_J . As depicted in Fig. (5.1), the frequency of the lattice beams is chosen to lay in between the D1- and D2-line of cesium. The interaction of the beam with the D1-line is repulsive, since the beam is blue-detuned for this atomic transition. Correspondingly, the same beam is red detuned for the D2-line, which results in an attractive potential. Consequently, the atoms experience the sum of an attractive and a repulsive trapping potential as described in eq. (2.3). The frequency is chosen such that the sum exactly cancels, which we call the magic wavelength. However, as seen in the sketch, there are transitions, where the atoms only experience the attractive potential. For example, the state $|0\rangle$ experiences an attractive potential of a σ^+ -polarized trap, while the forces of the σ^- -polarized trap vanish. This is indicated by a dashed arrow. This means, by choosing the right polarized light, we can apply a force depending on the state.

Since the D1- and D2-line consist of many atomic hyperfine states, we have to adapt the principle to the hyperfine representation. The nuclear spin $I = 7/2$ lifts this degeneracy and leads to the well known hyperfine ground states used for the

cesium standard of time. The outermost Zeeman states can be expressed in the basis of the fine structure representation yielding [57]

$$\begin{aligned} |\uparrow\rangle &= |I = 7/2, m_I = 7/2\rangle \otimes |0\rangle \quad , \\ |\downarrow\rangle &= \sqrt{\frac{7}{8}} |I = 7/2, m_I = 7/2\rangle \otimes |1\rangle - \sqrt{\frac{1}{8}} |I = 7/2, m_I = 5/2\rangle \otimes |0\rangle \quad . \end{aligned} \quad (5.2)$$

This indicates that the chosen spin states have two slightly different magic wavelengths at 865.9 nm and 869.3 nm. In the experiment, we choose the same wavelength for both traps, which results in equal distances between the potential wells of both lattices. In this work, we choose a magic wavelength of 865.9 nm for all measurements. Then, the σ^+ -polarized dipole trap confines only atoms in the $|\uparrow\rangle$ -state and atoms in the $|\downarrow\rangle$ -state are attracted by both traps, but dominated by the σ^- -polarized dipole trap:

$$\begin{aligned} U_{\text{DT}}^\uparrow &= U_{\text{DT}}^{\sigma^+} \quad , \\ U_{\text{DT}}^\downarrow &= \frac{7}{8} U_{\text{DT}}^{\sigma^-} + \frac{1}{8} U_{\text{DT}}^{\sigma^+} \\ &\text{with} \\ U_{\text{DT}}^{\sigma^+/\sigma^-}(\rho, z) &= U^{\sigma^+/\sigma^-} \cos^2((kz - \varphi^{\sigma^+/\sigma^-}(t))/2) e^{-2\rho^2/w_{\text{DT}}^2} \quad . \end{aligned} \quad (5.3)$$

U_{DT} describes the full potential with the effective trap depth U . The index σ^+ and σ^- refers to the lattice with the corresponding polarization. The trapping frequencies of the lattices are both $\Omega_{\text{trap}} = 2\pi \cdot 115$ kHz along the one-dimensional trap axis. The weak confinement along the radial direction leads to a trapping frequency of $\Omega_{\text{rad}} = 2\pi \cdot 1$ kHz. The maximum trap depth U^\uparrow and phase φ^\uparrow experienced by the $|\uparrow\rangle$ -state is by design identical to the σ^+ -polarized potential. The trap depth of the $|\downarrow\rangle$ -state however is a mixture of both circularly polarized trapping potentials and can be expressed by an effective trap depth U^\downarrow and phase φ^\downarrow [83]:

$$\begin{aligned} U^\uparrow &= U^{\sigma^+}, & U^\downarrow &= \sqrt{s_\sigma^2 + c_\sigma^2} \\ \varphi^\uparrow &= \varphi^{\sigma^+}, & \varphi^\downarrow &= \arctan \left\{ \frac{s_\sigma}{c_\sigma} \right\} \quad , \end{aligned} \quad (5.4)$$

with

$$\begin{aligned} s_\sigma &= \frac{7}{8} U^{\sigma^-} \sin \left\{ \varphi^{\sigma^-} \right\} + \frac{1}{8} U^{\sigma^+} \sin \left\{ \varphi^{\sigma^+} \right\} \quad , \\ c_\sigma &= \frac{7}{8} U^{\sigma^-} \cos \left\{ \varphi^{\sigma^-} \right\} + \frac{1}{8} U^{\sigma^+} \cos \left\{ \varphi^{\sigma^+} \right\} \quad . \end{aligned} \quad (5.5)$$

A detailed derivation is found in the appendix A.1. The effective potential U^\downarrow changes due to a dipole trap crosstalk for different relative positions between the

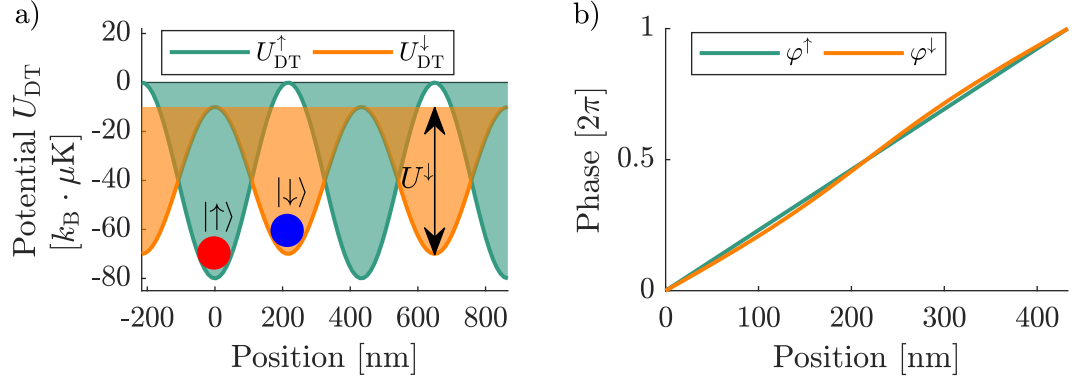


Figure 5.2: Effective trapping potential and phase of the $|\uparrow\rangle$ - and $|\downarrow\rangle$ -state for the state-dependent lattices: (a) The wavelength of the state-dependent lattices is chosen such that the U^\uparrow remains unchanged independent from the relative position of both traps. However, the effective potential U^\downarrow changes due to a dipole trap crosstalk. For a relative lattice separation of $\lambda/4$, it reaches a minimum trap depth. The trapping potential are identical if both lattices overlap. (b) A linear phase driving ramp $\varphi^{\sigma^+/\sigma^-}$ results is reproduced by the $|\uparrow\rangle$ -state, while the $|\downarrow\rangle$ -state performs an effective s-shaped driving ramp.

lattices. For a relative lattice separation of $\lambda/4$ as shown in Fig. 5.2, the potential reaches a minimum trap depth. The trapping potentials are identical, if both lattices overlap. Figure 5.2 (b) shows a linear phase driving ramp of the σ^- - and σ^+ -lattice. While the atoms in the $|\uparrow\rangle$ -state experience this linear transport, the atoms in the $|\downarrow\rangle$ -state perform an effective s-shaped driving ramp.

5.3 Atom loading and state manipulation

The realization of the state-dependent lattice experiment is shown in Fig. 5.3. Here, a MOT is overlapped with two state-dependent lattices. During a loading process, up to 50 atoms are released from the MOT into the standing wave potential. The $|\uparrow\rangle$ -state is prepared with two σ^+ -polarized pumping beams (gray) on the $|F=3\rangle \rightarrow |F'=4\rangle$ and $|F=4\rangle \rightarrow |F'=4\rangle$ transition, which are overlapped with the state-dependent lattice. Using microwave radiation, the $|\downarrow\rangle$ -state is coupled to the $|\uparrow\rangle$ -state allowing us to generate an arbitrary superposition state.

Push-out state detection in the state dependent lattice

After performing an experiment, the state of the atoms is determined by a technique called push-out state detection. The main concept relies on removing atoms

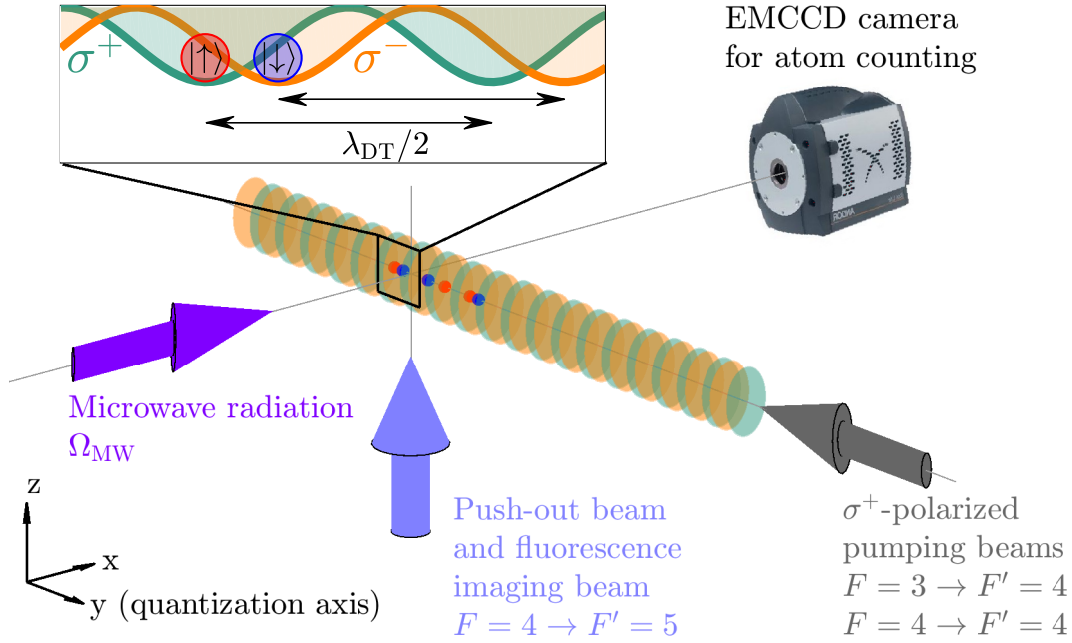


Figure 5.3: Illustration of the state-dependent lattice experimental setup: Two state-dependent lattices for each spin state are overlapped with a MOT (not shown). Two optical pumping beams are used for state preparation and microwave radiation for state manipulation. The number of atoms in the lattice is counted with an EMCCD camera by collecting the scattered fluorescence imaging light. For state detection, atoms in the $|\uparrow\rangle$ -state are removed with a resonant push-out beam.

in a certain hyperfine state and detecting the atom survival of the other hyperfine state. The technique uses the radiation pressure by photon scattering of a near-resonant laser beam. A strong σ^+ -polarized laser beam is tuned to the $|F = 4\rangle \rightarrow |F' = 5\rangle$ transition and heats the atoms in the $|\uparrow\rangle$ -state out of the lattice. Due to selection rules, the $|\downarrow\rangle$ -state is a dark state and only off-resonant scattering on the $|F = 3\rangle \rightarrow |F' = 4\rangle$ limits the overall detection efficiency to 99%. The number of initialized atoms and remaining atoms after the push-out pulse is counted by fluorescence imaging with an electron multiplying CCD camera (EMCCD, Andor: iXon DV897DCS-FI). This detection technique suffers from atom loss and a single state measurement takes much longer in comparison to the non-destructive state detection in the cavity experiment. Nevertheless, the experiment offers a similarly fast detection over the total measurement time due to the significant higher atom loading rate per repetition. This justifies the choice of this comparatively simple detection technique.

5.4 Experimental setup of the state-dependent lattices

The experimental apparatus allows for remarkable degree of position control. Details can be found in the thesis of Robens [30]. The properties of the apparatus are fundamental to perform optimal control transport in this work. The setup allows the full control over the trap depths and the relative positions of the state-dependent lattices. It is sketched in Fig. 5.4 and summarized in this paragraph.

The laser beam generated by a titanium-sapphire laser system (Coherent MBR 110 pumped by Coherent Verdi V18) delivers an output power up to 2.5 W at a wavelength of 866 nm and is split into two arms with a beam splitter (BS). The first arm is the intensity-stabilized ($\sigma^+ + \sigma^-$)-polarized running wave, which enters the vacuum cell from the left side. This beam is first sent through an acousto-optic modulator (Gooch & Housego: AOM 3080-122) with a constant frequency of 80 MHz. In order to clean up the spatial mode, the beam is guided through a fiber. After the fiber, a fraction is extracted to stabilize the intensity with the AOM. The second arm generates two beams with a σ^+ or σ^- polarization, which is guided through the vacuum cell from the right side. First this second arm is split with a polarizing beam splitter into two beams. Each beam is being individually controlled by an AOM with a relative phase and intensity. A Wollaston prism (WP) with a high extinction ratio ($> 10^{-7}$) is used to recombine the beams. The spatial mode is again cleaned up with the help of a fiber. After the fiber a fraction of the light is extracted in order to control the intensity of each beam. A second fraction of the light is split up and overlapped with laser light from the undisturbed output of the laser. This beat signal is used to control the phase of the two synthesized arms. For the phase and intensity locks of the second arm, Wollaston prisms are used to separate the beam according to their polarization. It allows to separately measure the beam intensity and relative phase to the counter-propagating laser beam of both lattices. A detailed view of the lock systems is shown in Fig. 5.5. The intensity and phase responses are converted in a servo loop into an amplitude and frequency signal, which drive the acousto-optic modulator of the different polarization arms.

The beams are focused down to the experimental region with a waist of 17 μm . The dominating noise source of this synthesized lattices are spatial polarization inhomogeneities of the laser beams determined by the linear extinction ratio of $5 \cdot 10^{-5}$ characterizing the polarization purity. The high bandwidth of 800 kHz of the phase and intensity servo loops enables fast transport operations on the microsecond scale. A waveform generator (Agilent, 33600A) and a direct digital synthesizer (Analog Devices, EVAL-AD9954) allow the programming of the timing-critical

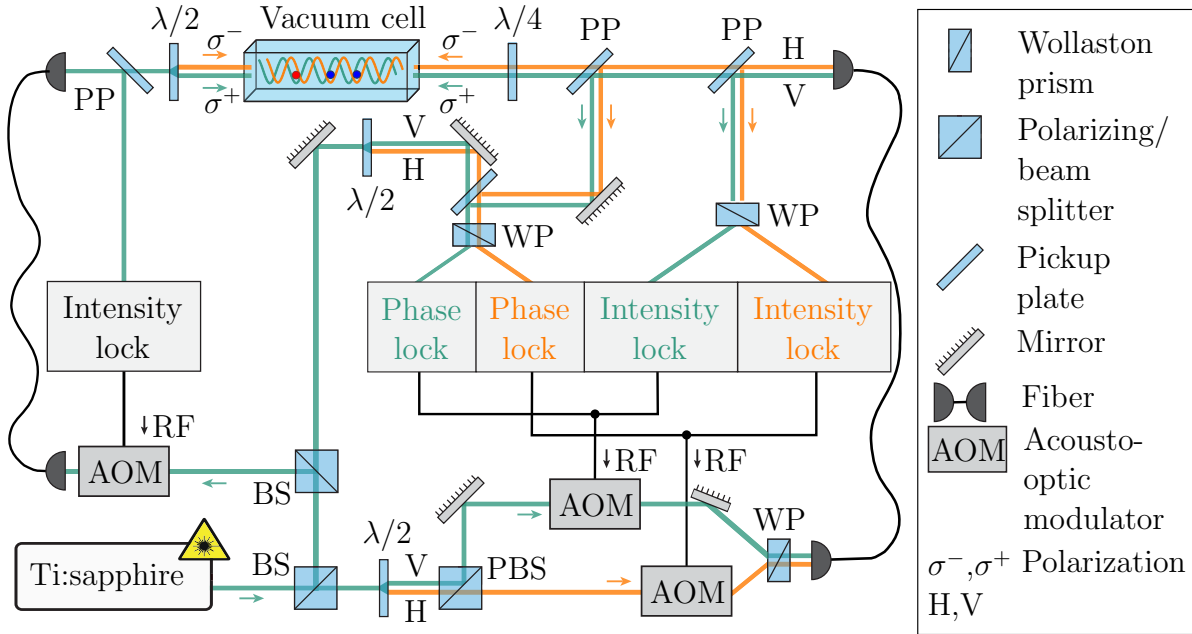


Figure 5.4: Experimental apparatus of the state-dependent lattices: The output of a titanium-sapphire laser system is split to generate both lattices. An intensity-stabilized ($\sigma^+ + \sigma^-$)-polarized running wave of constant frequency enters the vacuum cell from the left. The σ^+ - and σ^- -polarized beam from the right side is individually controlled. Parts of the light are extracted and detected with a photodiode in order to control the intensity. In order to control the phase, a beat signal between the undisturbed output of the laser and the frequency shifted beam is detected. A detailed view of the lock systems is shown in Fig. 5.5. The phase and intensity control loops set the frequency and amplitude of a radio frequency (RF) driving three acousto-optic modulators (AOM) to dynamically steer the trap depths and relative positions of the state-dependent lattices.

| Setup | | State-dependent setup | | | |
|-----------------------|------------------------|-----------------------|-------|------|----------------------------------|
| Direction | | x | y | z | |
| Trap wavelength | λ_{DT} | - | 865.9 | - | nm |
| Detuning from D2 line | Δ_{R} | - | -11 | - | $2\pi \cdot \text{THz}$ |
| Trapping frequency | Ω_{trap} | 1 | 115 | 1 | $2\pi \cdot \text{kHz}$ |
| Lamb-Dicke parameter | η | 1.44 | 0.13 | 1.44 | |
| Trap depth | U | 45 | 79 | 45 | $k_{\text{B}} \cdot \mu\text{K}$ |
| Waist | w_{DT} | - | 17 | - | μm |
| Powers | P_{DT} | - | 3 | - | mW |

Table 5.1: Summary of the trap properties in the state-dependent lattice system. In the experiment we operate two identical red-detuned spin-dependent traps along the y -direction.

transport ramps with high precision for amplitude and phase modulation. As a preparatory step in each measurement, the overlap of both lattices is automatically optimized by the phase control setup.

The state of an atom is detected by fluorescence imaging. It is performed in a deep trapping potential of $U = k_{\text{B}} \cdot 370 \mu\text{K}$ to shorten the exposure time to 500 ms without heating the atoms out of the trap. For the experimental sequences, the trapping potential is adiabatically lowered by the intensity control setup down to $U = k_{\text{B}} \cdot 47 \mu\text{K}$ [30]. This reduces off-resonant scattering of the trapping laser photons by the atoms, but the system still remain in the Lamb-Dicke regime. The parameters of the traps are summarized in Tab. 5.1.

5.5 Phase and intensity control systems

The phase and intensity control systems play a key role in the overall system and thus is described here in more detail. The control systems to drive phase and intensity ramps are based on an analog proportional-integral-derivative feedback loop (PID controller: Vescent Photonics, D2-125 laser servo) as shown in Fig. 5.5. The intensity of the laser beams is recorded with a photodiode (PD) and the signal is subtracted from a predefined set value V_{DC} , which serves as the error signal of the PID loop (bandwidth 10 MHz). The output of the PID controller steers the amplitude of an acousto-optic modulator (AOM) that controls the intensity of the laser beam. In the case of the phase control system, a beat signal is recorded at 80 MHz with a fast photodiode (FPD) between the undisturbed output of the laser and the frequency shifted proportion driving the dipole trap. A bias tee

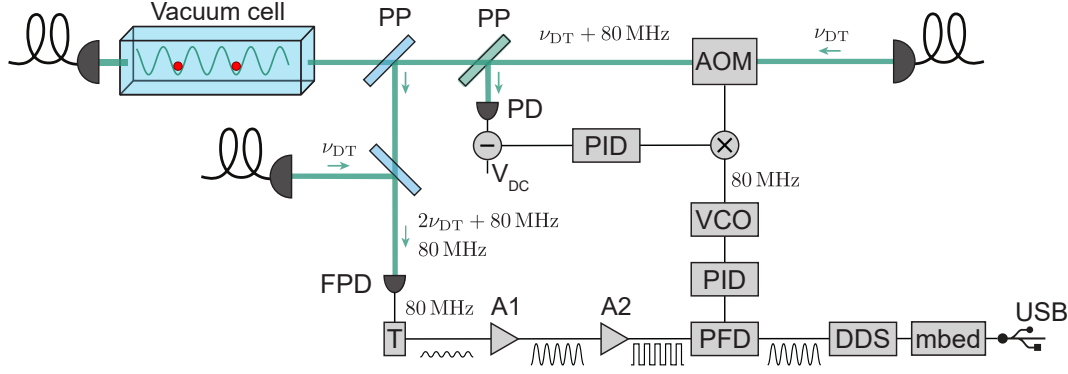


Figure 5.5: A detailed view of the intensity and phase control loop. This setup is installed twice and controls each synthesized arm of the σ^+ - and σ^- -polarized lattice. The acousto-optic modulator (AOM) controls the phase and amplitude of the laser beam. Parts of the light are extracted with a pickup plate (PP) and detected with a photodiode (PD) or a fast photodiode (FPD). In the amplitude control loop, the signal is subtracted from a computer-controlled reference voltage V_{DC} . The signal serves as the error signal of a proportional-integral-derivative controller (PID). In order to stabilize the phase, a beat signal between the undisturbed output of the laser and the frequency shifted proportion is recorded. A bias tee only passes the radio-frequency signal. A low-noise amplifier (A1) and a limiting amplifier (A2) in series provide a constant output signal at the beating frequency independent of the laser intensities. A phase frequency discriminator (PFD) compares this signal to the programmed waveform of a direct digital synthesizer (DDS), which serves as the error signal for the phase control loop. The PID drives a voltage controlled oscillator (VCO). The figure is taken with kind permission from the thesis of Robens [30].

(T) only passes the radio-frequency signal. A low-noise amplifier (A1) and a limiting amplifier (A2) in series provide a constant output signal at the beating frequency independent of the laser intensities, which produces the beating signal. A phase frequency discriminator (PFD) compares this signal to the programmed waveform of a direct digital synthesizer (DDS), which is stabilized to a 10 MHz rubidium clock. This signal serves as the error signal of the PID loop, whose output drives a voltage controlled oscillator (VCO). The frequency and amplitude of the RF frequency, which drives the AOM, are two independent controllable quantities. Therefore, the frequency generated by the VCO of the phase control loop can be combined with the amplitude signal from the intensity control loop. If we program any arbitrary driving ramp $u(t)$, the control loops do not respond instantaneously due to a delay time and limited control loop bandwidth. With an accurate knowledge of the response of such a dynamical system (LTI), which

is linear and time-invariant in first order approximation, we can consider these effects to reproduce the optimal driving ramps with highest precision.

Signal processing: Measurement of the impulse response

In this work, we need to be able to operate arbitrary transport ramps. They are generated by the intensity and phase control system. In order to have full control over the generated ramps, we need to know the exact response of the system. The input and output signals of the system can be:

$$\begin{aligned} u(t) &= \{U_{\text{IN}}^{\sigma^+}, U_{\text{IN}}^{\sigma^-}, \varphi_{\text{IN}}^{\sigma^+}, \varphi_{\text{IN}}^{\sigma^-}\} \quad , \\ y(t) &= \{U^{\sigma^+}, U^{\sigma^-}, \varphi^{\sigma^+}, \varphi^{\sigma^-}\} \quad . \end{aligned} \quad (5.6)$$

They define the trap depths and phases $\{U^\uparrow, U^\downarrow, \varphi^\uparrow, \varphi^\downarrow\}$ that both spin species experience following eq. (5.5) and (5.4).

In signal processing, the relation between input $U(t)$ and output $y(t)$ is formulated by the convolution theory [84]:

$$y(t) = (u * g)(t) = \int_{-\infty}^{\infty} u(\tau)g(t - \tau)d\tau \quad . \quad (5.7)$$

The impulse response function of the system $g(t)$ is defined as the output function of an impulse $\delta(t)$ as the input. The impulse response function can be measured by applying a Heavyside step function $\Theta(t)$ and recording the step response $y(t) = s_\Theta(t)$ by an out-of-loop photodiode. The impulse response is then determined by the derivative of the step response:

$$g(t) = \frac{d}{dt} (\Theta * g)(t) = \frac{d}{dt} s_\Theta(t) \quad . \quad (5.8)$$

The measurement of the step response and its derivative is shown in Fig. 5.6. The numerically derived derivative shows noise, which results from the noise of the photodiode signal. To overcome this, the measurement of the impulse response function is further improved by a transfer function fitting model provided by the Optimization Toolbox from MATLAB. The model function is described in the complex frequency space of $s = \sigma_s + i\omega_s$, where ω_s describes a frequency with a damping characterized by σ_s . The mapping is performed by a Laplace transform:

$$Y(s) = \mathcal{L}[y(t)] = \int_0^{\infty} e^{-st}y(t)dt \quad . \quad (5.9)$$

The input-output relation simplifies to

$$Y(s) = G(s)U(s) \quad (5.10)$$

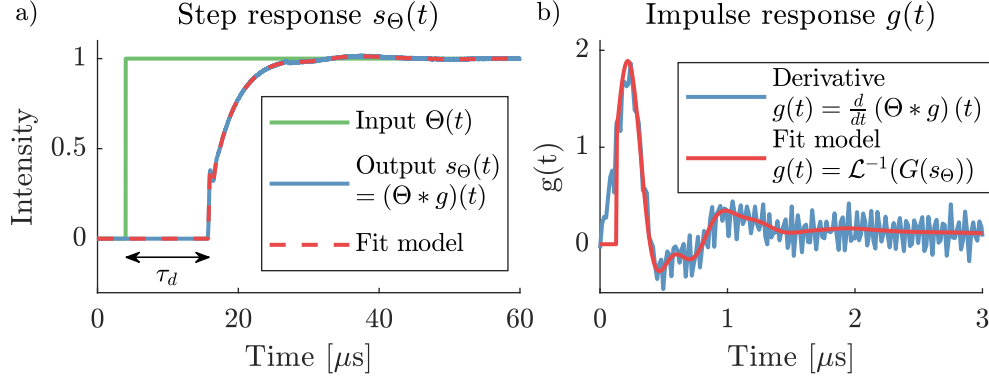


Figure 5.6: Fit of the step response from the intensity control setup of the σ^- -polarized lattice arm: (a) The input signal $u(t)$ is a Heavyside unit step function (green) and the measured step response $s_\Theta(t)$ delayed by τ_d is recorded with an out-of-loop photodiode (blue). (b) The impulse response determined by a simple derivative (blue) shows a higher noise floor than a fit of the transfer model function (red) from eq. (5.11). The fit model result is also shown as a step response (red).

The transfer function $G(s)$ is the Laplace transform of the impulse response function. $U(s)$ is the input signal in the complex frequency space. The transfer function fit model considers a delay time τ_d between the input and output signal and is further described by two polynomials $A(s)$ and $B(s)$:

$$\begin{aligned} G(s) &= e^{-s\tau_d} \frac{B(s)}{A(s)} \\ &= e^{-s\tau_d} \frac{b_0 + b_1s + b_2s^2 + \dots}{1 + a_1s + a_2s^2 + \dots} \end{aligned} \quad (5.11)$$

The parameters a_n and b_n are called poles and zeros. The poles contribute with oscillations in the system response. The number of zeros is in general smaller than the number of poles. An example of a system with more zeros than poles is the derivative term in a PID controller that amplifies high-frequencies including noise. In order to prevent noise amplification, the derivative part includes in general a low-pass filter to limit the high-frequency gain.

The impulse response function is determined in Fig. 5.6 by the inverse Laplace transform of the transfer function model:

$$\begin{aligned} \text{impulse response } g(t) &= \mathcal{L}^{-1}[G(s)] \quad , \\ \text{step response } s_\Theta(t) &= (\Theta * \mathcal{L}^{-1}[G(s_\Theta)])(t) \quad . \end{aligned} \quad (5.12)$$

The result of this measurement for all four control loops for intensity and phase of both lattices is shown in Fig. 5.7. Slow linear transport ramps are directly

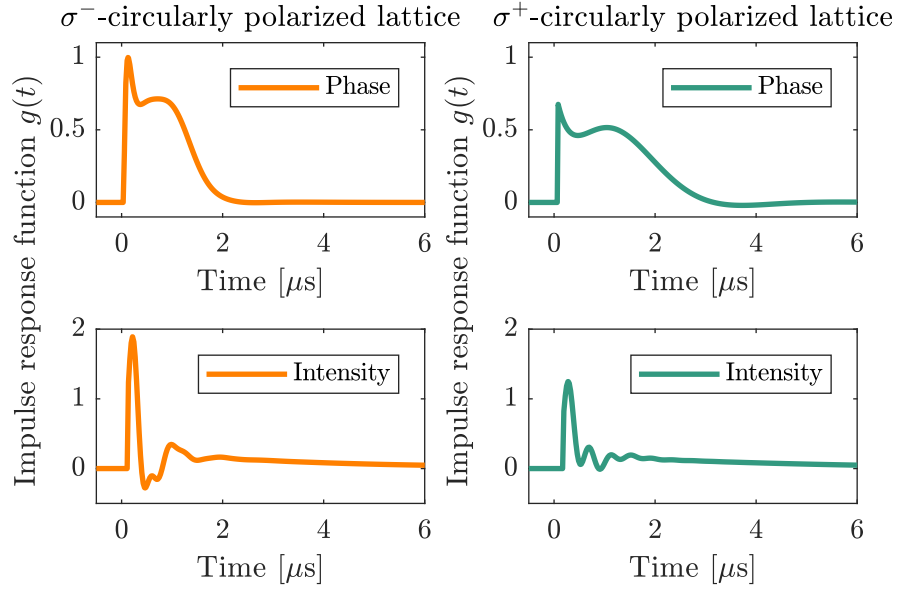


Figure 5.7: Fit of the impulse response functions $g(t)$ by the Optimization Toolbox from MATLAB of all for control systems: intensity (trap depth) and phase (trap position) for both synthesized σ^+ - and σ^- -polarized dipole trap arms. The result is used to improve the reproduction of desired arbitrary transport ramps.

applied as $u(t)$ and agree in good approximation with $y(t)$. However, for complex control ramps, as required for optimal control transport, they are deconvoluted to determine the input signal to the DDS of both synthesized arms. For non-complex signals the Laplace transform is equal to a Fourier transform. All processed signals in the experiments are real, such that:

$$U(s) = \frac{\mathcal{L}[y(t)]}{\mathcal{L}[g(t)]} = \frac{\mathcal{F}[y(t)]}{\mathcal{F}[g(t)]} \quad , \quad (5.13)$$

$$u(t) = \mathcal{L}^{-1}[U(s)] = \mathcal{F}^{-1}[U(s)] \quad .$$

The gained knowledge of all impulse responses of the control systems is needed to generate optimal control ramps in chapter 7.

In the following chapter, the state-dependent lattices are used to demonstrate microwave sideband cooling into the ground state along the state-dependent lattice direction. The ground state is a well-defined quantum state which is used in quantum walk and single atom interferometer experiments.

CHAPTER 6

MICROWAVE SIDEBAND COOLING OF NEUTRAL ATOMS

Microwave sideband cooling is another method to cool atoms into the vibrational ground state in a trapping potential. In comparison to Raman sideband cooling, the cooling using microwave sideband coupling shows several advantages: The longterm stability of microwave fields is better. Additionally maintenance of the microwave setup requires less effort due to the absence of optical phase and intensity locks. These are necessary to compensate relative frequency drifts of the Raman lasers and power fluctuations due to mechanical drift of optical components in the beam path. Furthermore, the photon microwave field is highly homogeneous along the lattice compared to the tightly focused laser beams. The reduced homogeneity of the Raman Rabi frequency results in a shorter coherence time. Microwave fields are the perfect tool in a state-dependent lattice experiment to couple vibrational sidebands. A microwave setup already exists to perform hyperfine state manipulations and to address atoms in individual potential wells. The ladder method originates from the nuclear magnetic resonance technique and uses a microwave field with a superimposed high gradient magnetic field along the lattice axis [85]. Compared to the previously discussed Raman sideband cooling technique in chapter 4, the microwave photon recoil energy with the wavenumber $k_{\text{MW}} = 2\pi/\lambda_{\text{MW}}$ is too weak to drive sidebands efficiently, and only a carrier transition is driven:

$$H_{\text{FC}}^{\Delta k} = e^{k_{\text{MW}}\hat{x}} \approx \hat{\mathbb{1}} + \mathcal{O}(10^{-5}) \quad . \quad (6.1)$$

6.1 Fundamentals of microwave sideband cooling in a state-dependent lattice

The principle of microwave sideband cooling is based on coupling of sideband transition by a small spatial shift. This shift induces a mechanical force during

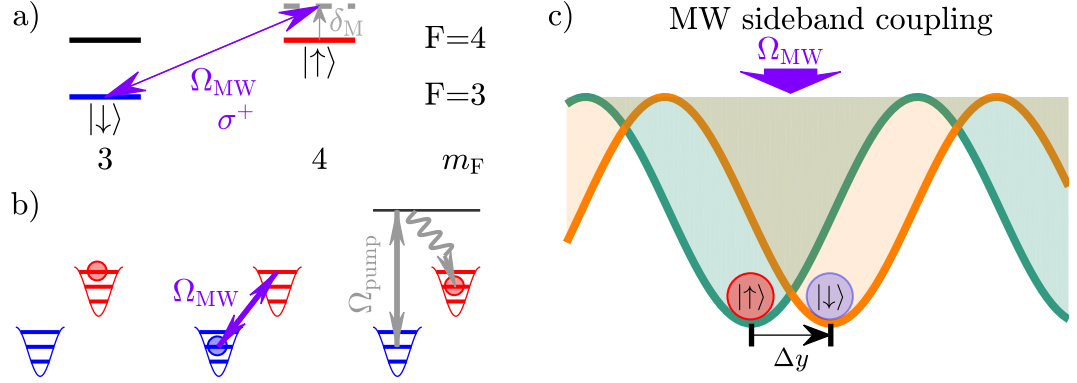


Figure 6.1: The principle of microwave sideband cooling: (a) The two qubit states $|\uparrow\rangle$ - and $|\downarrow\rangle$ -state are coherently coupled by a microwave field Ω_{MW} with a detuning δ_{M} . (b) A MW cooling cycle consists of a cooling sideband transition from the $|\uparrow\rangle$ to the $|\downarrow\rangle$. A strong optical pumping beam transfers the atom back without changing the vibrational state. (c) The sideband coupling is allowed for a spatial displacement Δy during the qubit state transfer.

a coherent state transfer [86]. The force results in an effective overlap between different vibrational wavefunctions, which is a prerequisite for sideband cooling.

Within a single electronic level, electronic dipole transitions generally vanish. However, selection rules can still allow magnetic dipole transitions, which are several orders of magnitude weaker, to couple states of the same electronic level directly, such as the ground states $|\uparrow\rangle$ - and $|\downarrow\rangle$ -state used in this work. The magnetic field \mathbf{B}_{MW} of a microwave field at $2\pi \cdot 9.2 \text{ GHz}$ couples to the magnetic dipole moment $\hat{\boldsymbol{\mu}}$ of the atom

$$\hat{H}_{F,m_F} = \hat{\boldsymbol{\mu}} \mathbf{B}_{\text{MW}} \quad . \quad (6.2)$$

During the microwave transition, the atom changes its spin state as shown in Fig. 6.1(a). The wavefunction is distorted by the spatial displacement during the state transfer. The translation operator describes the Frank-Condon Hamiltonian which initiates an overlap between vibrational states $\langle n' | \hat{H}_{\text{FC}} | n \rangle$:

$$\hat{H}_{\text{FC}}^{\Delta y} = \hat{T}^{\Delta y} = \sum_{y,n} |y + \Delta y, n + \Delta n\rangle_{|\downarrow\rangle} \langle y, n |_{|\uparrow\rangle} + \text{h.c.} \quad . \quad (6.3)$$

The state $|y, n\rangle$ describes the position y and the vibrational state n . During the state transfer, the atom can change the vibrational state by Δn , when we introduce a spatial shift Δy during the coherent transfer. Since the state-dependent lattice is not ideal, the state $|y, n\rangle$ is slightly different for the $|\uparrow\rangle$ - and $|\downarrow\rangle$ -state, which is indicated by the subscript. To get an intuitive picture of the coupling between vibrational states, the potential is approximated by a harmonic potential. In the

Lamb-Dicke regime, the momentum operator of the atomic center-of-mass motion \hat{k} is expressed by

$$\hat{k} = \frac{\hat{p}}{\hbar} \approx \sqrt{\frac{m_{\text{Cs}}\Omega_{\text{trap}}}{2\hbar}}(\hat{b}_y^\dagger - \hat{b}_y)\epsilon_y \quad . \quad (6.4)$$

Using the momentum operator as the generator of translation allows us to rewrite the translation operator in momentum space:

$$\begin{aligned} \hat{T}^{\Delta y} &= e^{i\hat{k}\Delta y} \\ &= \hat{1}_y + i\hat{k}\Delta y + \dots \\ &\approx \hat{1}_y + 0.5 \cdot i(\hat{b}_y^\dagger + \hat{b}_y) \quad . \end{aligned} \quad (6.5)$$

The unitary operator $\hat{1}$ describes the carrier transition and the second term represents the two first-order sidebands. The expression has a similar form as the Franck-Condon operator for Raman sideband cooling (see eq. (4.6)) with the exception that $\hat{T}^{\Delta y}$ operates in momentum space.

6.2 One-dimensional temperature model

Similar to the proceeding for Raman sideband cooling, I derive a new model for microwave sideband cooling. By considering the anharmonicity of the traps and the dependency of the coupling strength from different vibrational states, it improves the analysis of the experimental data. The mean temperature is determined from the probability distribution of an atomic ensemble over the vibrational state. The occupation probabilities $p(n)$ are measured by one-dimensional microwave sideband spectroscopy along the lattice direction y .

As before the state under study is described by the amplitudes c_n and the vibrational states $|n_\uparrow\rangle$

$$|\psi(0)\rangle = \sum_{n_\uparrow}^{\infty} c_{n_\uparrow} |n_\uparrow\rangle \otimes |\uparrow\rangle \quad . \quad (6.6)$$

The subscript refers to the fact, that the eigenstates can be different for the two spin states. This state is coherently driven by the microwave field and mapped onto the internal state $|n_\downarrow\rangle \otimes |\downarrow\rangle$. The operation is described in the general form of a Rabi oscillation with a phase θ :

$$|\psi(t)\rangle = \sum_{n_\uparrow, n_\downarrow} c_{n_\uparrow} \cos\left(\frac{\Omega_{n_\downarrow, n_\uparrow}}{2}t\right) |n_\uparrow, \uparrow\rangle + e^{i\theta} c_{n_\uparrow} \sin\left(\frac{\Omega_{n_\downarrow, n_\uparrow}}{2}t\right) |n_\downarrow, \downarrow\rangle \quad . \quad (6.7)$$

The coupling strength $\Omega_{n_\downarrow, n_\uparrow}$ follows from eq. (4.3) and eq. (6.5)

$$\begin{aligned}\hbar\Omega_{n_\downarrow, n_\uparrow} &= \langle \downarrow | \hat{H}_{F, m_F} | \uparrow \rangle \cdot \langle n_\downarrow | e^{i\mathbf{k}\Delta\mathbf{y}} | n_\uparrow \rangle \\ &= \hbar\Omega_0 \cdot FC_{n_\downarrow, n_\uparrow} .\end{aligned}\tag{6.8}$$

The Franck-Condon factor $FC_{n_\downarrow, n_\uparrow}$ describes the overlap between the corresponding eigenstates. For a well-known lattice shift and given trap depths U^\uparrow and U^\downarrow the factor is determined numerically. A simulation in Fig. 6.2(a) demonstrates the dependency of the Franck-Condon factor on the lattice shift. The Franck-Condon factor increases for the size of the lattice shift. A maximum is reached at different lattice shifts for the three simulated transitions. The optimal lattice shift reduces with higher initial vibrational state. During the cooling process, the vibrational state is reduced in each cooling cycle by one vibrational quantum. A high coupling strength is needed for all vibrational states. For small lattice shift, the Franck Condon factor for a trap depth of $k_B \cdot 80 \mu\text{K}$ is very homogeneous over vibrational levels but also inefficient as shown in Fig. 6.2(b). High lattice shifts of more than 50 nm, on the other hand, even cause the coupling to drop back to zero for certain vibrational states. For our experiments, we chose 17 nm as a good compromise.

The internal state is determined by the push-out state detection as a measure for the mapped state. The probability, that the state under study is coherently transferred into the $|\downarrow\rangle$ -state by a resonant driving is given by

$$\begin{aligned}P_\downarrow(t) &= |\langle \psi(t) | n_\downarrow, \downarrow \rangle|^2 \\ &= \sum_{n_\downarrow, n_\uparrow} |c_{n_\uparrow}|^2 \sin^2 \left(\frac{\Omega_{n_\downarrow, n_\uparrow}}{2} t \right) \\ &= \sum_{n_\downarrow, n_\uparrow} p(n_\uparrow) \sin^2 \left(\frac{\Omega_{n_\downarrow, n_\uparrow}}{2} t \right) .\end{aligned}\tag{6.9}$$

For simplicity, I assume Gaussian shaped resonance peaks with a Gaussian width σ , an offset frequency ν_0 and an amplitude A . The measured spectrum is then determined by

$$\mathcal{S}(\nu) = A \cdot \sum_{n_\downarrow, n_\uparrow} P_\downarrow(t) \cdot \exp \left(-\frac{(\nu - \nu_{n_\downarrow, n_\uparrow} - \nu_0)^2}{2\sigma^2} \right) .\tag{6.10}$$

The atomic transition frequencies ν_{n_x, n'_x} and ν_{n_y, n'_y} are numerically derived by solving the stationary Schrödinger equation from eq. (4.2). If the atoms are in thermal equilibrium, the occupation of the vibrational states is distributed according to a

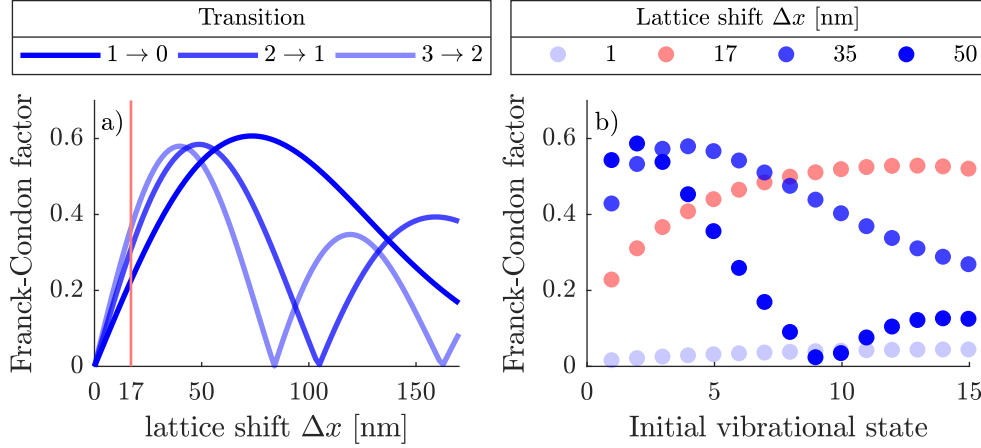


Figure 6.2: Franck-Condon factor for microwave sideband cooling for different lattice shifts and vibrational states for a trapping potential of $k_B \cdot 80 \mu\text{K}$: (a) The Franck-Condon factor of different cooling transition reaches a maximum for different lattice shifts. The optimal lattice shift reduces with higher initial vibrational state. As demonstrated in (b) the Franck Condon factor is very homogeneous for small lattice shift but also inefficient. High lattice shifts of more than 50 nm, on the other hand, even cause the coupling to drop back to zero for certain vibrational states. For our experiments, we chose 17 nm as a good compromise (red).

Boltzmann distribution:

$$p(n_{\uparrow/\downarrow}, T^*) = \frac{e^{-\frac{E_{n,\uparrow/\downarrow}}{k_B T^*}}}{\sum_{n_{\uparrow/\downarrow}=0}^{\infty} e^{-\frac{E_{n,\uparrow/\downarrow}}{k_B T^*}}} \quad (6.11)$$

In the following, I describe how we measure the microwave sideband spectrum for the first order sidebands and determine the temperature with this derived model.

6.3 Measurement of one-dimensional microwave ground state cooling

In order to determine the probability distribution of the vibrational state occupation, we conduct a microwave sideband spectrum. In the measurement sequence, all atoms are prepared in the $|\uparrow\rangle$ -state and the lattices are shifted apart by 17 nm. After a Gaussian shaped microwave transfer pulse, the lattices are overlapped again. The population in the $|\downarrow\rangle$ -state is measured with the push-out detection technique.

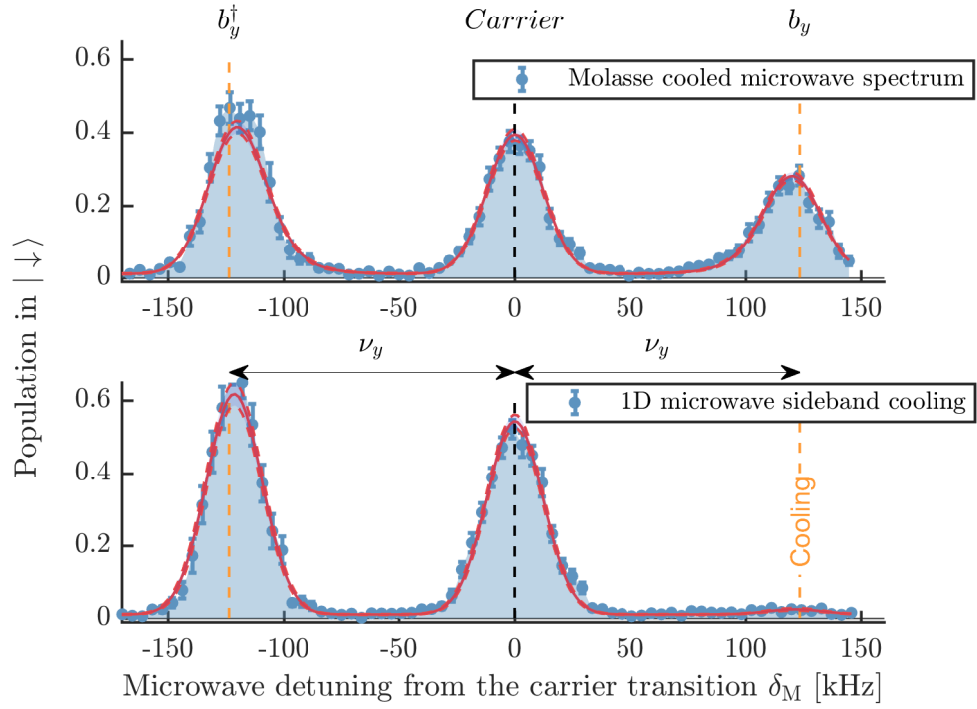


Figure 6.3: Measurement of longitudinal microwave sideband cooling into the ground state in the state-dependent lattice experiment: The red line is a fit following the model in eq. (6.10), which takes into account the anharmonic nature of our lattice. For comparison: the position marks of the sideband corresponds to the trap frequency of a harmonic trap with the same trap depth. The anharmonicity of the dipole trap manifests for different Boltzmann distributed mean vibrational states in a frequency shift of the sideband peaks and an asymmetric broadening. The carrier sideband height is not a free fit parameter. After cooling the height is reduced. This is due to the fact, that the Rabi frequency depends on the vibrational state.

A resulting spectrum without microwave cooling is shown in Fig. 6.3(a) for a trap depth of $k_B \cdot 90 \mu\text{K}$. The spectrum shows three distinctive peaks. The central peak is the carrier transition. The peak to the left is the heating sideband b_y^\dagger and the peak to the right is the cooling sideband b_y . The Gaussian transfer pulse with a duration of $90 \mu\text{s}$ and a Gaussian width of $9 \mu\text{s}$ is optimized for a maximum transfer probability on the first sideband. Decoherences dominated by the T_2 -time of $30 \mu\text{s}$ reduces the maximum sideband height to 65 %. The one-dimensional temperature model is shown as a red line. For molasse cooling, I experimentally achieve a ground state population of $(33 \pm 2)\%$ and a mean vibrational occupation number of $\bar{n}_y = 2.1 \pm 0.2$ along the lattice direction.

In a second measurement, a sideband cooling pulse in the shifted lattice is applied for 20 ms. The result is shown Fig. 6.3(b). The height of the cooling sideband significantly reduces. The carrier sideband height is not a free fit parameter. After cooling the height is increased. This is due to the fact, that the Rabi frequency depends on the vibrational state. Microwave sideband cooling improves the ground state occupation to $(98 \pm 1)\%$, which corresponds to a mean vibrational occupation number of $\bar{n}_y = 0.02 \pm 0.01$. Likewise, the width of the sidebands decreases and the position of the sidebands shifts further away from the carrier transition frequency due to the anharmonicity of the trapping potential. This shows, that the developed two-dimensional temperature model is able to determine the properties of trapped atoms, such as the trap frequency and the ground state population, with higher accuracy, since it takes the anharmonicity into account.

6.4 Conclusion and outlook

In this chapter, I introduced the principle of microwave sideband cooling in state-dependent lattices. I developed a new one-dimensional temperature model in a similar way as for Raman sideband cooling. The model considers the anharmonic shape of the lattice and is based on the full Hamiltonian of the system leading to a better interpretation of the measured microwave sideband spectrum. From the measurement with this existing setup, I determine a ground state population of $(98 \pm 1)\%$.

In order to cool all three dimensions, Raman sideband cooling was recently demonstrated with $(94 \pm 4)\%$ ground state population [30] in the radial direction: For resolved Raman sideband cooling, a blue-detuned hollow beam dipole trap is overlapped with the state-dependent lattice to increase the radial trap frequency to $2\pi \cdot 20 \text{ kHz}$ and the Lamb-Dicke parameter to $\eta = 0.3$. Two orthogonal phase locked Raman running waves cool the atoms to in radial direction. However, the radial cooling limit can be further improved up to a factor of five by carrier-free Raman sideband cooling, which is demonstrated in chapter 4.3. A radially aligned Raman beam locked to the blue-detuned hollow beam dipole trap would replace the current Raman system.

In the next chapter, I use optimal control to transport atoms over one lattice site while maintaining the ground state population with high fidelity. The fidelity measurement additionally allows to determine the radial temperature with high precision.

CHAPTER 7

OPTIMAL QUANTUM CONTROL FOR FAST ATOM TRANSPORT

Complex dynamical systems are often desired to be controlled using analytical solutions. Analytical methods have the potential to give exact solutions. However, the more complex the system gets, the more many assumptions and approximations have to be made to derive an analytical solution. In some of those cases, a numerical approach can be more feasible. If an efficient representation of the dynamics exists, optimal control theory is a powerful mathematical tool, to go from analytical guesses to optimal solutions for a variety of different research fields. In particular, time-optimal control of linear systems found its path into a large spectrum of applications in chemistry, aerospace, robotic engineering, economics, mathematics and physics [87–93]. A small analogy from our daily life is intended to illustrate the principle of optimal control: consider a waiter serving glasses of champagne using a tray. His goal is to transport the drinks from the counter to the guests without spilling the glasses, which for our motivated waiter defines the target state. At this point, we can also introduce the cost function, which accounts for how well we have reached the target state. In our example this would be the amount of champagne lost during the transport. A beginner would move very constantly and slowly, in order to keep the liquid almost at rest in the glass, which is equivalent to an adiabatic solution. However, a more experienced waiter can serve the champagne without spilling them much faster by adjusting his speed and balancing the tray with his hand. This is an optimal control solution. In control theory, the speed and position of the hand are the control parameters to be optimized. This example shows that it is not only possible to optimize the desired system outcome, it is even capable to speed up the process with little loss of fidelity. Optimal control theory has found successful applications in optimal quantum control with active manipulation of physical and chemical processes on the atomic and molecular scale [94].

In general, the time-evolution of a dynamical system is described in the form of differential equations. Optimal control accomplishes the task by numerically im-

proving the control solutions of a system that starts in a well defined initial state and evolves into a desired state after a given amount of time. As an example in quantum chemistry, they have been demonstrated to shape femtosecond laser pulses to optimize chemical reactions [95–97]. The improvement towards faster and more robust laser pulses has also been applied in quantum physics in the domain of few ultracold atoms, such as the stabilization of molecules [98] and the control of quantum dots [99]. In combination with the raising field of machine-learning fast optimization has been achieved for the generation of a BEC [100].

7.1 The transport of an atomic wave packet in optical lattices

One task in our experiment is to transport an atom prepared in the ground state as fast as possible over a certain distance without heating it as shown in Fig. 7.1. One example is the quantum walk experiment. A quantum walk is the quantum analog of a classical random walk and can be regarded as a universal computational primitive. It builds a basic block for a series of quantum algorithms in quantum computing [101]. All our experiments are based on discrete operations, which are repeated in time. Discrete-time quantum walk experiments with single atoms in optical lattices, as performed with our system, coherently delocalize matter waves [57]. The basic quantum walk protocol consists of two building blocks: The coin operation brings an atom into a coherent superposition of the $|\uparrow\rangle$ - and $|\downarrow\rangle$ -state. The shift operation transports each spin component by a certain distance in opposite direction, which results in a controlled delocalization. Repeating this process many times, the quantum interference of the two-particle trajectories show quantum correlations that strongly differ from its classical counterpart. After a discrete number of coin and shift operations in a classical random walk, the probability to end up at a specific final position is given by a binomial distribution. In a discrete-time quantum walk, the quantum interference caused by the coherent superposition of the walker over different paths changes the spatial distribution. Ultimately, the amount of operations we can perform is given by the coherence time T_2 of up to $240\,\mu\text{s}$ [30] divided by the amount of time each operation lasts. Since optimal control theory also holds promise to make the control pulses robust against small experimental deviations, it seems a natural desire to shorten and optimize the operations as much as possible. Transporting the atoms using the state dependent optical lattice, is the most time consuming operation. In former experiments the transport required several tens of microseconds.

I demonstrate in this chapter, how the process can be significantly reduced in

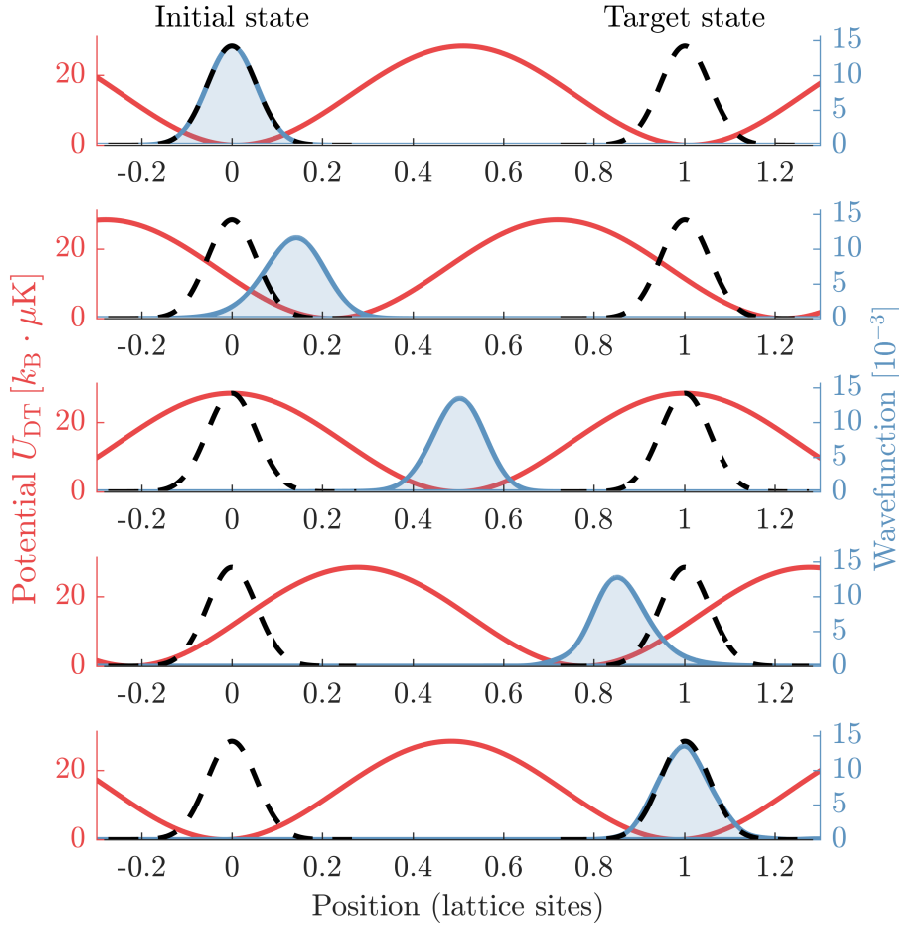


Figure 7.1: Simulation of an optimal control atom transport over one lattice site: The initial and final state are defined as the ground state. The optimal control transport ramp is optimized for a trap depth of $k_B \cdot 28.4 \mu\text{K}$ and a transport duration of $14.5 \mu\text{s}$ and reaches a transport fidelity of 99%). From top to bottom, the figures show the position of the lattice (red) and the normalized wave packet (blue) in equal time steps.

time and simultaneously improved in precision. In the first part, I introduce a measurement technique based on the previously discussed microwave sideband spectroscopy to quantify the transport fidelity of a driving ramp. I investigate the transport dynamics in case of linear driving ramps, as used in previous quantum walk experiments [57]. A strong dependency on the longitudinal trapping frequency and the dipole trap crosstalk for the different spin states was limiting

the transport time and fidelity.

With the high control of this setup and precise knowledge of the system, I derive a model to simulate the transport fidelity for an arbitrary transport ramp. With this model at hand, I use optimal control theory to derive driving ramps for arbitrary transport times and fidelities up to 99.9999%. The transport time is then limited only by the quantum speed limit. It describes a fundamental limit given by nature and is investigated in chapter 8.

For prospective quantum walk experiments with optimized transport ramps, I analyze the dynamics of multiple repetitions of the same driving ramp. Furthermore, to overcome even disregarded experimental imperfections, I demonstrate live optimal control of a driving ramp, where the system optimizes itself. For our experiment, this method can be used for large-distance optimal control transport, where the Hilbert space gets too large to be simulated by conventional computers in a reasonable time.

7.2 Theoretical model of the transport fidelity

In transport experiments, it is important that the transported particle reaches a certain target state. In this chapter, I derive a theoretical model of the transport fidelity.

The general definition of the transport fidelity \mathcal{F} is given by the squared overlap between the evolution of the initial state $|\psi_{\text{init}}\rangle$ after a time T with a target state $|\psi_{\text{target}}\rangle$:

$$\begin{aligned}\mathcal{F} &= |\langle \psi_{\text{target}} | \psi(T) \rangle|^2 \\ &= |\langle \psi_{\text{target}} | \hat{U}_{\text{evo}}(T) | \psi_{\text{init}} \rangle|^2 \\ &= |\langle \psi_{\text{target}} | \exp\left(-\frac{i}{\hbar} \int_0^T \hat{H}(t') dt'\right) | \psi_{\text{init}} \rangle|^2 \quad .\end{aligned}\tag{7.1}$$

The initial and target states are the normalized and real-valued vibrational ground states at different lattice site locations. The initial state is prepared in the vibrational ground state at the lattice position $d = 0$: $|\psi_{\text{init}}\rangle = |n = 0, d = 0\rangle$. The target position used in this work is shifted by one lattice site $\Delta d = \lambda_{\text{DT}}/2$ or multiple integers of this distance: $|\psi_{\text{target}}\rangle = |n = 0, d = \Delta d\rangle$. A detailed description of the numeric evaluation of these so-called Wannier states can be found in appendix A.2. The unitary time-evolution operator $\hat{U}_{\text{evo}}(T)$ is determined by the system Hamiltonian. In the laboratory frame, the one-particle Hamiltonian is given by the kinetic energy of the cesium atom with mass m_{Cs} and the potential energy of the sinusoidal lattice potential with the wave vector \mathbf{k} :

$$\hat{H} = \hat{T} + \hat{U} = \frac{\hat{\mathbf{p}}^2}{2m_{\text{Cs}}} + U_{\uparrow/\downarrow}(t) \cos^2((\mathbf{k}\hat{\mathbf{x}} - \varphi_{\uparrow/\downarrow}(t))/2) \quad .\tag{7.2}$$

The control fields that drive the transport ramps, are steered by the potential depth $U_{\uparrow/\downarrow}(t)$ and the phase $\varphi_{\uparrow/\downarrow}(t)$ for the $|\uparrow\rangle$ - or $|\downarrow\rangle$ -state respectively. In the next step, I decompose the evolution operator into a time-ordered product of operators with $t_0 < t_1 < t_2$:

$$\hat{U}_{\text{evo}}(t_2, t_0) = \hat{U}_{\text{evo}}(t_2, t_1) \hat{U}_{\text{evo}}(t_1, t_0) \quad . \quad (7.3)$$

This property allows to trace the evolution of the initial state in time, even though the Hamiltonian is time-dependent. The time steps Δt of the numeric integration must be chosen sufficiently small in order to assume a constant Hamiltonian over this time interval:

$$\begin{aligned} |\psi(t + \Delta t)\rangle &= \hat{U}_{\text{evo}}(t + \Delta t, t) |\psi(t)\rangle \\ &= \exp\left(-\frac{i}{\hbar} \int_t^{t+\Delta t} \hat{H}(t') dt'\right) |\psi(t)\rangle \\ &\approx \exp\left(-\frac{i}{\hbar} \left(\hat{T}\Delta t + \hat{U}\left(t + \frac{\Delta t}{2}\right)\Delta t\right)\right) |\psi(t)\rangle \quad . \end{aligned} \quad (7.4)$$

The kinetic energy term \hat{T} is time-independent and the potential energy term \hat{U} is approximated by the midpoint rule [102]. Both operators can not be simultaneously diagonalized in momentum and position space, which would be desired for a fast numeric integration. However, the kinetic term has a diagonal form in momentum space and the potential energy term in position space. Since both operators are arguments of an exponential function, the evaluation is nontrivial.

A general approach to solve the time-dependent Schrödinger equation is the split-operator exponential fast-Fourier transform method [103]. It splits the operator into a product of two terms in each representation, which then allows to use fast-Fourier transform to evaluate the actions of the operators in their respective local representation. In the following, the second order leapfrog composition is chosen following from the Baker-Campbell-Hausdorff expansion [104]:

$$\begin{aligned} \hat{U}_{\text{evo}}(t + \Delta t) &= \exp\left(-\frac{i}{\hbar} \hat{T}\Delta t\right) \cdot \exp\left(-\frac{i}{\hbar} \hat{U}\left(t + \frac{\Delta t}{2}\right)\Delta t\right) + \mathcal{O}(\Delta t^2) \\ &= \exp\left(-\frac{i}{\hbar} \frac{\hat{T}}{2}\Delta t\right) \cdot \exp\left(-\frac{i}{\hbar} \hat{U}\left(t + \frac{\Delta t}{2}\right)\Delta t\right) \cdot \exp\left(-\frac{i}{\hbar} \frac{\hat{T}}{2}\Delta t\right) \\ &\quad + \mathcal{O}(\Delta t^3) \\ &\approx \hat{U}_{\text{evo}}^{\hat{T}}(\hat{\mathbf{p}}) \quad \hat{U}_{\text{evo}}^{\hat{U}}(\hat{\mathbf{x}}) \quad \hat{U}_{\text{evo}}^{\hat{T}}(\hat{\mathbf{p}}) \quad . \end{aligned} \quad (7.5)$$

The time tracing of a state ψ is then computed with two additional Fourier transformations to evaluate the actions in their relative representation:

$$|\psi(x, t + \Delta t)\rangle \approx \hat{U}_{\text{evo}}^{\hat{T}}(\hat{\mathbf{x}}) \mathcal{F}^{-1} \left[\hat{U}_{\text{evo}}^{\hat{U}}(\hat{\mathbf{p}}) \mathcal{F} \left[\hat{U}_{\text{evo}}^{\hat{T}}(\hat{\mathbf{x}}) |\psi(x, t)\rangle \right] \right] \quad . \quad (7.6)$$

The energy during transport can be computed in a similar way:

$$E(t) \approx \mathcal{F}[\langle \psi(x, t) | \hat{T}(\hat{\mathbf{p}}) \mathcal{F}[\langle \psi(x, t) \rangle] + \langle \psi(x, t) | \hat{U}(t + \Delta t, \hat{\mathbf{x}}) | \psi(x, t) \rangle] . \quad (7.7)$$

Accuracy of the model

The accuracy of the simulation depends mainly on the approximation by the factorization of the evolution operator in eq. (7.5). It is possible to increase the precision to the order $\mathcal{O}(\Delta t^4)$ [105]. Furthermore, for numerical stability, the time increment Δt must be chosen small enough to ensure an accurate computation of the time-dependent wavefunction. Similarly, the spatial sampling interval Δx must be chosen small enough to accommodate the spatial bandwidth of the wavefunction. In the simulation, I assume a finite number of lattice sites. The boundary conditions are chosen to be periodic, which means, when a wave packet or parts of it are moving beyond the last lattice site, it reappears again in the first lattice site, and vice versa. Therefore, the number of lattice sites have to be chosen sufficiently large that the wavefunction is negligible on the grid boundary.

Transport fidelity for finite radial temperature

So far, the one-dimensional model neglects the radial degree of freedom of the atom in the lattice. The oscillation in the radial direction with a period of $2\pi/\Omega_{\text{rad}} = 1 \text{ ms}$ (see eq. (2.5)) is small compared to the transport duration of a few tens of microseconds and therefore, we can regard the atoms radial position as static during the transport. The radial position distribution $P_{\text{rad}}(\rho)$ in harmonic approximation is given by

$$P_{\text{rad}}(\rho) = \frac{\rho}{\sigma^2} \exp\left(\frac{-\rho^2}{2\sigma^2}\right) \quad (7.8)$$

$$\sigma = \sqrt{\frac{k_{\text{B}} T_{\text{rad}}}{m_{\text{Cs}} \Omega_{\text{rad}}^2}} = \sqrt{\frac{k_{\text{B}} T_{\text{rad}}}{4U_{\uparrow/\downarrow}}} w_{\text{DT}} ,$$

and depends on the radial temperature T_{rad} and the Gaussian dipole trap beam waist w_{DT} . For a finite radial temperature, the effective trap depth $U_{\text{DT}}(\rho)$ (see eq. (2.3)) changes depending on the radial distance ρ to the trap center. The further an atom is located away from the trap center, the smaller is the effective trap depth. Since the optimal control solution can only be optimized for one trap depth $U(t)$, the transport fidelity is reduced for other trap depths. The average transport fidelity is then determined by

$$\langle \mathcal{F} \rangle = \sum_{\rho} P_{\text{rad}}(\rho) \mathcal{F}(U_{\text{DT}}(\rho)) d\rho . \quad (7.9)$$

The strong dependency of the transport fidelity on the trap depth allows to determine the finite radial temperature with high precision. In the next chapter, I use this model to interpret the transport fidelity of linear transport of atoms.

7.3 Measurement of the transport fidelity

In order to determine the transport fidelity, the target state needs to be measured. In this work, target state is defined as the vibrational ground state in a certain lattice site.

In several ion experiments, transport schemes, which preserve the ground state have been demonstrated to shuttle atoms between different experimental regions with a separation of a few hundred micrometers [106–108]: With a linear ramp lasting just a few microseconds, the atom in the vibrational ground state of the trap is suddenly accelerated, then moved at a constant velocity and decelerated rapidly again. As expected, a high transport fidelity of the ground state population is observed at integer multiples of the period of atomic oscillations in the harmonic trap $2\pi/\Omega_{\text{trap}}$. For other transport durations, the atoms get highly excited. The excitations were measured using Raman sideband spectroscopy as introduced in chapter 4.

In our experiment, we typically use transport of single and a few atoms over a distances of half a lattice site up to several hundreds of lattice sites to generate low-entropy states [29], to demonstrate the violation of the Leggett-Garg inequality [109] or to perform quantum walk experiments [110], just to mention a few recent applications. In this work, I transport for simplicity a single atom in $|\uparrow\rangle$ - or $|\downarrow\rangle$ -state over one lattice site, which corresponds to $\lambda_{\text{DT}}/2 = 433 \text{ nm}$ as a benchmarking point. The second state-dependent lattice is kept at rest. To quantify the transport fidelity, I determine the ground state population before and after the transport. A fit of the derived one-dimensional temperature model (chapter 6.1) to a microwave sideband spectrum, determines the population occupation of all vibrational states $p(n)$. For a trap depth of $k_{\text{B}} \cdot 80 \mu\text{K}$, $n = 18$ bound states are expected by solving the stationary Schrödinger equation. Before transport the atom is well prepared close to the vibrational ground state. However, after transport the atoms are excited out of the thermal equilibrium and I assume a Gaussian distribution with the mean value μ and the standard deviation σ :

$$p(n) = \frac{1}{S} \exp\left(-\frac{(n - \mu)^2}{2\sigma^2}\right) \quad . \quad (7.10)$$

The one-dimensional temperature model determines this probability distribution. Without atom loss, the sum of the probability is one. A measurement of the atomic

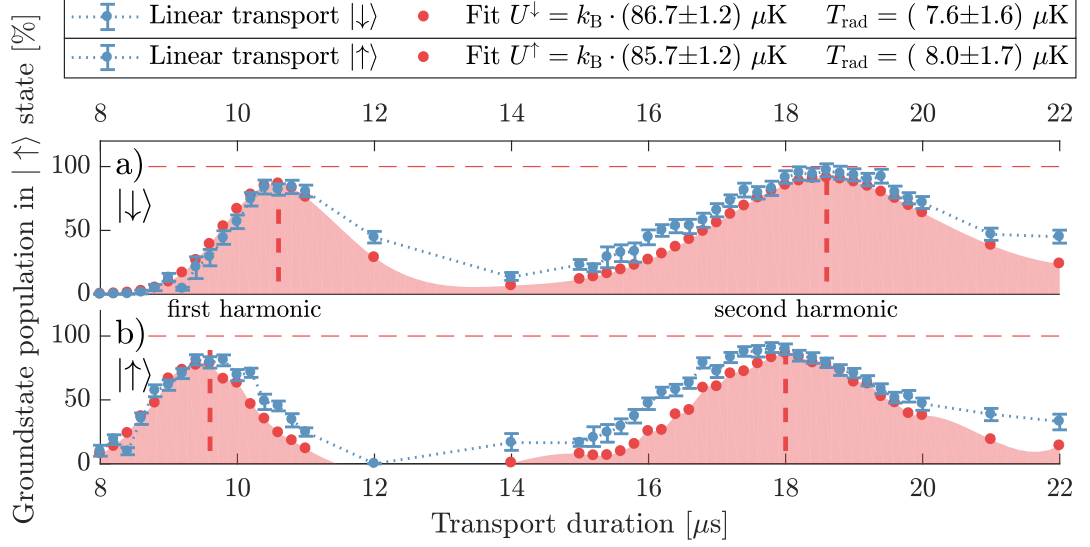


Figure 7.2: Measurement and simulation of the transport fidelity for different transport durations by using a linear transport ramp over one lattice site: (a) The transport fidelity is measured for the $|\downarrow\rangle$ -state (blue) and compared to the derived model in chapter 7.2. A high transport fidelity of the ground state population is observed at integer multiples of the period of atomic oscillations. The fidelity and robustness increases with higher harmonics. (b) The measured transport fidelity of the $|\uparrow\rangle$ -state shows a high transport fidelity for different transport durations. This is a result of the dipole trap crosstalk for the $|\downarrow\rangle$ -state, when both state-dependent lattices have the same trap depths.

survival rescales the probability distribution:

$$S = \sum_n p(n) \quad . \quad (7.11)$$

The ground state population manifests itself mainly in the ratio of the cooling and heating sideband peak heights as well as a small shift of their peak positions. To keep the measurement within a reasonable measurement time, I measure the sideband heights at two fixed frequencies, one at the cooling and one at the heating sideband frequency, for different driving ramps.

For a linear transport, the measured ground state occupation for variable transport durations together with a least square optimization of the previously introduced model in chapter 7.2 is shown in Fig. 7.2 for the $|\uparrow\rangle$ - and $|\downarrow\rangle$ -state. As expected, a high transport fidelity after transport is observed for the first two multiples of the oscillation period. The period is significantly different for both spin states. The difference is explained by the crosstalk of the state-dependent

lattice (see eq. (5.3)): The trapping potential for the $|\uparrow\rangle$ -state remains constant throughout the transport. However, for the $|\downarrow\rangle$ -state, the trap depth temporarily decreases to $7/8 U^\downarrow$ at half the transport distance as shown in Fig. 5.2. Although the lattice U_{DT}^σ is moved with constant velocity, the $|\downarrow\rangle$ -state is slightly accelerated and decelerated according to eq. (5.4). This crosstalk is also responsible that the periodic peaks for atoms in $|\downarrow\rangle$ -state are not equidistant. Therefore, it was not possible to achieve coherent transport of both atoms simultaneously using the first harmonic of the oscillation period in previous experiments. A transport duration at for the second or third harmonics was chosen instead. A second reason to choose a slower transport is an increased robustness against experimental imperfections, which is indicated by a broadening of the peaks. The experimentally obtained transport fidelity shows a remarkably good agreement with the theoretical analysis of the linear transport, making it therefore a reliable tool in the experiment to precisely extract the trap depth and radial temperature of the atoms. In the following, I will extend this model for an arbitrary driving ramp.

7.4 Optimal control theory for high transport fidelity

A main goal of this work is to preserve the ground state occupation of the atoms after transport with high fidelity. To derive optimal transport ramps, I use optimal control theory.

Optimal control theory aims to improve the steering of a desired quantum process. The optimization problem is formulated as a minimization problem and can be numerically approached by direct search methods. Two of the most commonly used algorithms are the Krotov-type method and the gradient ascent pulse engineering (GRAPE) algorithm [94]. The Krotov method is similar to the GRAPE algorithm, which is an iterative method with monotonic convergence. It has been used for example to generate control pulses for Bose-Einstein condensates [111]. GRAPE is applied for the design of pulse sequences in nuclear magnetic resonance spectroscopy and is based on an iterative gradient ascent procedure with many forward and backward propagations of the target functional [112]. The final error scales linearly with the number of algorithm iterations.

The computational method, I use for our system, is inspired by the chopped random-basis (CRAB) algorithm [113]. The numerical calculation is developed in cooperation with Antonio Negretti [114]. The technique is based on a numerical, iterative descent, where the error scales exponentially with the number of optimization parameters. While the control fields are usually discretized in time for the GRAPE and Krotov method, the CRAB algorithm expands the control in a

function basis, which significantly reduces the dimensionality and the computational effort.

Optimization algorithm

The basic idea optimal control theory is the minimization of a cost function \mathcal{C} defined in our case by the transport infidelity

$$\begin{aligned}\mathcal{C} &= 1 - \mathcal{F} \\ &= 1 - |\langle \psi_{\text{target}} | \hat{U}_{\text{evo}}(T) | \psi_{\text{init}} \rangle|^2.\end{aligned}\quad (7.12)$$

The fidelity \mathcal{F} was introduced in the previous chapter in eq. (7.1). In case the target states are unknown or described by a family of target states as for example in experiments with highly entangled states [115], desired properties or conditions of the target states can also define the cost function. For the CRAB algorithm [113], the control fields, which steer the system, are described by a function basis. This basis is chopped, in order to operate on a finite number M of basis functions. In order to optimize the transport fidelity, we parameterize the control fields, which are the potential depth $U_{\uparrow/\downarrow}(t)$ and the phase $\varphi_{\uparrow/\downarrow}(t)$. For a fast optimization success, the choice of the basis functions is crucial and a prior knowledge about the system is often necessary to restrict the solutions. As shown in appendix A.3, I prove that under the assumption that a quantum speed limit exists, a symmetric optimal control solution is found above this time limit. From this proof we gain insight in the properties of the control fields: Above the time limit, at least one solution for the phase ramp can be found, that is point symmetric. For the potential depth ramp we can find at least one axial symmetric driving ramp. Therefore, the Fourier series is a reasonable ansatz to determine a solution. The choice of this ansatz allows additionally to truncate the basis functions in a physically meaningful way. The maximum frequency is chosen as the system bandwidth of approximately 1 MHz. The lowest frequency is given by the time of the transport. The trap depth is then given by a constant offset $U_{\uparrow/\downarrow}^0$ modulated with sinus functions. The phase describes a linear ramp plus a modulation of the same basis functions with the control parameters $c = \{a_m, b_m\}$:

$$\begin{aligned}U_{\uparrow/\downarrow}(t, T) &= U_{\uparrow/\downarrow}^0 + \sum_{m=0}^M a_m \sin(\nu_m t), \quad t \in [0, T] \quad , \\ \varphi_{\uparrow/\downarrow}(t, T) &= \frac{2\pi}{T}t + \sum_{m=0}^M b_m \sin(\nu_m t), \quad t \in [0, T] \quad .\end{aligned}\quad (7.13)$$

The boundary conditions are defined as an initial phase $\varphi_{\uparrow/\downarrow}(t = 0) = 0$ and amplitude $U_{\uparrow/\downarrow}(t = 0) = U_{\uparrow/\downarrow}^0$ and final phase $\varphi_{\uparrow/\downarrow}(t = T) = 2\pi$ and amplitude

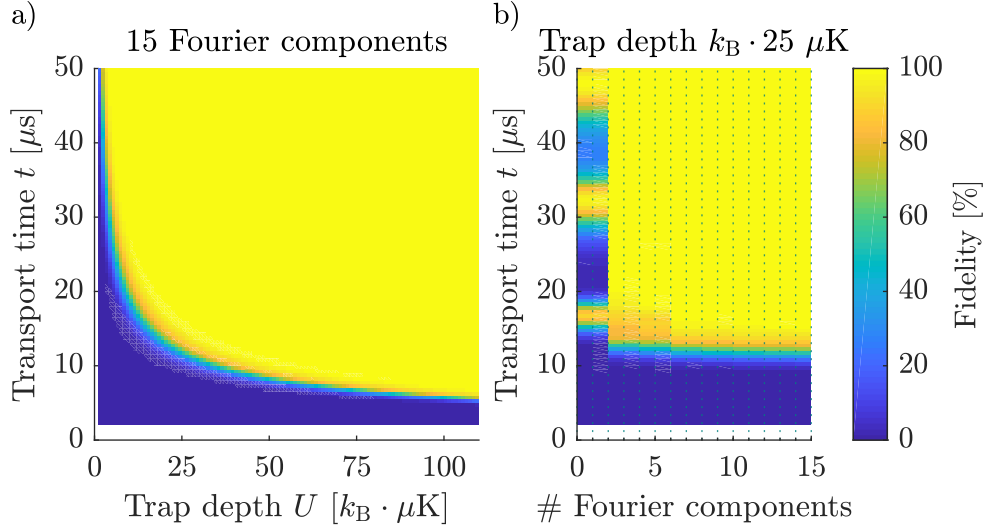


Figure 7.3: (a) Fidelity landscape of optimal control solutions for different trap depths and transport times by optimizing the phase of the transport ramps. A relatively sharp border is observed, where the fidelity starts to significantly reduce from 100 %. This is identified as the quantum speed limit. (b) The solution for different numbers of Fourier components is shown for a trap depth of $k_B \cdot 25 \mu\text{K}$. Zero components corresponds to a linear phase ramp. As expected, the point symmetry of the phase ramp reflects in a significant improvement for even Fourier components (point symmetric). For the measurements in this work, I optimize 10 Fourier components.

$U_{\uparrow/\downarrow}(t = T) = U_{\uparrow/\downarrow}^0$. These constraints are satisfied for $\nu_m = m\pi/T$. Furthermore, we restrict the maximum slope of the phase ramp of $0.838 \text{ rad}/\mu\text{s}$, which is given by the bandwidth of the phase lock loop, and a maximum trap depth limited by the available laser power. The conventional CRAB algorithm needs less optimization parameters than this approach, since the basis is randomized by a random number that breaks the orthonormality of the functions and leads to a faster convergence and higher bandwidth [113]. However, for a transport over hundreds of lattice sites, the number of optimization parameters has to be constraint further, which can introduce local minima into the solution space [116] and impede the search for an optimal control solution. A more sophisticated method is the dressed CRAB algorithm [117], which uses multiple sets of different basis functions in order to escape from local minima with a reduced number of optimization parameters.

However, for transport experiments over one lattice site, the number of search iterations for the fixed basis functions described in eq. (7.13) is similarly fast as the conventional CRAB algorithm. The nonlinear programming solver "fmincon" from MATLAB is applied as a direct search solver to approximate the solution to this

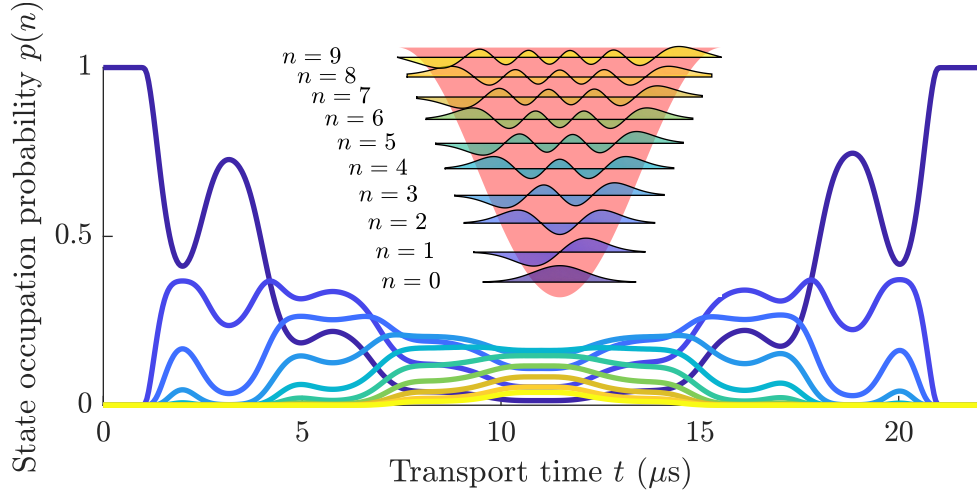


Figure 7.4: State occupation during optimal control transport: The optimal control solution is optimized for a trap depth of $k_B \cdot 25 \mu\text{K}$ and a transport time of $20 \mu\text{s}$ close to the quantum speed limit. An atom initialized in the ground state is highly excited during the transport, which is shown by the state occupation probability for the different bound states in the lattice. At the end of the ramp, the state evolves from high excited states back down into the ground state.

optimal control problem. It is based on the interior-point algorithm. Figure 7.3(a) shows a fidelity landscape of optimal control transport ramps for different trap depths and transport times. Above a certain transport time, which is defined as the quantum speed limit, the algorithm always finds an optimal control transport ramp with fidelity 99.9999 %. The quantum speed limit shows a square root dependency on the trap depth and follows closely a classical description of the problem. A deeper analysis of this fundamental limit follows in chapter 8.1.

Figure 7.3(b) shows exemplarily the solution for different Fourier components for the trap depth of $k_B \cdot 25 \mu\text{K}$. It verifies the expectation of the point symmetry of the phase ramp, since only even Fourier components lead to an improvement of the transport fidelity. For large transport times the first even Fourier component is already sufficient to improve almost perfectly the linear transport with zero Fourier components. However, close to the quantum speed limit higher orders are necessary. For the measurements shown in this work, I optimize 10 Fourier components for the amplitude and phase modulation.

Figure 7.4 shows a deeper analysis of an optimal control ramp at a trap depth of $k_B \cdot 25 \mu\text{K}$ and a transport time of $20 \mu\text{s}$ close to the quantum speed limit. An atom initialized in the ground state is highly excited during the transport up to the highest bound state as the state occupation probability for the different bound states in the lattice shows. At the end of the ramp, the state evolves from high

excited states back down into the ground state.

Experimental realization of optimal control transport ramp

The optimal control solution from the numerical calculation has to be implemented in the physical setup as real phase and amplitude profiles. In order to realize these driving ramps, we use the phase and amplitude control systems.

An optimal control solution for atom transport over one lattice site in $12.3\,\mu\text{s}$ is shown in Fig. 7.5. The transport ramps are in the time range of a few tens of microseconds and always show a point symmetry for the phase, and axial symmetry for the amplitude as expected from the proof in appendix A.3. Bandwidth limitations as well as nonlinearities of the phase and intensity control become relevant. In order to get the optimal control solution as the output signal from the control systems, the ramps need to be deconvolved with the measured impulse response functions of the particular system as described in chapter 5.5. The result is loaded onto the direct digital synthesizer (DDS), which steers the AOM controlling the intensity and phase of the laser beam as shown in Fig. 7.5(a). The intensity is directly measured by an out-of-loop photodiode, while the phase is determined by a quadrature measurement. During the application of this method, the synthesized arms are set to the same intensity. The interference of the opposite circular polarization of the co-propagating laser beams results in an effective linear polarization. The angle of the linear polarization depends on the relative phase difference $\Delta\varphi(t) = \varphi^{\sigma^+}(t) - \varphi^{\sigma^-}(t)$. The beams are guided through a polarizing beam splitter. An out-of-loop photodiode measures the intensity proportional to $\sin^2(\Delta\varphi(t)/2)$ according to Malus's law. In a second measurement, one synthesized arm is shifted by a phase of $\pi/4$ and the photodiode measures a signal proportional to $\sin^2(\Delta\varphi(t)/2 + \pi/4)$. With these two quadrature components, the relative phase between the synthesized arms is determined as follows:

$$\begin{aligned}\varphi^{\sigma^+}(t) - \varphi^{\sigma^-}(t) &= \arctan\left(\frac{\sin(\Delta\varphi(t))}{\cos(\Delta\varphi(t))}\right) \quad , \\ \cos(\Delta\varphi(t)) &= 1 - 2\sin^2\left(\frac{\Delta\varphi(t)}{2}\right) \quad , \\ \sin(\Delta\varphi(t)) &= 2\cos^2\left(\frac{\Delta\varphi(t)}{2}\right) - 1 \quad , \\ &= 2\sin^2\left(\frac{\Delta\varphi(t)}{2} + \frac{\pi}{4}\right) - 1 \quad .\end{aligned}\tag{7.14}$$

In order to further improve the phase and amplitude ramp, an iterative optical feedback is applied to compensate nonlinearities of the control system. The lim-

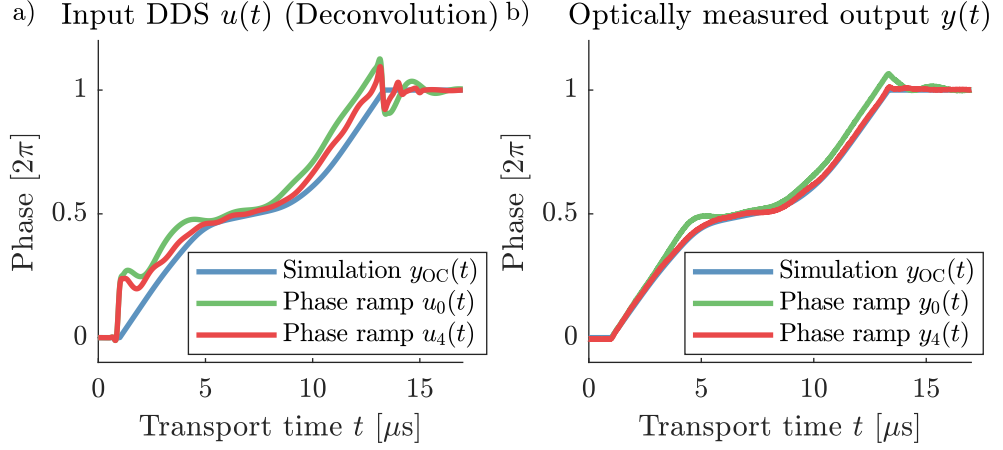


Figure 7.5: Phase measurement of an optimal control solution: (a) The blue phase ramp shows the optimal control solution from the simulation for a transport duration of $12.3 \mu\text{s}$. The green input signal of the DDS is the deconvolution of the ramp with the measured impulse response of the particular control system which compensates for bandwidth limitations. An iterative optical feedback method also compensates for nonlinearities of the control system and results in the red input signal. (b) The quadrature measurement technique measures optically the phase ramp of the lattice. In this example four iterations are sufficient for a scaling factor of $\alpha = 0.5$. The red and blue curve almost perfectly overlap. Quantitatively the coefficient of determination improves from $R^2 = 0.9916$ to $R^2 = 0.9997$.

ited bandwidth is increased by overdriving the control system. A feedback procedure measures the difference between the optical output $y_i(t)$ and the expectation $y_{OC}(t)$. The difference is resized with a scaling factor $\alpha \in (0, 1)$ and added to the previous ramp. After a deconvolution as described in eq. (5.13), the new input ramp $u_{i+1}(t)$ is determined by:

$$\begin{aligned} U_{i+1}(s) &= \frac{\mathcal{F}[y_i(t) + \alpha(y_i(t) - y_{OC}(t))]}{\mathcal{F}[g(t)]} \quad , \\ u_{i+1}(t) &= \mathcal{F}^{-1}[U_{i+1}(s)] \quad , \\ y_{i+1}(t) &= (u_{i+1} * g)(t) \quad . \end{aligned} \tag{7.15}$$

The coefficient of determination R^2 quantifies the goodness of the observed and expected driving ramp:

$$R^2 = \frac{1 - \sum [y_i(t) - y_{OC}(t)]^2}{\sum [y_i(t) - \overline{y_i(t)}]^2} \quad . \tag{7.16}$$

The result of the iterative feedback of four repetitions is shown in Fig. 7.5 and demonstrates a remarkable good reproduction of the optimal control ramp. The

ramps used for measurements in this chapter are not improved by the iterative feedback method and still show slight imperfections. This leads to a slight different transport fidelity. In order to compare the measured transport fidelity to the derived model, we measure all ramps optically by a quadrature measurement. The iterative feedback method is applied in combination with an improved measurement technique of the transport fidelity described in chapter 8.

Limitations of the optimal control ramps and outlook

The main limitation is the bandwidth of the control system, which constraints the maximum slope of the driving ramp to $0.838 \text{ rad}/\mu\text{s}$. After the AOM the wave front of the lattice beams can be distorted. The distortion can change during a phase ramp driving the AOM. The change in coupling efficiency of the laser light into the fibers due to the different distortions leads to a change in trap depth. It has to be compensated by the intensity lock and will be further improved by the high bandwidth lock system. Further noise sources are beam pointing instabilities, which result in a change of the trap depth. Off-resonant scattering of the dipole trap laser photons heats up the atoms and results in a reduced measured fidelity.

A new digital lock system provided by Signadyne (M3300A PXIe AWG and Digitizer Combination) should soon replace the analog feedback system. In combination with a feed forward technique recently derived in the work of Werninghaus [118], the bandwidth limit can be improved by one order of magnitude.

7.5 Measurement of optimal control transport

The implemented optimal control ramps are used to transport atoms over one lattice site. The measurement of the transport fidelity is performed for a constant trap depth of $k_B \cdot 80.9 \mu\text{K}$ for the $|\uparrow\rangle$ - and $|\downarrow\rangle$ -state.

An example of an optimized phase and amplitude ramp is shown in Fig. 7.6 for $14 \mu\text{s}$. In order to perform the same transport ramp for both spin states, the ramps of the σ^+ -pol. lattice are identical to the simulated ramps, while for the $|\downarrow\rangle$ -state, the dipole trap crosstalk is compensated with the σ^- -pol. lattice. Further details on the compensation method can be found in chapter 5 and appendix A.1.1. The ramps are deconvoluted with the measured impulse responses of the phase and amplitude control systems and loaded onto the DDS. The DDS steers the AOMs, which manipulates each individual lattice. In this first approach, the ramps are not further improved by the iterative feedback method. The optimal control solutions show the expected improvement in transport fidelity and robustness for various transport duration in comparison to the linear transport.

Figure 7.7 and 7.8 show the result for the $|\uparrow\rangle$ - and $|\downarrow\rangle$ -state, respectively. Each

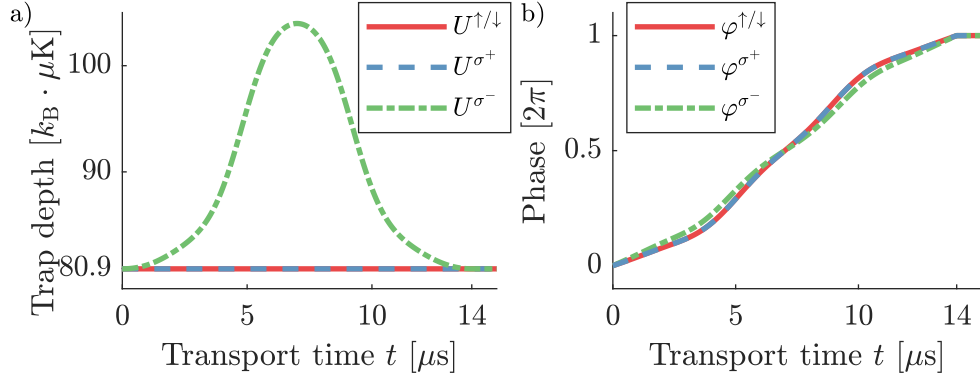


Figure 7.6: Comparison of an optimal control solution for the $|\uparrow\rangle$ - and $|\downarrow\rangle$ -state optimized for a transport duration of $14 \mu\text{s}$: (a) amplitude ramp and (b) phase ramp. The optimal control solution is an optimization of the phase ramp with constant trap depth (red). The ramps of the σ^+ -pol. lattice are identical to the simulated ramps. In order to realize the same optimal control solution for the $|\downarrow\rangle$ -state, the dipole trap crosstalk is compensated with the σ^- -pol. lattice (green).

figure shows a comparison of an optimal control transport, with a nearly constant high fidelity, an elongated single optimal control ramp with a maximal fidelity near the optimized transport time and a linear transport (blue). The transport fidelities are determined experimentally as described for the linear transport in chapter 7.3. The theoretical model of the transport fidelity (red) described in chapter 7.2 is fitted to the measurement of the linear transport, which determines a slightly higher trap depth of $U^{\uparrow} = k_B \cdot (85.7 \pm 1.2) \mu\text{K}$ and $U^{\downarrow} = k_B \cdot (86.7 \pm 1.2) \mu\text{K}$ than expected, since the model takes into account the anharmonicity of the trapping potential and a radial temperature $T_{\text{rad},\uparrow} = (8.0 \pm 1.6) \mu\text{K}$ and $T_{\text{rad},\downarrow} = (7.6 \pm 1.6) \mu\text{K}$. The models in Figure 7.7(a),(b) and 7.8(a)-(c) uses the determined trap depth and radial temperature from the linear transport. Therefore, the models are calculated without free parameters and describe all the measurement data remarkably well. If available, the simulation uses the optically measured ramps to consider imperfections in their reproduction, which become significant near the bandwidth limitation of the phase and intensity control system. This is observed in Fig. 7.7(a) and 7.8(a) for transport durations below $15 \mu\text{s}$ as a decrease in transport fidelity. With this new transport scheme, it is now possible to reduce the transport time while maintaining a high fidelity. For both spin states, I choose one optimal control solution at $T = 12 \mu\text{s}$ or $T = 14 \mu\text{s}$. If the ramp is elongated over different transport times, as shown in Fig. 7.7 (b) and 7.8 (b), the transport fidelity remains high for several transport durations. This plateau is significantly larger than for linear transport ramps. This shows, that the optimal control solutions have a better robustness against experimental imperfections than the linear transport

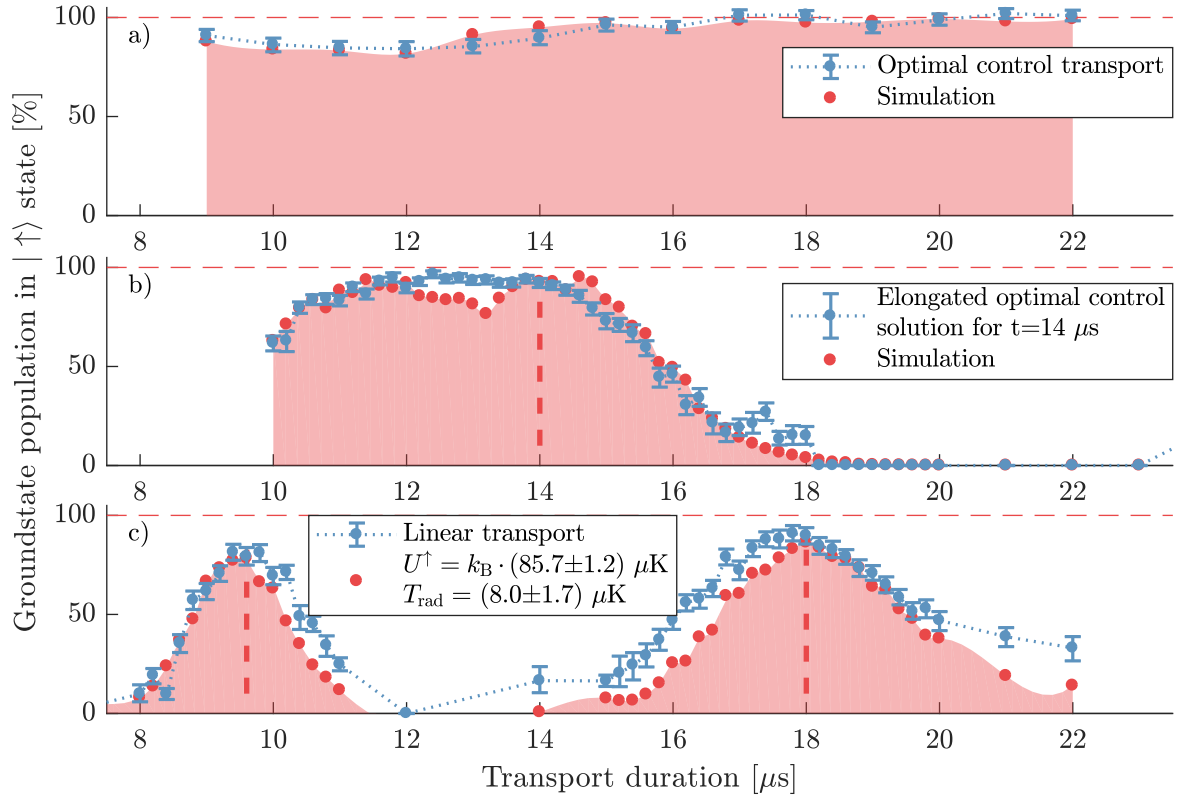


Figure 7.7: Measurement of optimal control transport of the $|\uparrow\rangle$ -state for a trap depth of $k_B \cdot 85.7 \mu\text{K}$: (a) Optimal control transport for different transport durations is compared with (b) a single optimal control solution optimized for $14 \mu\text{s}$, which is elongated for different transport durations and (c) linear transport. Optimal control transport shows a significant improvement of the transport fidelities compared to the linear transport. The optimal control solutions are optimized for a trap depth of $k_B \cdot 80.9 \mu\text{K}$. For lower transport durations the fidelity decreases below 100 % due to an underestimation of the trap depth, imperfections of the reproduced transport ramps and a finite radial temperature, which is confirmed by the numerical calculation. The simulation uses the fit result of the trap depth and radial temperature from the linear transport. (b) demonstrates a higher robustness of the optimal control solution against experimental imperfections indicated by a broad plateau.

ramps. Since the optimal control algorithm only optimizes on the transport fidelity, it can happen that the plateau is asymmetric around the optimized transport time. In Fig. 7.8 (c) I did not compensate the dipole trap cross talk for the $|\downarrow\rangle$ -state. As a consequence, the transport fidelity reduces considerably.

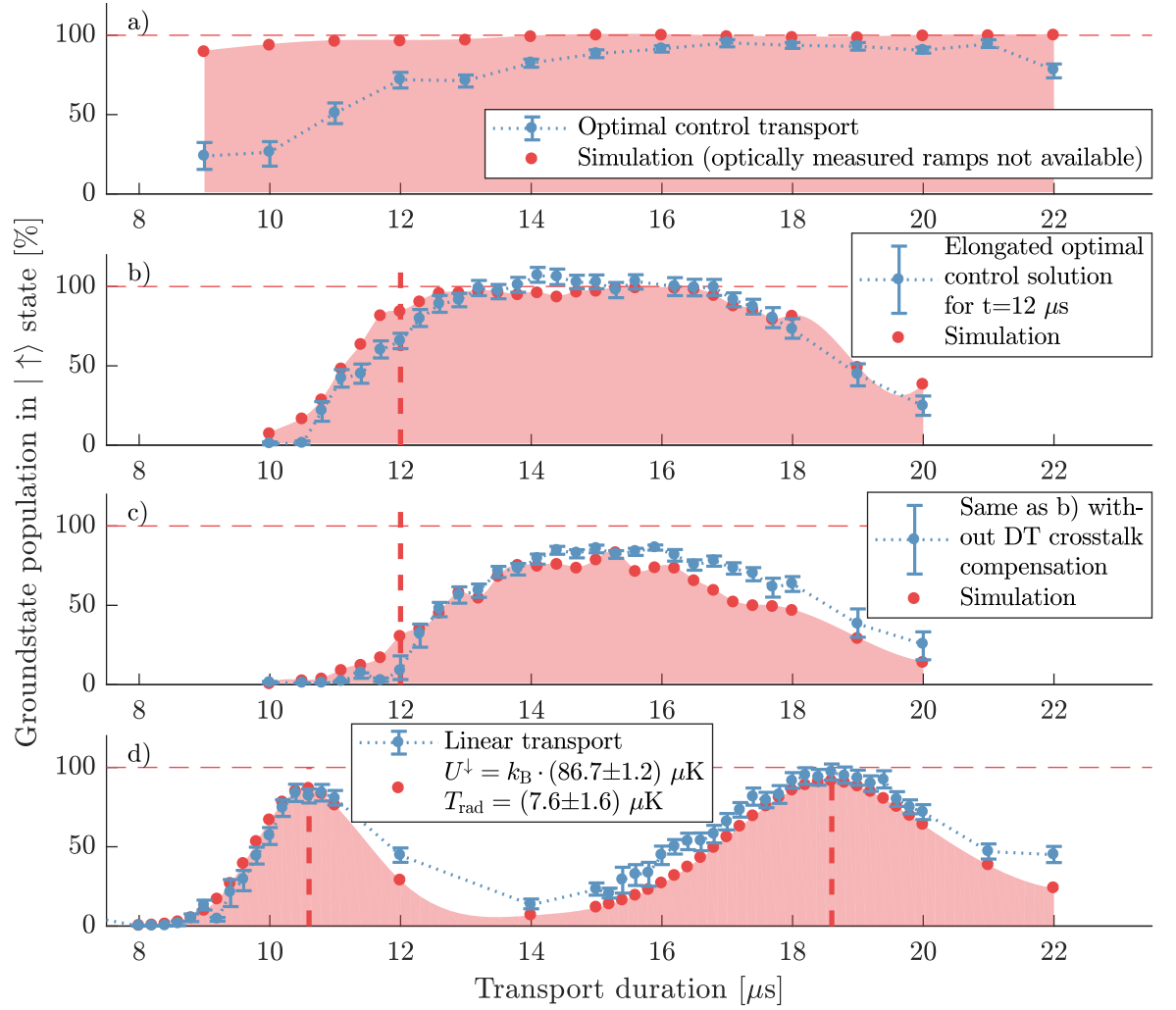


Figure 7.8: Measurement of optimal control transport of the $|\uparrow\rangle$ -state for a trap depth of $k_B \cdot 86.7 \mu\text{K}$: (a) Optimal control transport for different transport durations is compared with a single optimal control solution optimized for $12 \mu\text{s}$, which is elongated for different transport durations (b) with and (c) without dipole trap crosstalk compensation. (d) shows a linear transport. As for the $|\uparrow\rangle$ -state optimal control transport shows a significant improvement of the transport fidelities and robustness compared to the linear transport. The optimal control solutions are optimized for a trap depth of $k_B \cdot 80.9 \mu\text{K}$. The simulation in (a) deviates from the measurement since the optically measured ramps with deviations from the ideal ramps are not available, and therefore can not be used in the theoretical model. The deviations increases significantly for ramps below $15 \mu\text{s}$ near the bandwidth limit of the control loops. (b) exhibits a significantly higher transport fidelity compared to (c), which shows the importance to compensate for the dipole trap crosstalk for the $|\downarrow\rangle$ -state.

The measurement of optimal control transport shows a remarkable improvement compared to the previous transport scheme with linear ramps. The new transport scheme overcomes the restriction to choose a certain transport time and has a higher transport fidelity and robustness against experimental imperfections. In addition, we can compensate the dipole trap crosstalk, which allows coherent transport for both spin states simultaneously.

Conclusion

Applications of the state-selective transport employing quantum interference of atomic wave functions gain a factor of two in transport times compared to previous experiments. The probability to excite the vibrational state is reduced from 3 % for linear transport [57] to 1 % for optimal control transport. Additionally optimal control solutions show a higher robustness against experimental imperfections. The measurement shows a high sensitivity of the trap depth and the radial finite temperature. Therefore, the two parameters can be determined with high precision by a fit of the model. The new transport scheme allows a free choice of the transport duration, which is only limited by the quantum speed limit. If the dipole trap cross talk is compensated, the optimal control solutions are applicable for both spin states equally.

One of the key applications of this setup is the transport over distances of several lattices sites. In many cases, the transport is not realized in one step, but in multiple steps with state manipulation operation between transport steps. The dynamics of multiple transport steps is analyzed in the next chapter.

7.6 Multiple step optimal control transport

With the successful implementation of optimal control transport over one lattice site, I extend the sequence to a transport over multiple lattice sites. Here, it is interesting to investigate the robustness of successive transport steps.

The novel, fast optimal control transport can significantly reduce the effects by decoherence, which turns for example the quantum walk into a classical random walk. That is why I investigate the successive repetition of an optimal control solution optimized for a transport duration of $12\ \mu\text{s}$. The delay time between shift operations of $5\ \mu\text{s}$. This corresponds to the time of a microwave $\pi/2$ -pulse, which can be used in quantum walk experiments as a coin operation.

To investigate the robustness of successive transport steps, I measure the transport fidelity and the atom survival in dependence of the number of transport steps. The result is shown in Fig. 7.9(a). While the single step transport sequence exhibits a high transport fidelity, the excitations for multiple step transport add up

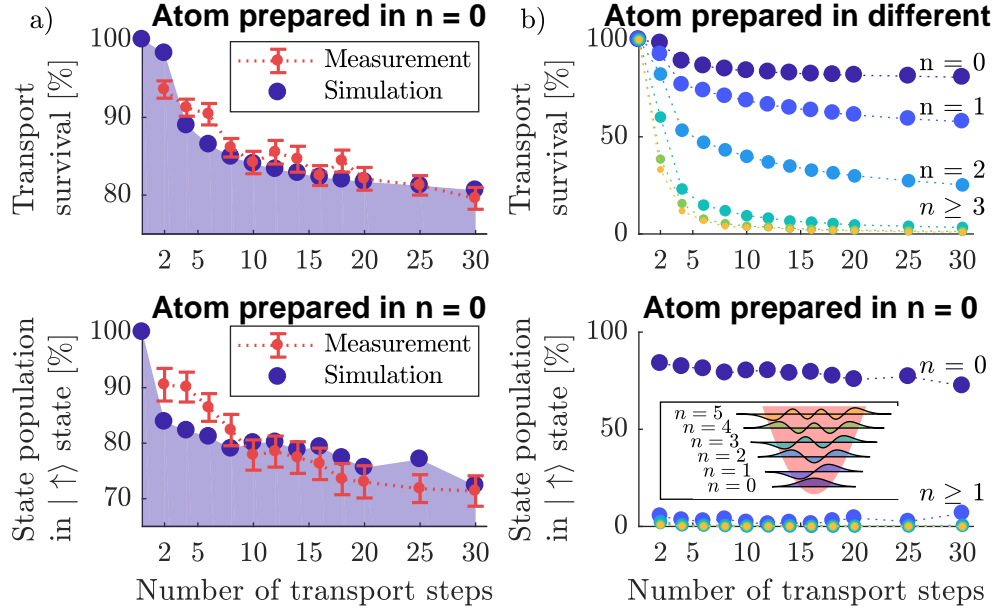


Figure 7.9: Dynamics for multiple successive transport steps with a delay time of $5 \mu\text{s}$. A single transport step is an optimal control solution that is optimized for a transport duration of for $12 \mu\text{s}$: (a) For atoms prepared in the ground state, the transport survival as well as the ground state population reduces with increasing number of transport steps. The simulation for a trap depth of $U^\uparrow = k_B \cdot 83.5 \mu\text{K}$ and a radial temperature of $T_{\text{rad}} = 8 \mu\text{K}$ confirms that a nearly constant fraction of the atoms remains in the ground state for increasing number of steps. (b) Additionally to (a), the simulation shows the dynamics also in higher excited states, which are color-coded according to the inset. The population in higher excited states is almost negligible. It follows that the ground state population is mostly protected during the transport. However, if an atom gets excited, it is quickly lost from the trap, which explains the observed high atom loss.

and lead to a significant loss of atoms from the trap. The atom loss rate of the transport fidelity and the groundstate occupation decreases with increasing number of transport steps. Although atoms get lost from the trap, a significant fraction of above 75% of the remaining atoms stays in the ground state. The atoms in the ground state still show a significant robustness against heating during transport. For the simulation of the transport fidelity and survival, I choose an empirical estimate for the trap depth of $U^\uparrow = k_B \cdot 83.5 \mu\text{K}$ and a radial temperature of $T_{\text{rad}} = 8 \mu\text{K}$. The model is in good agreement with the experimental data. This model is not fitted, because a numerical calculation of up to 30 transport steps is too computationally demanding as the dimensions of the underlying Hilbert space grow exponentially with the size of the quantum system.

The simulation in Fig. 7.9 (b) demonstrates that an atom initialized in an excited state is quickly lost from the trap. For atom interference experiments, excited atoms reduce the contrast, since orthogonal modes of the wavefunction can not interfere. Therefore, the loss of excited atoms is an advantage. It further shows that the population in higher excited states is almost negligible. It follows that the ground state population is mostly protected during the transport. However, if an atom gets excited, it is quickly lost from the trap, which explains the observed high atom loss. In the next chapter, I show how the atom survival and the ground state occupation can be improved for certain time delays between the transport steps.

Robustness of multiple step transport

The atom survival is a good indicator of the preservation of the ground state, since the excited atoms get quickly lost. In the following measurement shown in Fig. 7.10, the optimal control ramp for $12\mu\text{s}$ optimized for a trap depth of $U^\dagger = k_B \cdot 80.9\mu\text{K}$ is used for 20 transport steps. The survival for different delay times between the transport steps shows a periodic behavior. The oscillation is also reproduced by the theoretical model and coincides with the atomic oscillation period in the trap $2\pi/\Omega_{\text{trap}}$. The previous measurements indicate the presence of a superposition state of the ground state and higher excited states. The distinctive shape of the oscillation of this measurement confirms this result and even indicates the coupling of the ground state with the lowest excited states. A localized time-dependent atomic wavefunction potential is described in the basis of the bounded eigenfunctions with an amplitude c_n and a phase ϕ_n :

$$|\psi(y, t)\rangle = \sum_{n=0}^{n_{\text{bound}}} e^{-i(E_n t/\hbar + \phi_n)} c_n |n\rangle \quad . \quad (7.17)$$

The acceleration of the atoms is continuously changed during the optimal control transport and the position operator $\hat{\mathbf{y}}(t)$ is therefore time-dependent. During a linear transport, the sudden shift at the beginning of the transport creates a coherent state and the expectation value of the position operator oscillates only with the trap frequency. However, in case of optimal control transport, it is necessary to assume a coupling with higher order excited states. The expectation value of the position operator is then described by

$$\begin{aligned} \langle \hat{\mathbf{y}}(t) \rangle &= \langle \psi(y, t) | \hat{\mathbf{y}}(t) | \psi(y, t) \rangle \\ &= \sum_{n=0}^{n_{\text{bound}}} \sum_{m=0}^{n_{\text{bound}}-n} e^{-i((E_{n+m}-E_n)t/\hbar + \phi_{nm})} c_{nm} + e^{i((E_{n+m}-E_n)t/\hbar + \phi_{nm})} c'_{nm} \quad . \end{aligned} \quad (7.18)$$

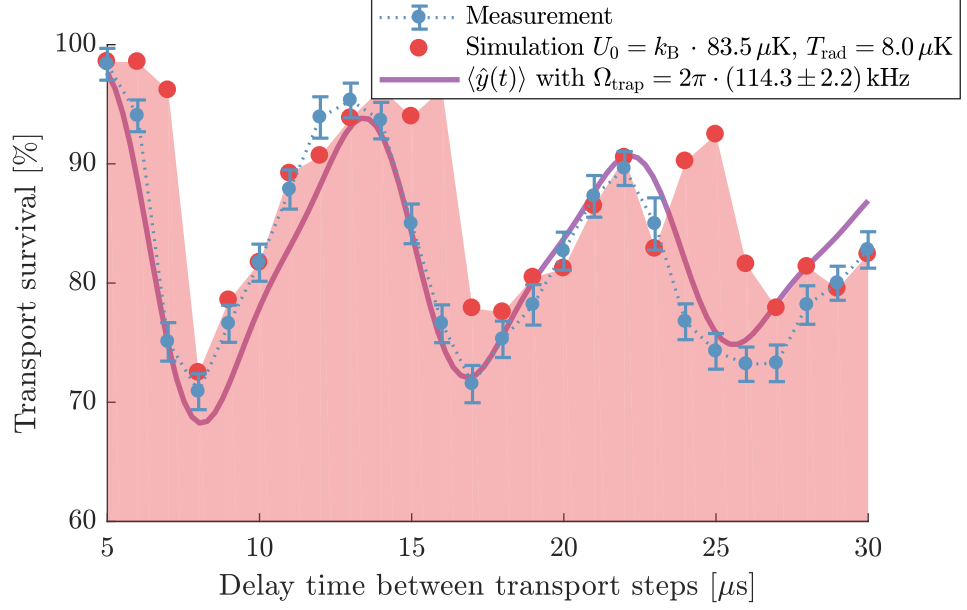


Figure 7.10: Measurement of the transport survival of the $|\uparrow\rangle$ -state depending on the delay time between 20 successive transport step: An optimal control transport ramp of $12 \mu\text{s}$ duration is chosen. At multiples of the harmonic oscillator period of the trap, high survival is observed, which is confirmed by a numerical calculation for a trap depth of $U^\uparrow = k_B \cdot 83.5 \mu\text{K}$ and a radial temperature of $T_{\text{rad}} = 8 \mu\text{K}$. The asymmetric shape of the oscillation indicates a coupling of the ground state with the lowest excited states. As a consequence, the state oscillates with harmonics of the trap frequency, which is confirmed with a fit of the expectation value of the position operator.

The expectation value oscillates also with higher multiples of the trap frequency $n\Omega_{\text{trap}}$. For simplicity I assume a harmonic potential $E_n = n\hbar\Omega_{\text{trap}}$. The coupling is dominated by the interaction between the ground state and the lowest excited states:

$$\begin{aligned} \langle \hat{\mathbf{y}}(t) \rangle &= \sum_{n=0}^{n_{\text{bound}}} \cos(n\Omega_{\text{trap}}t + \phi_n) c_n \\ S &= \sum_{n=0}^{n_{\text{bound}}} c_n^2 \quad . \end{aligned} \tag{7.19}$$

The atom survival $S = (82.1 \pm 1.4)\%$ and the ground state population $c_0^2 = (73.0 \pm 2.9)\%$ after 20 transport steps is determined from the measurement in Fig. 7.9. A fit of the model $\langle \hat{\mathbf{y}}(t) \rangle$ determines an occupation of $8.7_{-2.7}^{+3.2}\%$ in the first and $0.4_{-0.3}^{+0.9}\%$ in the second excited state, which agrees well with the simulation shown in Fig. 7.9. The fit is shown in Fig. 7.10.

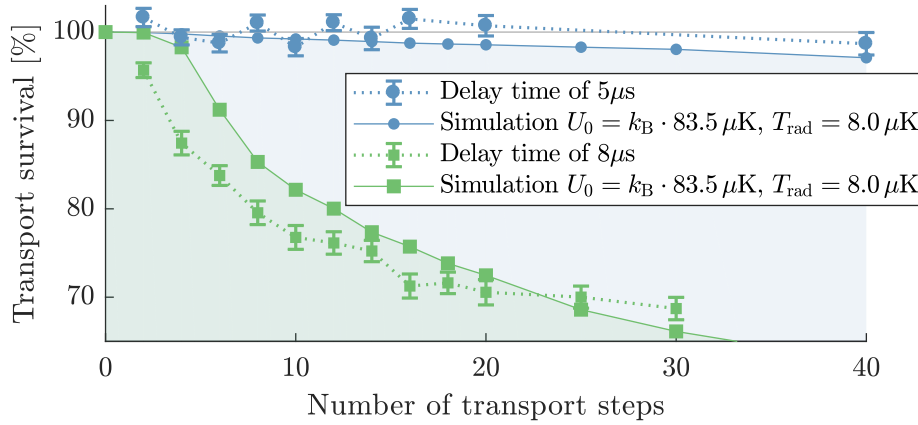


Figure 7.11: Measurement of the robustness of successive optimal control transport sequences for the outstanding delay times of $5 \mu\text{s}$ and $8 \mu\text{s}$ in Fig. 7.10. The delay of $5 \mu\text{s}$ shows a high robustness against experimental imperfection with an atom loss below 2 %. However, the delay of $8 \mu\text{s}$ shows a high atom loss for multiple transport steps. The numerical calculation for a trap depth of $U^\dagger = k_B \cdot 83.5 \mu\text{K}$ and a radial temperature of $T_{\text{rad}} = 8 \mu\text{K}$ is in good agreement with the experimental data.

Applications with multiple transport steps with robust delay times ensure low atom losses and preservation of the ground state occupation. Figure 7.11 shows a comparison of the dependency between transport survival and the number of transport steps for two delay times of $5 \mu\text{s}$ and $8 \mu\text{s}$. Those times were chosen for showing optimal atom survival and highest atom loss. Even after 40 transport steps, an atom loss below 2 % is observed for the optimal delay time. For the delay time of $8 \mu\text{s}$, it can be observed how the atom loss adds up with increasing number of transport steps.

To avoid the dependency on specific delay times, one could use optimal control theory to optimize the driving ramp for a desired delay time. However, I noticed that the computational capacities for the optimization are already limited for large distances of a few tens of lattice sites. Another approach is live optimal control, when the experimental measurement time becomes shorter than the time needed for the numerical calculation. This is discussed in the next chapter.

7.7 Live optimal control

Numeric simulation can show discrepancies to the real experiment due to inaccurate assumptions or insufficient knowledge of the system parameters. Earlier

optimal control experiments have demonstrated to improve the result further by replacing the cost function model by the experiment itself [119]. In a closed loop, the experiment delivers the fidelity by a direct measurement during the optimization of the control parameters. This live optimal control approach is also advantageous for systems that are computationally demanding, such as the considered transport problem of long distance optimization. For future applications, a transport of atoms over hundreds of lattice sites is considered. The number of iterations stays the same for simulation and experiment, while the evaluation time of a single fidelity estimation is different. An experimental run takes roughly the same time while the simulation time increases with the Hilbert space and exceeds the measurement time.

Optimization algorithm

The optimization algorithm is performed exemplary for the $|\uparrow\rangle$ -state by optimizing two Fourier components of the phase ramp

$$\begin{aligned} U^\uparrow(t, T) &= k_B \cdot 80 \mu\text{K} = \text{const} \\ \varphi^\uparrow(t, T) &= \frac{2\pi}{T}t + \sum_{m=0}^2 b_m \sin(\nu_m t), \quad t \in [0, T] \quad . \end{aligned} \quad (7.20)$$

In order to determine the cost function with the experiment, the measurement error has to be considered carefully. Each measurement is averaged with a minimum number of 15 repetitions and the measurement continues until a measurement error below 1 % is reached. A single measurement is an average of about ten atoms. Furthermore, the cost function is determined by several quantities that are measured one after the other. To reduce the measurement time, I redefine the cost function to use a minimum number of measurement quantities: I minimize the cooling sideband height $CSB_{\text{transport}}$ under the condition that the atom survival $S_{\text{transport}}$ is above the empirical value of 88 %. This condition is necessary, because the cooling sideband height scales with the survival and is also minimized for a low-fidelity transport with high atom loss. In a first approach, the cost function is defined as follows:

$$C = \begin{cases} 1 & S_{\text{transport}} < 0.88 \\ 2(S_0 - S_{\text{transport}}) + (CSB_{\text{transport}} - CSB_0) & S_{\text{transport}} \geq 0.88 \end{cases} \quad . \quad (7.21)$$

S_0 and CSB_0 describe the atom survival and cooling sideband height without transport. The survival is empirically weighted stronger by a factor of two because it is a necessary condition for a high-fidelity transport. The live optimal control is tested for a transport duration of $12 \mu\text{s}$ starting with a linear ramp as the initial

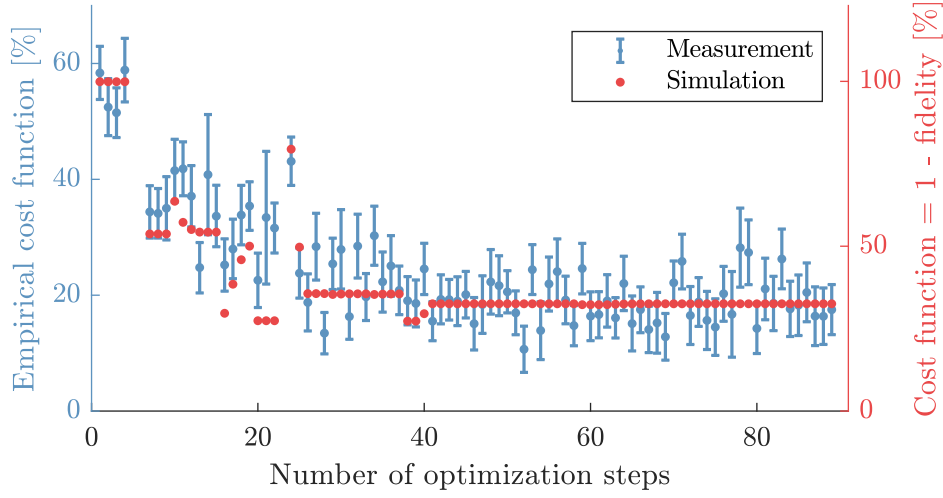


Figure 7.12: Measurement of a transport ramp optimization with live feedback from the experiment: A transport ramp over one lattice site with a duration of $12\ \mu\text{s}$ is optimized. The optimization parameter are two Fourier components. The empirical cost function is a weighted sum of a survival and cooling sideband height measurement (blue). The initial guess is a linear transport ramp. The empirical cost is optimized in 90 optimization steps. The transport fidelity is calculated with the derived model for the ramps of each optimization steps. The cost function is defined as the infidelity (red). In agreement with the simulation, the algorithm determines an optimal control solution with the same infidelity of 32 %.

guess. The demonstration of live optimal control of a transport over one lattice site is shown in Fig. 7.12. Each data point corresponds to a ramp with two Fourier components, which are optimized in this measurement. A linear ramp of $12\ \mu\text{s}$ has an empirical cost of 58 %. The cost function converges in 90 optimization steps to 17 % (blue). The transport fidelity is calculated with the derived model for the ramps of each optimization steps. The cost function is defined as the infidelity and shown in red. In agreement with this model, the algorithm is able to optimize both Fourier components reaching a minimum transport infidelity of 32 %. The same minimum cost is obtained, when the ramps are optimized with the numerical optimization algorithm. This measurement demonstrates, that live optimal can be used as an alternative optimization technique.

7.8 Conclusion

In this chapter, I introduced a numeric approach for atom transport based on optimal control. A decomposition of the evolution operator allows a computationally fast simulation of the atomic motion and the tracing of the time evolution of a pre-defined initial state. The overlap with a target state defines the transport fidelity, which is confirmed experimentally. Furthermore, I demonstrated how optimal control theory can improve atom transport with respect to high fidelities above 99 %, to larger robustness against experimental imperfections and to a factor of two shorter transport durations as in previous experiments with linear transport ramps. The ability to choose an arbitrary transport duration above a fundamental lower bound, the so-called quantum speed limit, and the possibility to incorporate imperfections resulting from the lattice crosstalk, high transport fidelities are reached simultaneously for both spin states. With regard to future quantum walk experiments, I analyzed the dynamics for multiple successive transport sequences. A key finding here is, that optimal control ramps efficiently protect the ground state population while excited atoms are quickly lost from the trap. In addition, I observe interference effects between the ground state and higher excited states, which lead to a transport efficiency that depends on the delay time between transport steps. For certain delay times, high atom survival of above 98 % is possible while maintaining the ground state population for up to 40 transport steps. In a proof-of-principle measurement, I show that a measurement based on the live feedback algorithm is an alternative to find optimal control transport ramps. The advantage of this method is, that knowledge of the system parameters is not required. It may be used in the future for long distance transport optimization, where the numerical simulation fails due to unfeasible calculation times.

CHAPTER 8

THE QUANTUM SPEED LIMIT

In the last century, many research efforts were inspired by the question how to interpret the Heisenberg's time-energy uncertainty relation [120]. The interpretation of this particular relation is challenging due to the fact that time is no observable. In 1945, Mandelstam and Tamm postulated for the first time, that the principle is not a statement about simultaneous events as for the position-momentum uncertainty relation, but rather defines a lower boundary for the time a quantum system needs to evolve from one state into an orthogonal state [121]. Based on this interpretation, they derived the first expression for the quantum speed limit in an isolated system. The quantum speed limit describes a maximum rate, but in general the name is also used to describe the minimum time. The finite energy of each system leads to a minimum evolution time. From then on, this concept has been extended to different regimes. In quantum information, the limit is interpreted as the maximum rate, in which quantum information can be processed and communicated [122, 123]. As a consequence, a quantum computer can only execute a limited number of operations in a given time. This limit only depends on the energy and not on the computer architecture. A parallelization of computer processes can not overcome this fundamental limit, but help to achieve the fastest computational speed. The bound definition by Mandelstam and Tamm focuses on free-evolving systems, with the initial state evolving into an arbitrary orthogonal one.

With regard to the relevant influence of the environment, for example by dephasing, thermalization or dissipation in real-life applications, the quantum speed limit has been generalized to open systems [124–126]. However, many practical applications are performed with external driving to reach a specific orthogonal state. Therefore, a new derivation of the quantum speed limit is needed [127–129]. Such driven systems exhibit a non-equilibrium behavior as a result of the interaction of the system with an external time-dependent field. Recent applications of optimal control at the quantum speed limit have been successfully demonstrated for two different driven quantum-mechanical systems [130]: The goal of the first experiment is the coherent transfer of a Rb⁸⁷ BEC on an atom chip from the vibra-

tional ground state into the first excited state by displacing the trapping potential. With the CRAB algorithm, they derive an optimal driving ramp for the shortest possible time while maintaining a high transfer efficiency. The second experiment drives a BEC non-adiabatically from the superfluid phase to the Mott-insulating phase in the shortest possible time using the same algorithm.

In the first part of this chapter, I demonstrate the quantum speed limit for atom transport. In a second part, I introduce an improved measurement technique to detect the transport fidelity with higher precision and analyze the dynamics at the quantum speed limit for different trap depths. Finally, I propose a measurement scheme to explore the quantum speed limit of a free-evolving system.

8.1 Quantum speed limit of atom transport

In this chapter, I demonstrate the finite-temperature quantum speed limit in transporting an atom from one position to another in space while preserving the ground state occupation. High-speed operations in these quantum systems build a key element in quantum information processing and quantum computation. The ion-trap quantum computer [131] has demonstrated the elementary requirements for quantum computation in terms of generation of entangled states [132] and error correction [133]. Shuttling ions between different trapping zones without heating takes time in the microsecond regime, and is the limiting factor in fast measurement schemes [134, 135]. Entangling gates demonstrated in previous work at NIST show a reduced error when the atoms are in the quantum ground state [136, 137]. In order to avoid recooling the atoms after the shuttling, transport sequences have been demonstrated, that maintain the ground state occupation by adjusting the transport time to multiples of the oscillation period of the ions in the trap [106–108]. Similar successes of fast and precise transporting in the non-adiabatic regime without heating were achieved for neutral atom in optical tweezers [74] and magnetic quadrupole potentials [138]. In the context of quantum walks, fast atom transport boost the number of possible operation steps and increases the measurement fidelity, which is limited dominantly by the coherence time of our system.

The quantum speed limit

The quantum speed limit in our driven system defines the fundamental upper bound how fast an atom can be transported over some distance without heating. In order to extract the information about the quantum speed limit out of the

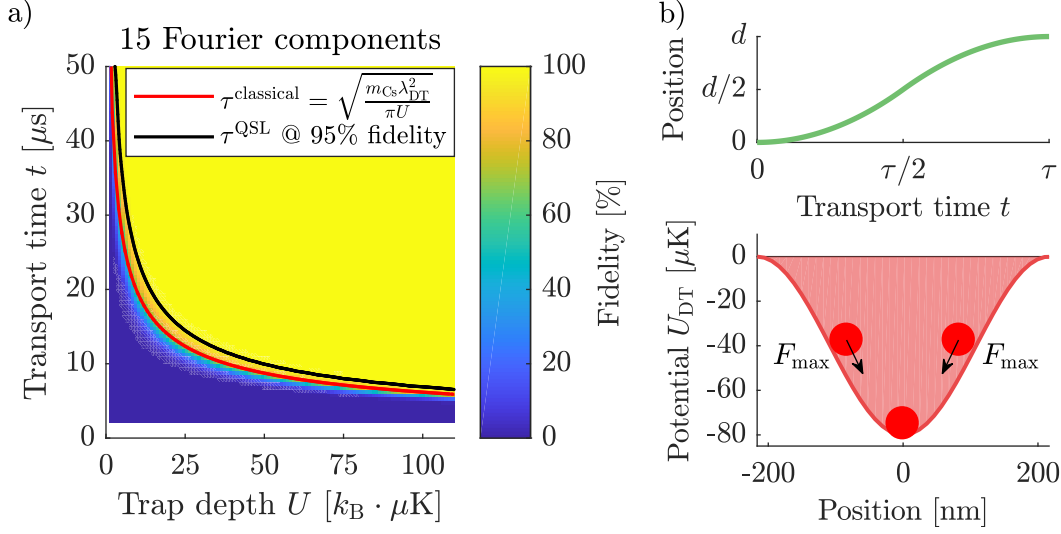


Figure 8.1: The classical and quantum speed limit: (a) The quantum speed limit as indicated by the 95 % fidelity limit (black line) of numerically calculated optimal control solutions shows a square root dependency on the trap depth similar to the classical speed limit (red line). (b) The classical driving ramp follows an s-shape, which accelerates or decelerates the atom at the steepest slope of the sinusoidal lattice potential.

numerical model and the experimental evaluation, I introduce a heuristic limit:

$$\mathcal{F}_{\text{QSL}} = |\langle \psi_{\text{target}} | \hat{U}_{\text{evo}}(\tau^{\text{QSL}}) | \psi_{\text{init}} \rangle|^2 = 0.95 \quad . \quad (8.1)$$

The limit τ^{QSL} is defined as the shortest transport time for which the fidelity does not drop below 95 %. The result of a numerical calculation is shown in Fig. 8.1(a): The color-coded transport fidelity is derived in dependency of the transport time t and the trap depth U . The solutions are optimized for a transport over one lattice site and derived with 15 optimization parameters, which corresponds to the Fourier components in eq. 7.13. The quantum speed limit (black line) shows a square-root dependency on the trap depth as it is expected also for the classical case (red line).

The classical speed limit

In the classical approach the atom experiences the largest acceleration or deceleration $\pm a_{\text{max}}$ in the sinusoidal potential at the position $kx_{\text{max}} - \varphi = \pm\pi/4$ as shown

in Fig. 8.1 (b). The absolute value of the force F_{\max} is defined as:

$$\begin{aligned} F_{\max} &= m_{\text{CS}} a_{\max} = -|\nabla U_{\text{DT}}| \Big|_{x=x_{\max}} = -kU \sin(2(kx_{\max} - \varphi)) = \pm kU \quad , \\ a_{\max} &= \pm \frac{2\pi}{m_{\text{CS}} \lambda_{\text{DT}}} U \quad . \end{aligned} \quad (8.2)$$

I assume a transport sequence in which the atom is constantly accelerated half of the transport time τ and slowed down in the same amount of time with maximum acceleration and deceleration, respectively. Therefore, the transport ramp follows an s-shaped driving ramp. The classical speed limit $\tau^{\text{classical}}$ for transport distance d is calculated by

$$\begin{aligned} \frac{d}{2} &= \frac{1}{2} a_{\max} \left(\frac{\tau^{\text{classical}}}{2} \right)^2 \\ \Rightarrow \tau^{\text{classical}} &= \sqrt{\frac{2 d m_{\text{CS}} \lambda_{\text{DT}}}{\pi U}} \quad . \end{aligned} \quad (8.3)$$

The classical speed limit is proportional to the harmonic oscillator period $\tau^{\text{harm}} = \sqrt{m_{\text{CS}} \lambda_{\text{DT}} / (2U)}$. The time of the classical speed limit is always smaller than τ^{QSL} as shown in Fig. 8.1 (a).

Measurement of the quantum speed limit

For an experimental verification of the quantum speed limit, I use a trap depth of about $k_{\text{B}} \cdot 25 \mu\text{K}$. In the limit of a deep trap, the number of maximum excitations stays way below the number of bound states and the trap is well approximated by an harmonic potential. For shallow traps, however, the atoms get excited close to the highest energetic bound states and the anharmonicity of the lattice has to be taken into account. From the numerical analysis, the quantum speed limit is expected at $15 \mu\text{s}$, which is below the bandwidth limitation of the phase and intensity control system.

In order to derive the optimal control ramps, the trap depth has to be determined. This is achieved with a measurement of a microwave sideband spectrum. A trap depth of $k_{\text{B}} \cdot 18.86 \mu\text{K}$ is determined by fitting three Gaussian curves to the carrier transition and two sidebands. This fit method is less accurate, than the newly developed temperature model and leads to an underestimation of the trap depth.

The transport fidelity of the derived optimal control ramps is measured as follows: The atoms are prepared in the motional ground state by microwave sideband cooling. Since the cooling parameters are optimized for a trap depth of $k_{\text{B}} \cdot 80 \mu\text{K}$, the preparation is done in this deeper lattice potential. Then the trap depth is lowered adiabatically to about $k_{\text{B}} \cdot 25 \mu\text{K}$ within 1 ms and the atoms are transport over

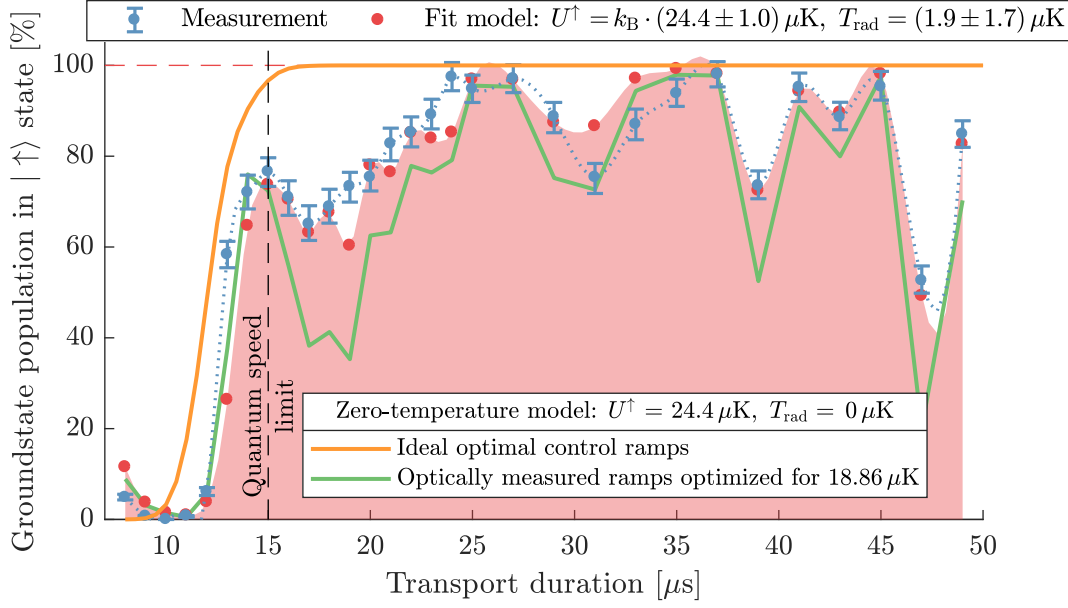


Figure 8.2: Measurement of the quantum speed limit for a measured trap depth of $k_B \cdot 18.86 \mu\text{K}$. The underestimation of the depth of $k_B \cdot 24.4 \mu\text{K}$ shifts the measured quantum speed limit to higher transport durations and leads to a partially reduced transport fidelities above the limit. For a trap depth of $k_B \cdot 24.4 \mu\text{K}$, a quantum speed limit at $15 \mu\text{s}$ is expected (orange curve). The fit model includes the optically measured driving ramps for $k_B \cdot 18.86 \mu\text{K}$ and estimates the trap depth and a radial temperature of $1.9 \mu\text{K}$ and reproduces the measurement result. In addition, a comparison of the finite- and zero-temperature model is depicted (red and green curve).

one lattice site. After the potential is adiabatically increased back to $k_B \cdot 80 \mu\text{K}$, the groundstate population is determined with a microwave sideband spectrum as described in chapter 6.3. The transport fidelity is determined by comparing the ground state population with and without transport. The result of the fidelity for different transport durations is depicted in Fig. 8.2. The measurement (blue) shows a significant and sudden increase in transport fidelity around $12 \mu\text{s}$ and reaches high fidelities up to 98%. Due to the underestimation of the trap depth, the transport ramps are not always optimal, which is observed in a decrease of the fidelity for certain transport times above the quantum speed limit. The derived temperature model described in chapter 7.3 is used to estimate the trap depth (red). A fit determines a trap depth of $k_B \cdot 24.4 \mu\text{K}$, a radial temperature of $1.9 \mu\text{K}$ and reproduces well the features in the measurement. A lower estimate of the trap depth shifts the quantum speed limit from $14 \mu\text{s}$ (orange curve) to higher transport durations as expected for shallower lattices (green and red model curve). The

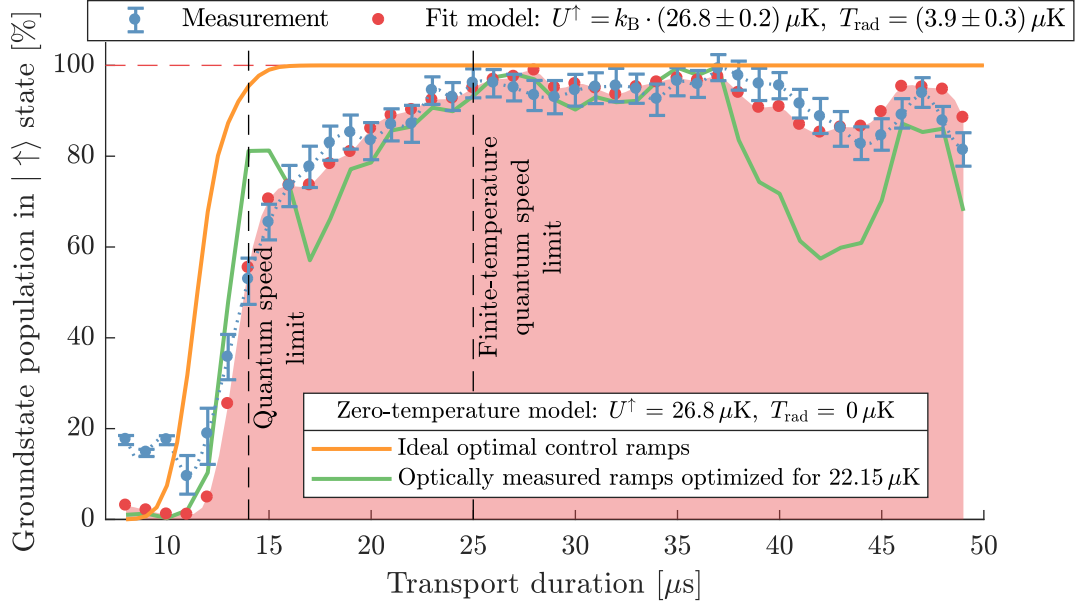


Figure 8.3: Measurement of the quantum speed limit for a measured trap depth of $k_B \cdot 22.15 \mu\text{K}$. The better estimate of the depth allows a determination of the finite-temperature quantum speed limit at $25 \mu\text{s}$, which is larger than the quantum speed limit at $14 \mu\text{s}$ for an ideal optimal control ramps for the trap depth and perfect radial ground state cooling (orange curve). In addition, a comparison of the finite- and zero-temperature model is depicted (red and green curve).

radial temperature affects the curve towards a slower rise time of the fidelity. The rise of the transport fidelity for transport durations below the quantum speed limit is an artifact of our measurement technique, where the ground state population of all lattice sites is measured. Below the quantum speed limit, the transport is so fast that the atoms can remain in the ground state of the initial trapping site and give rise to the experimentally measured fidelity.

A second measurement is shown in Fig. 8.3, where the transport ramps are optimized for a trap depth of $k_B \cdot 22.15 \mu\text{K}$. With this better estimate of the depth, the transport fidelity significantly improves and the measured quantum speed limit is determined at $25 \mu\text{s}$. This limit lies above the expected limit of $14 \mu\text{s}$. The optimization algorithm to derive the transport ramps assumes an initial state in the three-dimensional ground state. Since the atoms are not cooled in the radial direction, we define the finite-temperature quantum speed limit for thermal atoms analog to the quantum speed limit to reach 95% transport fidelity within the error bars. A higher radial temperature increases the probability, that the atom is located away from the trap center. As a consequence, the effective trap depth is on average smaller, which leads to the observed higher quantum speed limit.

The measurement results shows for the first time the transition over the quantum speed limit, where the transport fidelity suddenly decreases. The theoretical model well describes the observed measurement data and even allows a good estimate of the trap depth and the radial temperature. In the next chapter, a second measurement technique is introduced, which increases the measurement precision further.

8.2 Direct vibrational state detection scheme

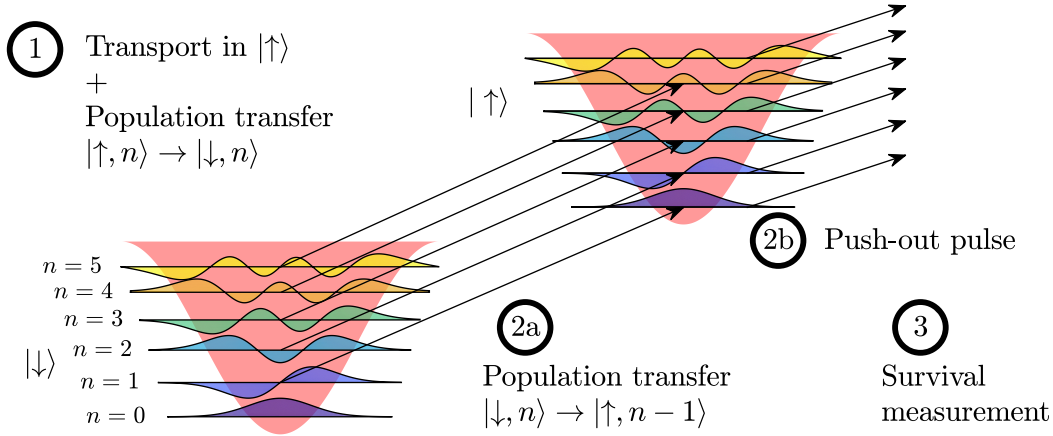


Figure 8.4: Direct, precise and robust measurement technique to determine the vibrational state population: 1) After the transport in the $|\uparrow\rangle$ -state, the atoms are transferred with a π -pulse into the $|\downarrow\rangle$ -state with 98 % efficiency. 2a)+2b) A repetition of population transfer by microwave sideband coupling, which is optimized on the $|\downarrow, n=1\rangle \leftrightarrow |\uparrow, n=0\rangle$ transition, and followed by a push-out of atoms in the $|\uparrow\rangle$ -state, removes efficiently atoms above a chosen vibrational state m (here $m=1$). 3) The remaining atoms in the $|\downarrow\rangle$ -state are detected in a survival measurement.

So far I used a measurement technique that determines the vibrational state occupation indirectly, since it is based on a model fit to sideband heights in a microwave spectrum. A more precise ground state detection scheme has been demonstrated [86], which can directly determine the ground state population. The basic idea is depicted in Fig. 8.4: Atoms are removed above a certain vibrational state and the remaining atoms are subsequently counted. First, the atoms are cooled down by microwave sideband cooling and reach a ground state occupation of $(98 \pm 1) \%$. Atoms prepared in the $|\uparrow\rangle$ -state are transferred via a carrier π -pulse transition into the $|\downarrow\rangle$ -state while preserving their vibrational state distribution. In the second

step, a microwave coupling on the $|\downarrow, n+m\rangle \leftrightarrow |\uparrow, n\rangle$ transition transfers the population with a vibrational number larger than $m-1$ into the $|\uparrow\rangle$ -state. A Gaussian transfer pulse with a duration of $90\ \mu\text{s}$ and a Gaussian width of $9\ \mu\text{s}$ is used. The coupling depends on the Franck-Condon factor and the anharmonicity of the trap for each transition, which leads to different single state transfer efficiency $f_1(n+m)$ of the vibrational states. Atoms in lower vibrational states are not coupled in this process and remain in the $|\downarrow\rangle$ -state. A subsequent push-out pulse removes all atoms in the $|\uparrow\rangle$ -state. If the sideband transfer and push-out pulse is repeated N times, the total efficiency to remove atoms above the state $|m-1\rangle$ increases exponentially according to:

$$f_N(n+m) = 1 - (1 - f_1(n+m))^N \quad . \quad (8.4)$$

In the last step, the remaining atoms are counted by fluorescence detection. The number of repetitions is a trade off between an efficient removal of atoms in the states $|m+n\rangle$ and a high survival probability of atoms in lowest vibrational states. The ground state population is reduced in each repetition step due to off-resonant state transfer. For the following measurements $m=1$ is chosen to determine the ground state population after transport.

The result is shown in Fig. 8.5 for a different number of repetitions. The measured data shows three distinctive dips. The central dip corresponds to the carrier transition and the left and right valley to the first order cooling and heating sideband, respectively. For the carrier transition, we observe a single transfer efficiency of the order of 25 %. The total efficiency to remove atoms is improved with increasing number of repetitions. For more than 10 repetitions, the population is almost completely removed and the dip evolves into a broader basin. The same effect is observed for the heating sideband since the microwave transfer pulse is optimized on the sideband transition $|\downarrow, n+m=1\rangle \leftrightarrow |\uparrow, n=0\rangle$ with a single transfer efficiency of $f_1(n+m=1) = 85\%$. However, the cooling sideband stays nearly unaffected and the survival probability reduces only by a few percent for a repetition number of $N=15$. A high repetition rate also leads to a broadening of the dip. The ground state population results directly from the cooling sideband height rescaled by the survival probability (gray line). In order to reduce the measurement time, only a measurement at the cooling sideband transition is performed. Since the position of the dips can change for different vibrational state occupation, the broadening effect of the dips is an advantage. It further reduces the sensitivity of a measurement of the maximal depth. In the following experiments, $N=10$ repetitions are chosen as a good compromise, resulting in a survival probability of 91 %. Atoms with a vibrational quantum number larger than one are removed with an efficiency of 97 %.

In the following measurements, the transport fidelity is determined by the ratio

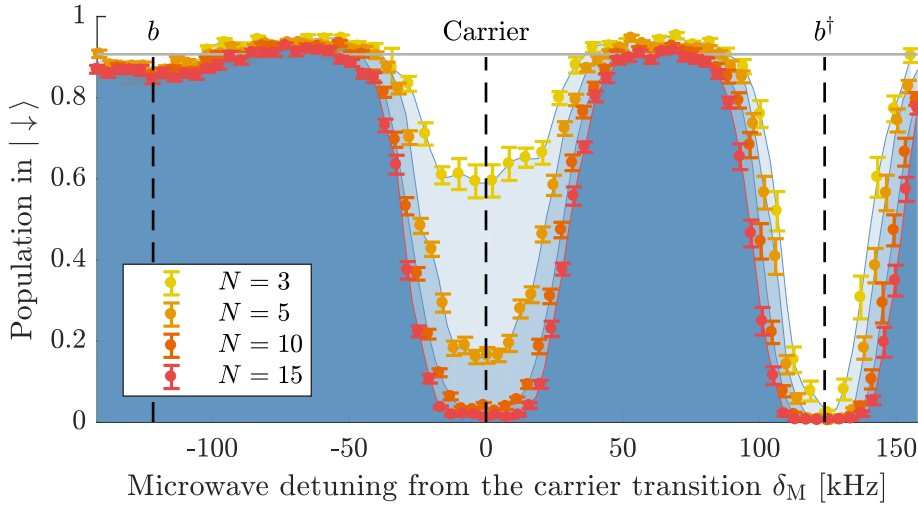


Figure 8.5: Microwave spectrum for direct measurement of the ground state population for different number of repetitions N : The blue shaded areas are added to distinguish the different data sets more easily. In this example, the population is removed in a vibrational states above $n = 0$. The population on the carrier and heating sideband (b^\dagger) transition is efficiently removed with increasing number of repetitions, while the cooling sideband (b) keeps the same height and broadens with more repetitions to a plateau. The survival probability indicated by the gray horizontal line for $N = 15$ repetitions slightly decreases for higher number of repetitions. When the population in the carrier is efficiently removed by several repetitions, the fidelity is directly extracted from the ratio of the cooling sideband height with and without transport.

of atoms in the ground state before and after transport. This corresponds to the ratio of the cooling sideband height with and without transport:

$$\mathcal{F} = \frac{\mathcal{S}_{\text{transport}}(\nu_{\text{cool}})}{\mathcal{S}_{\text{no transport}}(\nu_{\text{cool}})} . \quad (8.5)$$

The transport ramps are optimized by the iterative optical feedback method described in chapter 5.5.

The result of a linear transport of the $|\uparrow\rangle$ -state in dependency of the transport duration is shown in Figure 8.6 for three different trap depths. Similar to the previous measurements, we observe a high transport fidelity for multiples of the oscillation period of the atoms in the trap (blue). The theoretical model of the transport fidelity fit described in chapter 7.2 follows the measurement data with remarkable agreement (red). In harmonic approximation, the radial temperature T_{rad} is linear in the trapping frequency and shows the expected proportionality

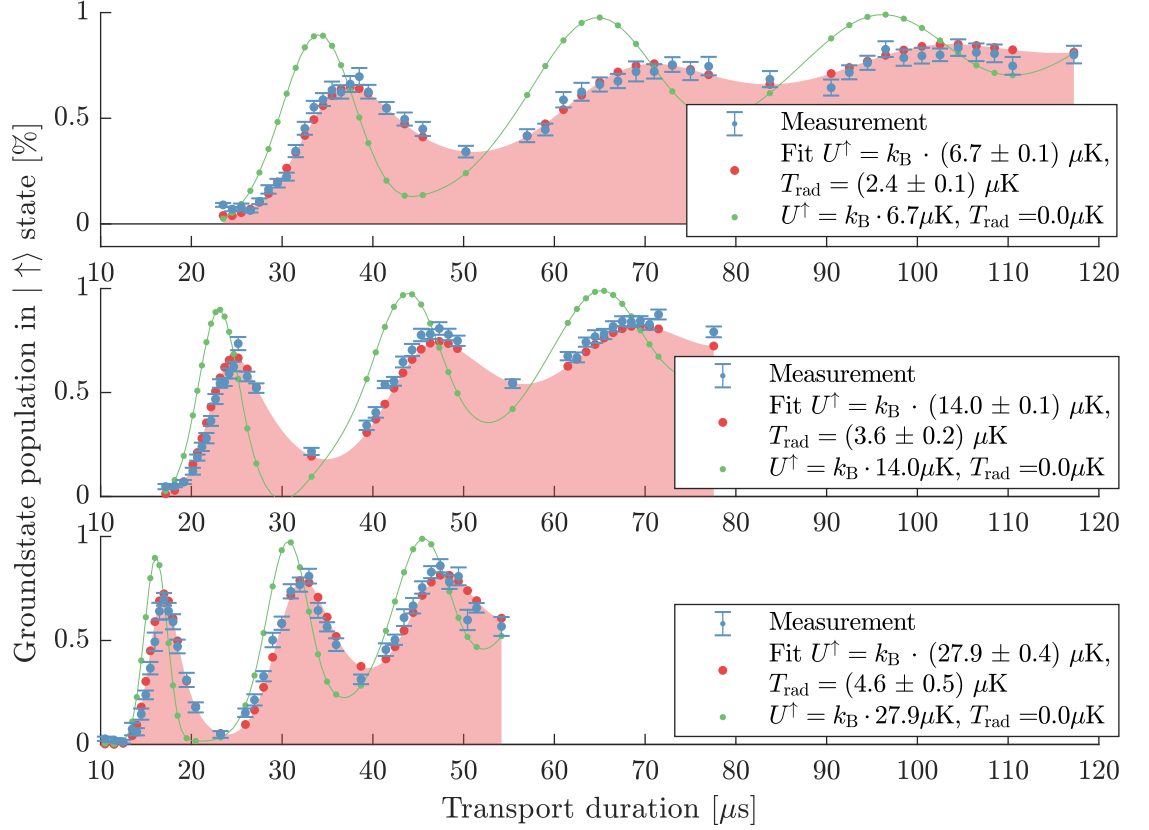


Figure 8.6: Measurement of the transport fidelity for linear transport: The three data sets are measured for three different trap depths. A high transport fidelity for multiples of the oscillation period of the atoms in the trap is observed (blue). A theoretical model of the transport fidelity (red) is a fit of the trap depth U^\uparrow and the temperature T_{rad} of the uncooled radial direction to the measurement data. It shows a remarkable agreement with the measured data. The radial motion strongly influences the transport in comparison to an atom in the three-dimensional ground state depicted in green.

with the square root of the trap depth within the fit error. A smaller trap depth leads to a shorter longitudinal oscillation period and results mainly in a shift of the peaks. To demonstrate the effect of the radial temperature the figure also shows the simulation for zero radial temperature in comparison (green). The peaks shift towards larger transport durations, since the atoms see a shallower effective trap depth on average. This averaging leads to a broadening of the peaks and to an asymmetric shape with a lower fidelity in the peak maximum. A fit of the linear transport measurements results in an one order of magnitude better estimate of the trap depth than a microwave spectrum with an error of a few $k_B \cdot \mu\text{K}$. With

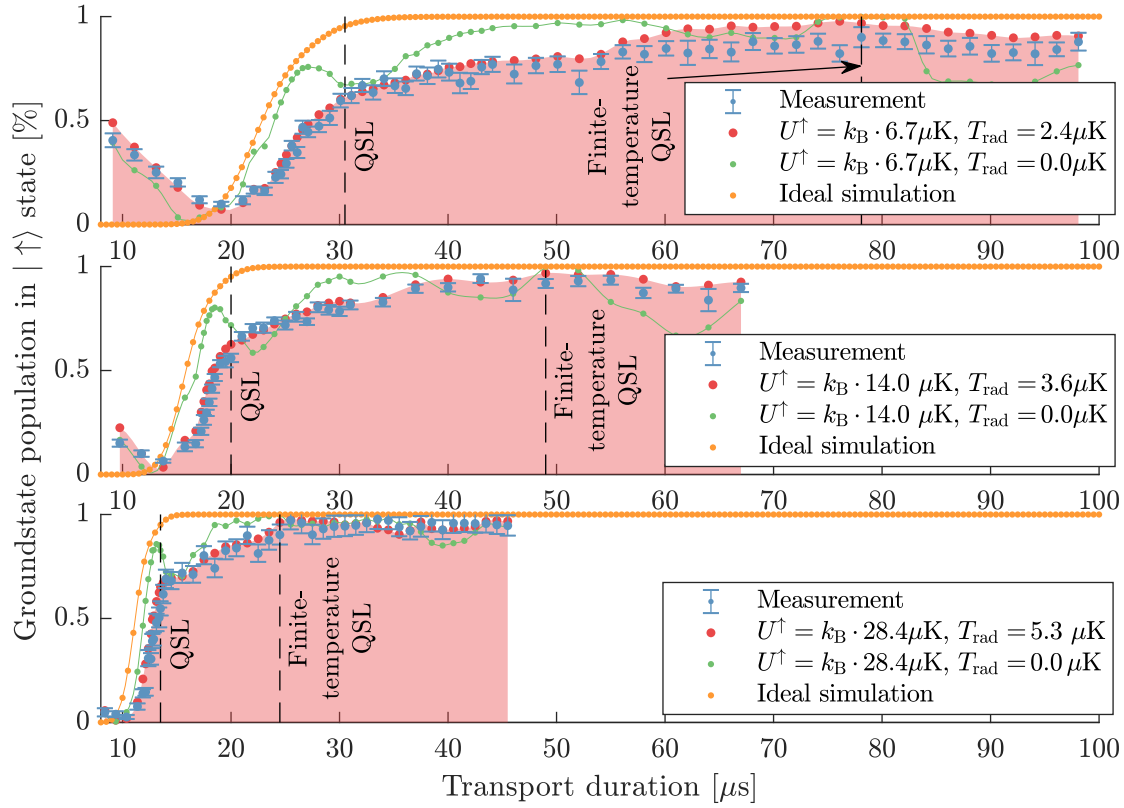


Figure 8.7: Measurement of the transport fidelity for optimal control transport: The three data sets are measured for the same three trap depths (blue) as for the previous measurement for linear transport in Fig. 8.6. From the measured data, the finite-temperature quantum speed limit (FTQSL) is estimated. It is defined as the transport duration, when the transport fidelity reaches 95 %. The theoretical model depicted by the red dots with an extrapolated area uses the fit result of the linear transport measurement. The ramps were originally optimized for trap depths of $U^\uparrow = k_B \cdot \{5.6, 12, 26\} \mu\text{K}$, which underestimates the trap depth a bit. The strong effect of the radial temperature is demonstrated by the zero-temperature model (green). A numerical calculation for ideal optimal control ramps and three-dimensional ground state cooling (orange) allows an estimate of the quantum speed limit (QSL).

this better estimate of the trap depths, the usage of optimal control ramps can be further improved.

Figure 8.7 shows the measurement data of optimal control transport in the $|\uparrow\rangle$ -state for the same choice of shallow trapping potentials. The theoretical model of the transport fidelity is calculated without free parameters and uses the fit result

from the linear transport measurement with remarkable agreement. The finite-temperature quantum speed limit is a rough estimate, because the optimal control ramps are determined for slightly different trap depths of $U^\dagger = k_B \cdot \{5.6, 12, 26\} \mu\text{K}$ and the execution of the transport ramps include imperfections and constraints as discussed in chapter 5.5. For comparison, the figure 8.7 also shows the numerical calculation for the measurement parameters, but at zero radial temperature. The rise of the fidelity for the shallow trap depth of $k_B \cdot 6.7 \mu\text{K}$ for transport durations below the quantum speed limit is, as previously mentioned, an artifact of our measurement technique, which measures the ground state population of all lattice sites. For driving ramps faster than the quantum speed limit time, a significant fraction of the ground state population remains in the initial lattice site.

The following table shows a summary of the quantum speed limit (QSL) for ideal optimal control ramps in the three-dimensional ground state and the larger finite-temperature quantum speed limit (FTQSL) determined from the measurements:

| Trap depth U^\dagger [$k_B \cdot \mu\text{K}$] | QSL [μs] | FTQSL [μs] | Radial temperature T_{rad} |
|--|-----------------------|-------------------------|-------------------------------------|
| 6.7 ± 0.1 | 30.5 ± 0.5 | 78.1 ± 1.0 | 2.4 ± 0.1 |
| 14.0 ± 0.1 | 20.0 ± 0.5 | 49.0 ± 1.0 | 3.6 ± 0.2 |
| 26.8 ± 0.2 (chapter 8.1) | 14.0 ± 0.5 | 25.0 ± 1.0 | 3.9 ± 0.3 |
| 27.9 ± 0.4 | 13.5 ± 0.5 | 24.5 ± 1.0 | 4.6 ± 0.5 |

Both measurement techniques used in this thesis agree within the error bars. Due to the astonishing agreement of the theoretical model and the measured data, we have a lot of confidence in our model, that we can predict the square-root dependency of the quantum speed limit on the trap depth.

8.3 Conclusion

In conclusion, the fundamental boundary of fast transport of thermal atoms by means of optimal control theory has been measured for the first time. The boundary was determined by measuring the transport fidelity of optimal control ramps in dependency of the transport duration. In order to determine the transport fidelity, a direct measurement technique of the groundstate population shows a significant improvement compared to an indirect technique based on a fit of the vibrational state occupation to a microwave spectrum. The finite-temperature quantum speed limit τ_{FTQSL} was estimated for three different trap depth. In order to measure τ_{QSL} of this system, we need to cool the atoms into the three-dimensional ground state, which can be achieved by additional Raman sideband cooling. This would allow us to reach even the zero-temperature quantum speed limit, which is smaller by

a factor 2.5. The analog control system works close to its bandwidth limitation for such fast atom transport. To enable quantum walk experiments at deeper trap depths at the quantum speed limit, a new digital control system is prepared to be installed. The system is based on a digital arbitrary waveform generator (M3300A from KeySight) with a bandwidth of up to 200 MHz and a sampling rate of $500 \cdot 10^6$ samples/s.

8.4 Outlook: Quantum speed limit of a static system

So far, we can measure the quantum speed limit for a driven system. However, many theoretical studies analyze the quantum speed limit in the regime of a freely evolving system. Since this regime was never explored experimentally, I want to propose a measurement with our state-dependent lattice to determine the quantum speed limit.

The unified bound

Physicists have analytically investigated the quantum speed limit for various types of quantum systems. The choice of the information metric that measures the distinguishability of two quantum states, results in a family of independent quantum speed limits that differ in tightness [139]. When restricting to orthogonal pure or mixed states in a static system described by a time-independent Hamiltonian, the unified bound is defined by [140]

$$t \geq \tau_{\text{QSL}} = \max \left\{ \tau_{\text{MT}}^{\text{QSL}}, \tau_{\text{ML}}^{\text{QSL}}, \dots \right\} \quad . \quad (8.6)$$

I propose a scheme to test the Mandelstam-Tamm ($\tau_{\text{MT}}^{\text{QSL}}$) and Margolus-Levitin ($\tau_{\text{ML}}^{\text{QSL}}$) bound, where I consider a process in which a state evolves freely into an orthogonal one after some time t :

$$\langle \psi(0) | \psi(t) \rangle = 0 \quad . \quad (8.7)$$

The quantum speed limit derived by Mandelstam and Tamm is given by the standard deviation of the energy ΔE during the evolution [121]:

$$\tau_{\text{MT}}^{\text{QSL}} = \frac{\pi \hbar}{2 \Delta E} \quad , \quad (8.8)$$

$$\Delta E = \sqrt{\langle \psi | \hat{H}^2 | \psi \rangle - \langle \psi | \hat{H} | \psi \rangle^2} \quad .$$

The derivation is based on the Cauchy-Schwarz inequality. This bound is not

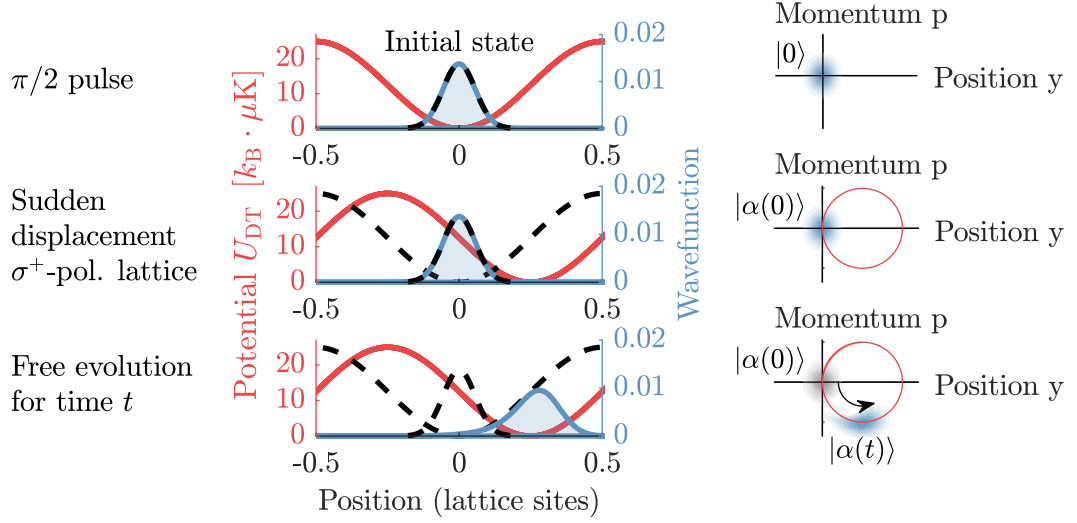


Figure 8.8: Measurement sequence to test the Mandelstam-Tamm and Margolus-Levitin bound: The left side shows the measurement sequence in top-to-bottom order and the right side illustrates the Wigner-function representation of the evolution of the atomic wave packet for the $|\uparrow\rangle$ -state. An atom is prepared in the ground state and transferred with a $\pi/2$ pulse into a superposition state. After a sudden displacement of the σ^+ -pol. lattice (red), the wave packet for the $|\uparrow\rangle$ -state (blue) is described by a coherent state $|\alpha(0)\rangle$. The wave packet for the $|\downarrow\rangle$ -state remains in the unshifted σ^- -pol. lattice (black dashed lines). After the free evolution time t , the Ramsey interferometer sequence is completed with a second $\pi/2$ pulse. The measured Ramsey fringe contrast directly quantifies the overlap $\langle\alpha(t)|\alpha(0)\rangle$.

always suitable, since it becomes arbitrarily small for diverging ΔE , although the average energy is finite [141]. The quantum speed limit defined by Margolus and Levitin is directly based on the average energy $\langle E \rangle$ and the ground state energy E_0 [142]:

$$\tau_{\text{ML}}^{\text{QSL}} = \frac{\pi \hbar}{2(\langle E \rangle - E_0)} \quad , \quad (8.9)$$

$$\langle E \rangle = \langle \psi | \hat{H} | \psi \rangle \quad .$$

Measurement scheme testing the Mandelstam-Tamm and Margolus-Levitin bound

In order to test the Mandelstam-Tamm and Margolus-Levitin bound, I propose a measurement scheme based on Ramsey interferometry. In this measurement the orthogonality of an initial and final state is determined. The sequence is shown in

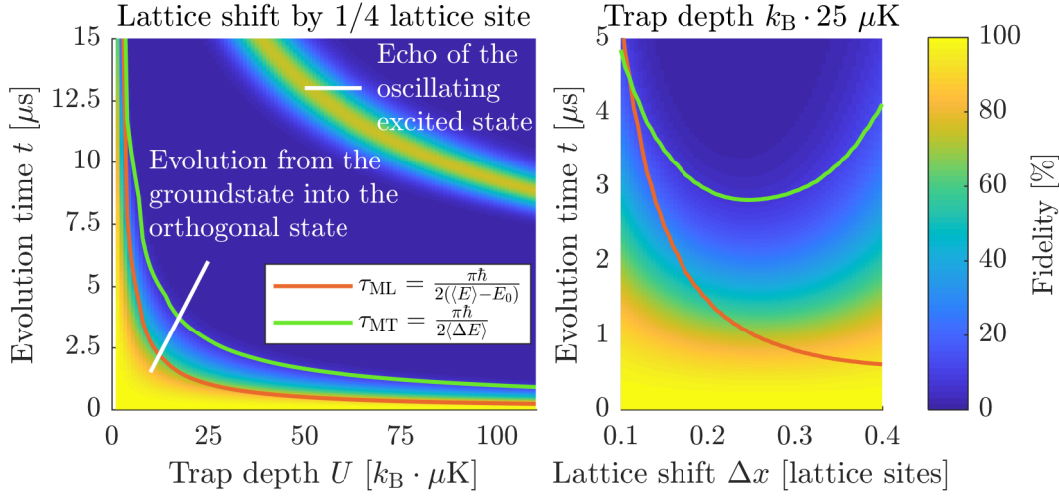


Figure 8.9: Numerical analysis of the quantum speed limit in a static system: The color-coded fidelity describes the overlap between the initial ground state and the evolved state for different evolution times t and trap depths U (left) as well as for different lattice shifts (right). The overlap vanishes only for $t \geq \tau_{\text{QSL}}$. I also show the analytically-derived bounds by Mandelstam-Tamm and Margolus-Levitin. The numerical calculation follows as expected the larger bound τ_{MT} . For long evolution times, a revival of the fidelity is observed.

Fig. 8.8. An atom is prepared in the ground state and transferred with a $\pi/2$ pulse into a superposition state in the overlapped state-dependent lattices:

$$\psi_{\text{init}} = \frac{1}{\sqrt{2}}(|\uparrow, n=0\rangle - |\downarrow, n=0\rangle) \quad . \quad (8.10)$$

The evolution is initiated by a sudden displacement $\Delta y \in (0, \lambda_{\text{DT}}/4)$ of the σ^+ -pol. lattice trapping the wave packet for the $|\uparrow\rangle$ -state. In harmonic approximation, the state in the shifted lattice is described by a coherent state:

$$|\alpha(t)\rangle = e^{i\omega t} D(\alpha) |0\rangle = e^{i\omega t} e^{-|\alpha|^2/2} \sum_{n=0}^{\infty} \frac{\alpha^n}{\sqrt{n!}} |n\rangle \quad . \quad (8.11)$$

The coherent state is generated by definition by the displacement operation $D(\alpha) = \exp(\alpha \hat{a}^\dagger - \alpha^* \hat{a})$. The wave packet for the $|\downarrow\rangle$ -state remains in the unshifted σ^- -pol. lattice. After the evolution time t , a second $\pi/2$ pulse is applied. The wavefunction is described by

$$|\psi(t)\rangle = \frac{1}{2} |\uparrow\rangle \otimes [|\alpha(t)\rangle - D(\alpha) |0\rangle] - \frac{1}{2} |\downarrow\rangle \otimes [D(-\alpha) |\alpha(t)\rangle + |0\rangle] \quad . \quad (8.12)$$

A subsequent push-out of the $|\uparrow\rangle$ -state and a survival measurement maps the state onto the $|\downarrow\rangle$ -state. We can trace the contrast of a Ramsey fringe, which quantifies directly the overlap of the initial ground state with the evolved state:

$$\begin{aligned} |\langle \downarrow | \psi(t) \rangle|^2 &= \frac{1}{4} |\langle \alpha(t) | + D(\alpha) | 0 \rangle|^2 \\ &= \frac{1}{2} + \frac{1}{2} \text{Re}[\langle \alpha(t) | D(\alpha) | 0 \rangle] \\ &= \frac{1}{2} + \frac{1}{2} \text{Re}[\langle \alpha(t) | \alpha(0) \rangle] \quad . \end{aligned} \tag{8.13}$$

Figure 8.9 shows a numerical calculation of $\text{Re}[\langle \alpha(t) | \alpha(0) \rangle]$ depending on the evolution time for different trap depths and lattice displacements. For these parameters, the bound by Mandelstam-Tamm is larger than the bound of Margolus-Levitin and the quantum speed limit is determined by $\tau_{\text{QSL}} = \tau_{\text{MT}}$. This is confirmed by the numerical calculation, which follows the higher bound. We also observe a revival of the fidelity after one oscillation period, which is expected to be 1 in an ideal harmonic trap.

The simulation predicts, that we are able to measure the Mandelstam-Tamm bound and explore the dynamics with our experimental setup. By choosing different trap depths, we can even analyze the regime of an harmonic trap in case of a deep trap as well as the influence of an anharmonic shape in case of a shallow lattice.

CHAPTER 9

CONCLUSION

This thesis presents results on motional control of atomic wave packets in optical lattices and introduces a novel concept of optimal transport: (i) The first part demonstrates three-dimensional ground state cooling in an optical dipole trap of an atom-cavity system. The measurement is interpreted with a newly developed temperature model. (ii) In the second part, I investigate a new method of fast atom transport without heating in a state-dependent lattice. By means of optimal control theory, transport ramps are derived and experimentally implemented.

The two-dimensional trap of an atom-cavity system was extended by a new blue-detuned dipole trap in order to strongly confine atoms in all three dimensions. This new confinement allows to use the recently developed method of carrier-free Raman sideband cooling additionally along the third direction. This technique is applicable without the need of additional lasers. The suppression of the carrier transition is achieved by trapping the atom in the zero-crossing of the electric field of one of the Raman beams and can lead to a five times higher cooling efficiency. The temperature in the three-dimensional trap is determined by the measurement of Raman sideband spectra. A new temperature model is derived to extract the information about the ground state population. The model includes the dynamics of Raman sideband couplings described by the Franck-Condon Hamiltonian and the anharmonic shape of the trapping potential. The ground state occupation of (94.5, 60.5, 89.8) % in x, y, z -direction, respectively, is achieved within milliseconds.

In a state-dependent lattice, the atoms are cooled into the one-dimensional ground state by means of microwave sideband cooling. Analog to the cooling scheme with Raman beams, a temperature model is derived for the microwave coupling and leads to a better fit to the measured sideband spectrum. A ground state population of 98 % is determined.

Fast atom transport is challenging, because it can heat atoms out of the ground state. New transport sequences are derived with an optimization algorithm based on optimal control theory. This numeric approach allows to optimize the trans-

port fidelity and to reduce the transport time by a factor two compared to previous transport schemes. The transport fidelity for the new optimal control ramps are measured with two techniques: The first technique is based on a fit of the temperature model to a microwave sideband spectrum to determine the ground state population before and after transport. The second technique is a direct detection of the vibrational state occupation. Both measurements show, that atoms can be transported faster, with larger fidelity and a higher robustness against experimental imperfections compared to previous conventional transport schemes.

The dynamics of multiple successive transport steps of an optimal control ramp are analyzed. Interference effects between the ground state and higher excited states are observed in a measurement, which leads to transport efficiencies that depend on the time delay between transport steps. For certain delay times, high transport fidelities of 98 % are achieved for up to 40 transport steps.

An alternative optimization algorithm is demonstrated to determine optimal transport sequences. The algorithm using live feedback of the experimental system is successfully demonstrated. The advantage of this method is, that knowledge of the system parameters is not required and experimental imperfections of the system can be compensated.

The fundamental limit of fast transport is given by the so-called quantum speed limit. It is based on an interpretation of Heisenberg's uncertainty relation, which states that the finite energy of a system leads to a minimum evolution time. The quantum speed limit is determined experimentally and the measurement shows an astonishing agreement with a theoretical analysis of the transport fidelity. It was measured, that the speed limit shows a square-root dependency on the trap depth of the lattice potential.

These results on optimized transport operations are crucial for all upcoming experiments based on coherent multi-path interference effects of atomic wave packets in optical lattices.

A APPENDIX

A.1 State-dependent lattice potential of the $|\downarrow\rangle$ -state

The derivation of the effective dipole potential experienced by the atoms for two state-dependent lattices is derived in this appendix. It closely follows the master thesis of Groh [83]. The $|\downarrow\rangle$ -state experience a contribution of both circularly polarized dipole traps, which is not negligible to perform optimal control transport of atoms. On the one hand, we want to calculate for given circularly polarized traps $\{U^{\sigma^-}, U^{\sigma^+}\}$ and arbitrary transport ramps $\{\varphi^{\sigma^-}, \varphi^{\sigma^+}\}$, the resulting effective potential depth U^\downarrow and movement along the lattice axis φ^\downarrow of an atom in the $|\downarrow\rangle$ -state. On the other hand, we want to design from a optimal control solution $\{U^{\sigma^+} = U^\uparrow, \varphi^{\sigma^+} = \varphi^\uparrow\}$ the driving ramp $\{U^{\sigma^-}, \varphi^{\sigma^-}\}$, such that the $|\downarrow\rangle$ -state experience the same ramp as the $|\uparrow\rangle$ -state. In the first case, we find an analytic solution while we apply an iterative approach for the second case.

A.1.1 Calculation of $\{U^\downarrow, \varphi^\downarrow\}$ from $\{U^{\sigma^-}, \varphi^{\sigma^-}\}$ and $\{U^{\sigma^+}, \varphi^{\sigma^+}\}$

The potential depth for the $|\downarrow\rangle$ -state is a mixture of both polarization components. This chapter shows that the trapping potential can be rewritten by an effective potential depth U^\downarrow , a phase ramp φ^\downarrow and an offset δU^\downarrow , which gets important for atom interferometry:

$$U_{\text{DT}}^\downarrow = \frac{7}{8}U_{\text{DT}}^{\sigma^-} + \frac{1}{8}U_{\text{DT}}^{\sigma^+} \stackrel{!}{=} U^\downarrow \cos^2 \left\{ (\varphi - \varphi^\downarrow)/2 \right\} - \delta U^\downarrow \quad . \quad (\text{A.1})$$

The circularly polarized trapping potential are similarly defined by

$$U_{\text{DT}}^{\sigma^+/\sigma^-} = U^{\sigma^+/\sigma^-} \cos^2 \left\{ (\varphi - \varphi^{\sigma^+/\sigma^-})/2 \right\} \quad . \quad (\text{A.2})$$

By using the relation $\cos^2(\alpha) = \frac{1}{2}(1 + \cos(2\alpha))$ and writing down eq. (A.1) using eq. (A.2) for specific phase φ , we get with:

$$\begin{aligned} s_\sigma &= \frac{7}{8}U^{\sigma^-} \sin\left\{\varphi^{\sigma^-}\right\} + \frac{1}{8}U^{\sigma^+} \sin\left\{\varphi^{\sigma^+}\right\} \quad , \\ c_\sigma &= \frac{7}{8}U^{\sigma^-} \cos\left\{\varphi^{\sigma^-}\right\} + \frac{1}{8}U^{\sigma^+} \cos\left\{\varphi^{\sigma^+}\right\} \quad , \\ U_{\text{Offset}} &= U^\downarrow - 2\delta U^\downarrow - \frac{7}{8}U^{\sigma^-} - \frac{1}{8}U^{\sigma^+} \quad . \end{aligned} \quad (\text{A.3})$$

$$\varphi = 0 : \quad U_{\text{Offset}} = c_\sigma - U^\downarrow \cos(\varphi^\downarrow) \quad , \quad (\text{A.4})$$

$$\varphi = \frac{\pi}{4} : \quad U_{\text{Offset}} = s_\sigma - U^\downarrow \sin(\varphi^\downarrow) \quad , \quad (\text{A.5})$$

$$\varphi = \frac{\pi}{2} : \quad U_{\text{Offset}} = -c_\sigma + U^\downarrow \cos(\varphi^\downarrow) \quad , \quad (\text{A.6})$$

$$\varphi = \frac{\pi}{4} + \varphi^\downarrow : \quad U_{\text{Offset}} = \frac{7}{8}U^{\sigma^-} \sin\left\{\varphi^{\sigma^-} - \varphi^\downarrow\right\} + \frac{1}{8}U^{\sigma^+} \sin\left\{\varphi^{\sigma^+} - \varphi^\downarrow\right\} \quad . \quad (\text{A.7})$$

By adding eq. (A.4) and (A.6), we find that $U_{\text{Offset}} = 0$ and we can determine δU^\downarrow from this. Furthermore, we can calculate $\tan\{\varphi^\downarrow\}$ from eq. (A.4) and (A.5), which determines φ^\downarrow . Finally, we use the result of φ^\downarrow with eq. (A.4) and the relation $\cos(\arctan(\alpha)) = (1 + \alpha^2)^{-1/2}$ to determine U^\downarrow :

$$\begin{aligned} \delta U^\downarrow &= \frac{1}{2} \left(U^\downarrow - \frac{7}{8}U^{\sigma^-} - \frac{1}{8}U^{\sigma^+} \right) \quad , \\ \varphi^\downarrow &= \arctan\left\{\frac{s_\sigma}{c_\sigma}\right\} \quad , \\ U^\downarrow &= \sqrt{s_\sigma^2 + c_\sigma^2} \quad . \end{aligned} \quad (\text{A.8})$$

A.1.2 Iterative approach to derive $\{U^{\sigma^-}, \varphi^{\sigma^-}\}$ from $\{U^{\sigma^+}, \varphi^{\sigma^+}\}$

We want to drive the same transport ramp for both spin states $\{U^\downarrow = U^\uparrow, \varphi^\downarrow = \varphi^\uparrow\}$. The ramps for the σ^+ -polarized dipole trap are given by $\{U^{\sigma^+} = U^\uparrow, \varphi^{\sigma^+} = \varphi^\uparrow\}$. However, the driving ramps for the σ^- -polarized dipole trap are determined iteratively in the following way. The result of U^\downarrow from eq. (A.8) is a quadratic function in U^{σ^-} . We use one of its solution $U^{\sigma^-}(\varphi^{\sigma^-})$. Secondly we calculate from eq. (A.7)

φ^{σ^-} in dependency of U^{σ^-} :

$$\begin{aligned}
 U^{\sigma^-}(\varphi^{\sigma^-}) &= \sqrt{128(U^\downarrow)^2 + \frac{(\varphi^{\sigma^+})^2}{2}(\cos\{2(\varphi^{\sigma^-} - \varphi^{\sigma^+})\} - 1)} - \frac{U^\uparrow}{7} \cos\{\varphi^{\sigma^-} - \varphi^{\sigma^+}\} \quad , \\
 \varphi^{\sigma^-}(U^{\sigma^-}) &= \varphi^\downarrow + \arcsin \left\{ \frac{U^{\sigma^+}}{7U^{\sigma^-}} \sin \left\{ \varphi^\downarrow - \varphi^{\sigma^-} \right\} \right\} \quad .
 \end{aligned}
 \tag{A.9}$$

As initial guess we use $\varphi_{\text{initial}}^{\sigma^-} = \varphi^{\sigma^+}$ and alternatingly solve both equations hundred times in order to converge towards U^{σ^-} and φ^{σ^-} .

A.2 Wannier states and eigenenergies of a standing wave potential

The stationary Schrödinger equation is solved numerically to determine the eigenstates or here, the so-called Wannier states, which defines the initial and target ground state $|\psi_{\text{init}}\rangle$ and $|\psi_{\text{target}}\rangle$ as well as the eigenenergies E_n . The system Hamiltonian is given by

$$\hat{H} = \frac{\hat{\mathbf{p}}^2}{2m_{\text{Cs}}} + U \cos^2(\mathbf{k}\hat{\mathbf{x}}) \quad . \quad (\text{A.10})$$

The Bloch theorem considers the periodicity of the lattice and the eigenvalue problem is set in a fixed finite volume and with an infinite family of solutions with discretely spaced eigenvalues with a band index n :

$$\hat{H} |n\rangle = E_n |n\rangle \quad . \quad (\text{A.11})$$

The derivatives $\hat{\mathbf{p}}^2 = -\hbar\partial_x^2$ in position space are approximated with the following discretized difference equation:

$$f''(x_i) = \frac{f(x_{i-1}) - 2f(x_i) + f(x_{i+1}))}{\Delta x^2} \quad . \quad (\text{A.12})$$

The momentum operator $\hat{\mathbf{p}}$ has only a diagonal form in momentum space compared to the representation in position space:

$$\hat{p} |\psi\rangle = \underbrace{\begin{Bmatrix} p_1 & 0 & 0 \\ 0 & \ddots & 0 \\ 0 & 0 & p_n \end{Bmatrix}}_{\text{momentum space}} |\psi_p\rangle = \frac{-\hbar}{\Delta x^2} \cdot \underbrace{\begin{Bmatrix} -2 & 1 & 0 & \dots & 0 & 1 \\ 1 & -2 & 1 & \ddots & 0 & 0 \\ 0 & 1 & -2 & \ddots & 0 & 0 \\ \vdots & \ddots & \ddots & \ddots & \vdots & \vdots \\ 0 & 0 & 0 & \dots & -2 & 1 \\ 1 & 0 & 0 & \dots & 1 & -2 \end{Bmatrix}}_{\text{position space}} |\psi_x\rangle \quad . \quad (\text{A.13})$$

Our quantum system shares an analogous system Hamiltonian as Bloch electrons in a crystal in condensed matter physics reduced to one dimension. The eigenstates in periodic media generally described by the Bloch functions are delocalized over the whole lattice as shown in Fig. A.1. The form is described by a plane wave in a continuum with the periodic term $u_K(x)$ depending on the Bravais lattice periodicity $\hat{U}(x+a) = \hat{U}(x)$ with the Bravais lattice vector $L = n_L a$ with the band index n_L and the lattice constant $a = \lambda/2$:

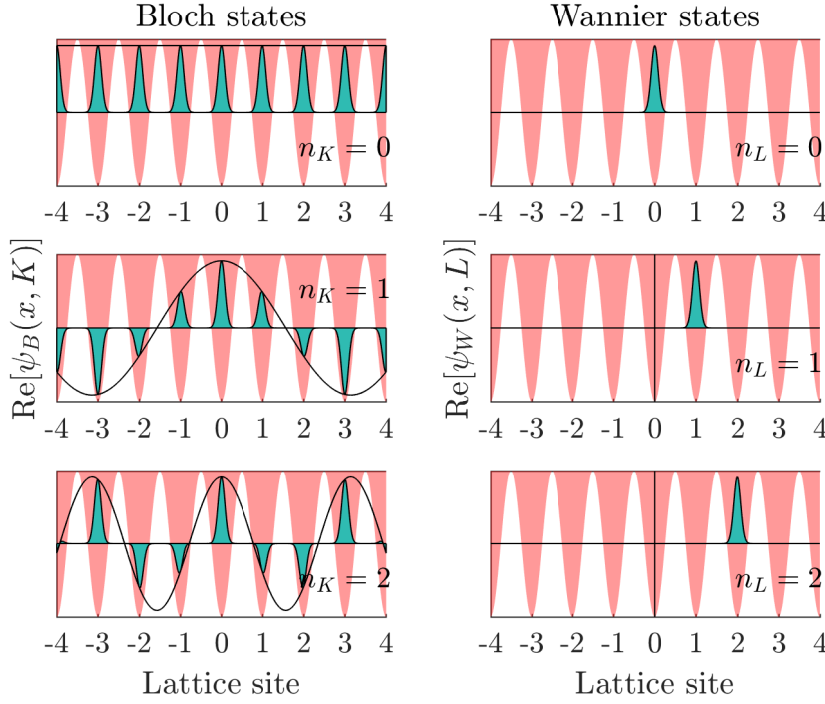


Figure A.1: The comparison between two real-space representations of the system vibrational eigenstate $n = 0$: The left side illustrates the delocalized Bloch states for the first three band indices n_K . It shows a periodic function $u_K(x)$ with an envelope e^{iKx} sketched as a black line. The Wannier states associated with the same vibrational number is a superposition of Bloch states with different K , which builds a localized wave packet. The phase factor e^{-iKL} is effectively translating the Wannier state by L . In the background is the red DT to illustrate the position of the sinusoidal lattice.

$$\psi_B(x, K) = e^{iKx} u_K(x) \quad . \quad (\text{A.14})$$

The momentum operator in eq. (A.13) is then defined in momentum space by the reciprocal wave number K of the Brillouin zones:

$$\hat{\mathbf{p}} = \hbar K \hat{\mathbf{e}}_p = \hbar \frac{2\pi}{a} n_K \hat{\mathbf{e}}_p \quad . \quad (\text{A.15})$$

with the band index n_K . G. Wannier introduced in 1937 a description of electrons in insulating crystals [143] by basic wave functions with properties similar to atomic functions. The model considers the limit, when the overlap between adjacent atoms is small, atomic separations are large and the wave packets get strongly located to the lattice center. The same functions can be applied to photonic crystal systems

[144, 145] and optical lattices [146]. The so called Wannier states form a complete, orthogonal basis, which still contains the full information about the band structure of the underlying crystal. They simplify the computations due to its minimum real-space spread over the lattice. The Wannier states are defined as a superposition of Bloch waves over all momenta K in the first Brillouin zone and N lattice sites as shown in Fig. A.1:

$$\begin{aligned}\psi_W(x, L) &= \frac{1}{\sqrt{N}} \sum_K e^{-iKL} \psi_B(x, K) \quad , \\ \psi_B(x, K) &= \frac{1}{\sqrt{N}} \sum_L e^{iKL} \psi_W(x, L) \quad .\end{aligned}\tag{A.16}$$

From A.14 and A.16 can be deduced that the phase e^{iKL} effectively shifts a localized Wannier state to another lattice site:

$$\psi_W(x, L = n_a a) = \psi_W(x - n_L a, L = 0) \quad .\tag{A.17}$$

For a transport over one lattice site, we identify the initial and target state with $|\psi_{\text{init}}\rangle = \psi_W(x, L = 0)$ and $|\psi_{\text{target}}\rangle = \psi_W(x, L = a)$ for the vibrational ground state $n = 0$. Furthermore we identify the periodic function $u_K(x)$ as the Bloch function for $K = 0$, which corresponds to a superposition of Wannier functions of different Brillouin zones:

$$\psi_B(x, K = 0) = u_K(x) = \sum_L \psi_W(x, L) \quad .\tag{A.18}$$

A.3 Symmetries of optimal control transport

Optimal control solutions show certain symmetries, which are confirmed in this proof.

Atom transport is in general invariant under time reversal operation and in the special case of a symmetric transport ramp invariant under a combination of a parity, time-reversal and translation operation, which I define as the symmetry operation. In the following we assume that for our transport ramps, which is defined as the tuple (φ, U) of a phase and an amplitude modulation, there exists an evolution operator $U_{\text{evo}}(T)$ with the Hamiltonian $\hat{H}(\varphi(t), U(t))$ in the form of

$$U_{\text{evo}}(T, \varphi, U) = \exp \left(-\frac{i}{\hbar} \int_0^T \hat{H}(\varphi(t), U(t)) dt \right) \quad \forall t \in [0, T] \quad , \quad (\text{A.19})$$

$$\hat{H}(\varphi(t), U(t)) = \frac{\hat{\mathbf{p}}^2}{2m_{\text{Cs}}} + U(t) \cos^2((\mathbf{k}\hat{\mathbf{x}} - \varphi(t))/2) \quad .$$

Under consideration of optimal control transport we are explicitly interested in the transport fidelity, which describes the overlap between the final state $|\psi(T)\rangle$ after transport with time T and a target state $|\psi_{\text{target}}\rangle$. For that purpose we define a class of transport ramps, which fulfill the condition that the fidelity is one

$$R_{\mathcal{F}=1} : \{\mathcal{F} = |\langle \psi_{\text{target}} | \psi(T) \rangle|^2 = 1\} \quad . \quad (\text{A.20})$$

In the following. we show that the fidelity is in general invariant under time-reversal operation $\hat{\Theta}$ and for specific class of symmetric ramps under a symmetry operation $\hat{\mathcal{S}}$

$$\begin{aligned} \hat{\Theta}\mathcal{F} &= \mathcal{F} \quad \forall(\varphi, U) \quad , \\ \hat{\mathcal{S}}\mathcal{F} &= \mathcal{F} \quad \forall(\varphi, U) \in R_{\hat{\mathcal{S}}} \quad . \end{aligned} \quad (\text{A.21})$$

Especially for the symmetry operation invariance, we additionally show that if a quantum speed limit exist, we can always find at least one symmetric optimal control ramp for a transport time larger or equal the quantum speed limit with fidelity one, which justifies our choice to describe the phase and amplitude modulation by a Fourier basis with sine functions.

A.3.1 Time-reversal invariance

The conventional reversal on a finite time window $[0, T]$ by the time reversal operator $\hat{\Theta}$ is described in Tab. A.1. The time reversal operator commutes with the Hamiltonian $[\hat{\Theta}, \hat{H}(t)] = 0$. In order to show the time-reversal invariance of the fidelity, it is enough to show that the wavefunction after transport is invariant under the operation, since the target state is time independent

$$\hat{\Theta} |\psi(T)\rangle = |\psi(T)\rangle \quad \forall(\varphi, U) \quad . \quad (\text{A.22})$$

| Parity | Time reversion | Translation | Symmetry |
|---|---|---|---|
| \hat{P} | $\hat{\Theta}$ | \hat{T}_d | $\hat{S} = \hat{P}\hat{\Theta}\hat{T}_d$ |
| unitary $\hat{P}\hat{P}^\dagger = \mathbb{1}$ | anti-unitary $\hat{\Theta}\hat{\Theta}^\dagger = -\mathbb{1}$ | unitary $\hat{T}_d\hat{T}_d^\dagger = \mathbb{1}$ | anti-unitary $\hat{S}\hat{S}^\dagger = -\mathbb{1}$ |
| $\hat{P}t = t\hat{P}$ | $\hat{\Theta}t = (T - t)\hat{\Theta}$ | $\hat{T}_dt = t\hat{T}_d$ | $\hat{S}t = (T - t)\hat{S}$ |
| $\hat{P}\hat{x} = -\hat{x}\hat{P}$ | $\hat{\Theta}\hat{x} = \hat{x}\hat{\Theta}$ | $\hat{T}_d\hat{x} = (\hat{x} + d)\hat{T}_d$ | $\hat{S}\hat{x} = (-\hat{x} + d)\hat{S}$ |
| $\hat{P}\hat{p} = -\hat{p}\hat{P}$ | $\hat{\Theta}\hat{p} = -\hat{p}\hat{\Theta}$ | $\hat{T}_d\hat{p} = \hat{p}\hat{T}_d$ | $\hat{S}\hat{p} = \hat{p}\hat{S}$ |
| $\hat{P}(i\hbar) = (i\hbar)\hat{P}$ | $\hat{\Theta}(i\hbar) = -(i\hbar)\hat{\Theta}$ | $\hat{T}_d(i\hbar) = (i\hbar)\hat{T}_d$ | $\hat{S}(i\hbar) = -(i\hbar)\hat{S}$ |
| $\hat{P} \psi(t)\rangle$ $= \psi(t)\rangle \hat{P}$ | $\hat{\Theta} \psi(t)\rangle$ $= \psi(T - t)\rangle^* \hat{\Theta}$ | $\hat{T}_d \psi(t)\rangle$ $ \psi(t)\rangle \hat{T}_d$ | $\hat{S} \psi(t)\rangle$ $ \psi(T - t)\rangle^* \hat{S}$ |

Table A.1: Characteristics of the parity, time reversal, translation and a combined operator.

An atom start at $t = 0$ in the ground state in the lattice potential and evolves into the state $|\psi(T)\rangle = U_{\text{evo}}(T) |\psi(t = 0)\rangle$. The final state is invariant under the time reversal operation:

$$\begin{aligned}
\hat{\Theta}|\psi(T)\rangle &= \hat{\Theta} \left[\exp \left(-\frac{i}{\hbar} \int_0^T \hat{H}(t') dt' \right) |\psi(t = 0)\rangle \right] \\
&= \exp \left(\frac{i}{\hbar} \int_T^0 \hat{H}(T - t') d(T - t') \right) |\psi(t = T)\rangle \\
&\stackrel{\text{substitute } \tilde{t}=T-t}{=} \exp \left(-\frac{i}{\hbar} \int_0^T \hat{H}(\tilde{t}') d\tilde{t}' \right) |\psi(x_0, \tilde{t} = 0)\rangle \\
&= |\psi(T)\rangle \quad .
\end{aligned} \tag{A.23}$$

A.3.2 Ramp symmetry and $\hat{P}\hat{\Theta}\hat{T}$ invariance

This chapter shows the proof that in case a quantum speed limit exist for an atom transport from an eigenstate to another eigenstate as in our system over a distance d in a time T , it can always be found at least one symmetric optimal control ramp with fidelity one. A class of symmetric optimal control ramp $R_{\hat{S}}$ is defined as a point symmetric phase ramp around the point $(T/2, d/2)$, which corresponds to half the transport distance at half the total transport time and an axial symmetric amplitude ramp around the axis $T/2$:

$$R_{\hat{S}} : \left\{ \begin{array}{l} \varphi(t) = kd - \varphi(T - t) \\ U(t) = U(T - t) \end{array} \right\} . \quad (\text{A.24})$$

In the following steps we choose an arbitrary ramp that is part of the class $R_{\mathcal{F}=1}$ defined in A.20. We proof that we can always construct a symmetric ramp with a different transport time T' , which is also in the class $R_{\mathcal{F}=1}$, by making use of the invariance of the Hamiltonian of a symmetric ramp under the symmetry operation. In a final proof, we show that in case of the existence of a speed limit, we always find a symmetric ramp in this limit.

First we show that the fidelity does not change if we let the state evolve for a time larger than the transport time T . For $T' > T$ the Hamiltonian is time-independent acting on the ground state $H(T) |\psi_{\text{target}}\rangle = E_{\text{target}} \hat{T}_d |\psi_0\rangle$. The additional evolution manifests in a global phase, which leaves the fidelity unchanged:

$$\begin{aligned} \mathcal{F} &= |\langle \psi_{\text{target}} | \psi(T) \rangle|^2 \\ &= |\langle \psi_{\text{target}} | \hat{U}_{\text{evo}}(T) | \psi_0 \rangle|^2 \\ &= |\langle \psi_{\text{target}} | \exp\left(-\frac{i}{\hbar} \int_0^T \hat{H}(t) dt\right) | \psi_0 \rangle|^2 \\ &= |\langle \psi_{\text{target}} | \exp\left(-\frac{i}{\hbar} (T' - T) E_{\text{target}}\right) \exp\left(-\frac{i}{\hbar} \int_0^T \hat{H}_S(t) dt\right) | \psi_0 \rangle|^2 \quad (\text{A.25}) \\ &= |\langle \psi_{\text{target}} | \exp\left(-\frac{i}{\hbar} \left(\int_T^{T'} \hat{H}(t) dt + \int_0^T \hat{H}(t) dt\right)\right) | \psi_0 \rangle|^2 \\ &= |\langle \psi_{\text{target}} | \hat{U}_{\text{evo}}(T') | \psi_0 \rangle|^2 . \end{aligned}$$

With the same argument the Hamiltonian can be extended by a time-independent term acting on the initial ground state $H(0) |\psi_0\rangle = E_0 |\psi_0\rangle$.

First we show if an arbitrary optimal control solution with fidelity one exists, we can construct a symmetric ramp with an equal or smaller transport time $T_{\hat{S}} \leq T$ with the same fidelity:

$$\exists \quad \{\varphi_{\mathcal{F}=1}, U_{\mathcal{F}=1}(t)\} \in R_{\mathcal{F}=1} \quad \Rightarrow \quad \exists \quad \{\varphi_{\hat{S}}, U_{\hat{S}}(t)\} \in \{R_{\hat{S}}, R_{\mathcal{F}=1}\} . \quad (\text{A.26})$$

The symmetric driving ramp is constructed in the following way around the point defined by half of the transport distance $(\tau, kd/2)$. In general two symmetric functions can be constructed with transport time $T_{\hat{S}} = 2\tau$ and $T_{\hat{S}} = 2(T - \tau)$, where we are interested in the shortest ramp:

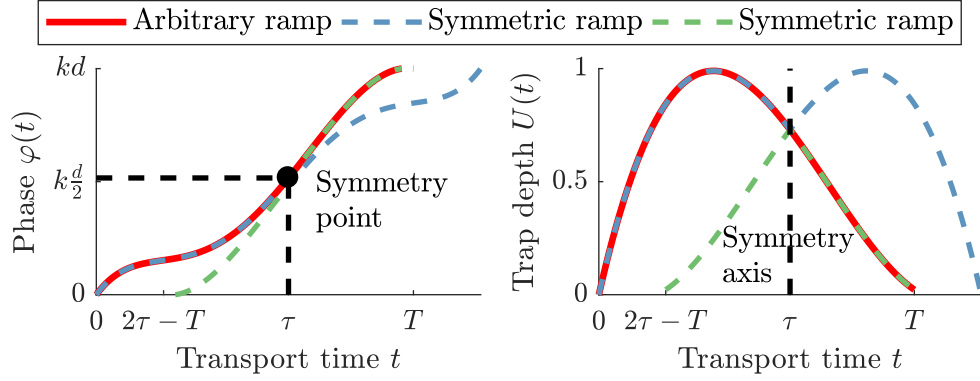


Figure A.2: Symmetric ramp construction: From an arbitrary ramp in phase or trap depth two symmetric ramps can be constructed, one with a transport duration of $T_S = 2\tau$ and one with $T_{\hat{S}} = 2(T - \tau)$. The phase ramp is point symmetric around the point $(\tau, kd/2)$ and the amplitude is axial symmetric around the axis at τ .

$$\begin{aligned}
 \tau \leq \frac{T}{2} : \quad & \begin{cases} \varphi_S(t) = \begin{cases} \varphi(t) & , t \leq \tau \\ kd - \varphi(2\tau - t) & , t > \tau \end{cases} \\ U_S(t) = \begin{cases} U(t) & , t \leq \tau \\ U(2\tau - t) & , t > \tau \end{cases} \end{cases} \\
 \tau > \frac{T}{2} : \quad & \begin{cases} \varphi_S(t) = \begin{cases} kd - \varphi(T - t) & , t \leq \tau \\ \varphi(t) & , t > \tau \end{cases} \\ U_S(t) = \begin{cases} U(T - t) & , t \leq \tau \\ U(t) & , t > \tau \end{cases} \end{cases} .
 \end{aligned} \tag{A.27}$$

It is useful to define the combined anti-unitary operator $\hat{S} = \hat{P}\hat{\Theta}\hat{T}_d$ of parity, time reversion and translation operation. The characteristics of these operators are summarized in Tab.A.1. The Hamiltonian of the symmetric ramp $H_{\hat{S}}(t)$ is simplified by using eq. (A.27) to

$$\begin{aligned}
 \tau \leq \frac{T}{2} : \quad & H_{\hat{S}}(t) = \begin{cases} H(t) & , t \leq \tau \\ \hat{S}H(t)\hat{S}^\dagger & , t > \tau \end{cases} \\
 \tau > \frac{T}{2} : \quad & H_{\hat{S}}(t) = \begin{cases} \hat{S}H(t)\hat{S}^\dagger & , t \leq \tau \\ H(t) & , t > \tau \end{cases} .
 \end{aligned} \tag{A.28}$$

Furthermore, we find that the symmetric Hamiltonian is invariant under the op-

eration \hat{S} :

$$\begin{aligned}
\hat{S}^\dagger H_{\hat{S}}(T) \hat{S} &= \frac{\hat{p}^2}{2m_{Cs}} + U_{\hat{S}}(T-t) \cos^2((-k(\hat{x}-d) - \varphi_{\hat{S}}(T-t))/2) \\
&= \frac{\hat{p}^2}{2m_{Cs}} + U_{\hat{S}}(t) \cos^2((-k(\hat{x}-d) - (kd - \varphi_{\hat{S}}(t)))/2) \\
&= \frac{\hat{p}^2}{2m_{Cs}} + U_{\hat{S}}(t) \cos^2((k\hat{x} - \varphi_{\hat{S}}(t))/2) \\
&= H_{\hat{S}}(t) \quad ,
\end{aligned} \tag{A.29}$$

and in case the Hamiltonian fulfills $H_{\hat{S}}(t) = \hat{S}H(t)\hat{S}^\dagger$, the \hat{S} invariance lead to

$$\begin{aligned}
H_{\hat{S}}(t) &\stackrel{A.29}{=} \hat{S}^\dagger H_{\hat{S}}(T) \hat{S} \\
&\stackrel{A.28}{=} \hat{S}^\dagger \hat{S} H(t) \hat{S} \hat{S}^\dagger \\
&= H(t) \quad ,
\end{aligned} \tag{A.30}$$

and the symmetric Hamiltonian $H_{\hat{S}}(t)$ is fully expressed by the original Hamiltonian $H(t)$. The fidelity for the symmetric driving ramp is equal to that of the original driving ramp. We are interested in the case $T_{\hat{S}} \leq T$:

$$\begin{aligned}
\mathcal{F}_{\hat{S}} &= |\langle \psi_{\text{target}} | \psi_S(T_{\hat{S}}) \rangle|^2 \\
&= |\langle \psi_{\text{target}} | \hat{U}_{\hat{S},\text{evo}}(T_{\hat{S}}) | \psi_0 \rangle|^2 \\
&\stackrel{A.25}{=} |\langle \psi_{\text{target}} | \hat{U}_{\hat{S},\text{evo}}(T) | \psi_0 \rangle|^2 \\
&\stackrel{A.28, A.30}{=} |\langle \psi_{\text{target}} | \hat{U}_{\text{evo}}(T) | \psi_0 \rangle|^2 \\
&= \mathcal{F} \quad .
\end{aligned} \tag{A.31}$$

If a quantum speed limit exists, the driving ramp at this limit necessarily goes through the symmetry point $(\tau, kd/2)$, since otherwise we can construct a symmetric ramp with a shorter transport time and same fidelity. In case this driving ramp is not element of the symmetric functions, we can still construct a symmetric ramp with the same transport time and fidelity. From eq. (A.25) follows the final conclusion, that if a quantum speed limit exists, we always find at least one symmetric driving ramp for all transport times larger than the quantum speed limit:

$$\exists T_{\text{QSL}} \quad \Rightarrow \quad \exists \{U(t), \varphi(t)\} \in \{R_{\hat{S}}, R_{\mathcal{F}=1}\} \quad \forall T \geq T_{\text{QSL}} \quad . \tag{A.32}$$

BIBLIOGRAPHY

- [1] J. I. Cirac and P. Zoller. Goals and opportunities in quantum simulation. *Nature Physics*, 8(4):264–266, 2012.
- [2] R. P. Feynman. Simulating physics with computers. *International Journal of Theoretical Physics*, 21(6-7):467–488, 1982.
- [3] Joel E. Moore. The birth of topological insulators. *Nature*, 464(7286):194–198, 2010.
- [4] C. Weitenberg, M. Endres, J. F. Sherson, M. Cheneau, P. Schau, T. Fukuhara, I. Bloch, and S. Kuhr. Single-spin addressing in an atomic Mott insulator. *Nature*, 471(7338):319–325, 2011.
- [5] A. Aspuru-Guzik and P. Walther. Photonic quantum simulators. *Nature Physics*, 8(4):285–291, 2012.
- [6] D. S. Weiss and M. Saffman. Quantum computing with neutral atoms. *Physics Today*, 70(7):45–50, 2017.
- [7] R. Blatt and C. F. Roos. Quantum simulations with trapped ions. *Nature Physics*, 8(4):277–284, 2012.
- [8] A. A. Houck, H. E. Türeci, and J. Koch. On-chip quantum simulation with superconducting circuits. *Nature Physics*, 8(4):292–299, 2012.
- [9] Yuriy Makhlin, Gerd Schön, and Alexander Shnirman. Quantum-state engineering with Josephson-junction devices. *Reviews of Modern Physics*, 73(2):357–400, 2001.
- [10] V. B. Braginskiĭ, A. B. Manukin, and M. Yu. Tikhonov. Investigation of Dissipative Ponderomotive Effects of Electromagnetic Radiation. *Soviet Physics JETP*, 31(5):829, 1970.
- [11] J. H. N. Loubser and J. A. van Wyk. Electron spin resonance in the study of diamond. *Reports on Progress in Physics*, 41(8):1201–1248, 1978.

- [12] A. I. Ekimov and A. A. Onushchenko. Quantum size effect in three-dimensional micorscopic semiconductor crystals. *Soviet Physics JETP Letters*, 34:345–349, 1981.
- [13] I. Bloch, J. Dalibard, and S. Nascimbène. Quantum simulations with ultracold quantum gases. *Nature Physics*, 8(4):267–276, 2012.
- [14] D. J. Wineland, R. E. Drullinger, and F. L. Walls. Radiation-pressure cooling of bound resonant absorbers. *Physical Review Letters*, 40(25):1639–1642, 1978.
- [15] W. Paul. Electromagnetic traps for charged and neutral particles. *Reviews of Modern Physics*, 62(3):531–540, 1990.
- [16] T. W. Hänsch and A. L. Schawlow. Cooling of gases by laser radiation. *Optics Communications*, 13:68–69, 1975.
- [17] E. L. Raab, M. Prentiss, A. Cable, S. Chu, and D. E. Pritchard. Trapping of Neutral Sodium Atoms with Radiation Pressure. *Physical Review Letters*, 59(23):2631–2634, 1987.
- [18] T. Bergeman, G. Erez, and H. J. Metcalf. Magnetostatic trapping fields for neutral atoms. *Physical Review A*, 35(4):1535–1546, 1987.
- [19] P. S. Jessen and I. H. Deutsch. Optical Lattices. *Advances in Atomic, Molecular and Optical Physics*, 37(C):95–138, 1996.
- [20] H. F. Hess. Evaporative cooling of magnetically trapped and compressed spin-polarized hydrogen. *Physical Review B*, 34(5):3476–3479, 1986.
- [21] W. Ketterle and N. J. van Druten. Bose-Einstein condensation of a finite number of particles trapped in one or three dimensions. *Physical Review A - Atomic, Molecular, and Optical Physics*, 54(1):656–660, 1996.
- [22] B. P. Anderson, T. L. Gustavson, and M. A. Kasevich. Atom trapping in nondissipative optical lattices. *Physical Review A - Atomic, Molecular, and Optical Physics*, 53(6):3727–3730, 1996.
- [23] M. Karski. *State-selective transport of single neutral atoms*. PhD thesis, Universität Bonn, 2010.
- [24] C. Robens, S. Brakhane, W. Alt, D. Meschede, J. Zopes, and A. Alberti. Fast, High-Precision Optical Polarization Synthesizer for Ultracold-Atom Experiments. *Physical Review Applied*, 9(3):34016, 2018.

-
- [25] D. Schrader, S. Kuhr, W. Alt, M. Müller, V. Gomer, and D. Meschede. An optical conveyor belt for single neutral atoms. *Applied Physics B: Lasers and Optics*, 73(8):819–824, 2001.
 - [26] D. A. Steck. Cesium D Line Data. *Theoretical Division*, 4710(7):1–31, 2008.
 - [27] G. Kirchhoff and R. Bunsen. Chemische Analyse durch Spectralbeobachtungen. *Annalen der Physik und Chemie*, 7(189):337–381, 1860.
 - [28] P. Zeeman. On the influence of magnetism on the nature of the light emitted by a substance. *American Journal of Physics*, 16:218, 1897.
 - [29] C. Robens, J. Zopes, W. Alt, S. Brakhane, D. Meschede, and A. Alberti. Low-Entropy States of Neutral Atoms in Polarization-Synthesized Optical Lattices. *Physical Review Letters*, 118(6):1–9, 2017.
 - [30] C. Robens. *Testing the Quantumness of Atom Trajectories*. PhD thesis, Universität Bonn, 2017.
 - [31] C. Wieman and T. W. Hänsch. Doppler-Free Laser Polarization Spectroscopy. *Physical Review Letters*, 36:1170, 1976.
 - [32] J. Dalibard and C. Cohen-Tannoudji. Laser cooling below the Doppler limit by polarizationgradients: simple theoretical models. *Journal of the Optical Society of America B*, 6(11):2023–2045, 1989.
 - [33] R. Grimm, M. Weidemüller, and Y. B. Ovchinnikov. Optical Dipole Traps for Neutral Atoms. *Advances in Atomic, Molecular and Optical Physics*, 42(C):95–170, 2000.
 - [34] S. Haroche and J.-M. Raimond. *Exploring the Quantum: Atoms, Cavities, and Photons*. Oxford University Press, 2006.
 - [35] J. Miguel-Sánchez, A. Reinhard, E. Togan, T. Volz, A. Imamoglu, B. Besga, J. Reichel, and J. Estève. Cavity quantum electrodynamics with charge-controlled quantum dots coupled to a fiber Fabry-Perot cavity. *New Journal of Physics*, 15, 2013.
 - [36] J. Benedikter, H. Kaupp, T. Hümmer, Y. Liang, A. Bommer, C. Becher, A. Krueger, J. M. Smith, T. W. Hänsch, and D. Hunger. Cavity-Enhanced Single-Photon Source Based on the Silicon-Vacancy Center in Diamond. *Physical Review Applied*, 7(2):1–12, 2017.

- [37] A. Jeantet, Y. Chassagneux, C. Raynaud, P. Roussignol, J. S. Lauret, B. Besga, J. Estève, J. Reichel, and C. Voisin. Widely Tunable Single-Photon Source from a Carbon Nanotube in the Purcell Regime. *Physical Review Letters*, 116(24):1–5, 2016.
- [38] J. McKeever, A. Boca, A. D. Boozer, R. Miller, J. R. Buck, A. Kuzmich, and H. J. Kimble. Deterministic Generation of Single Photons from One Atom. *Science*, 303(5666):1992–1995, 2004.
- [39] A. Reiserer, N. Kalb, G. Rempe, and S. Ritter. A quantum gate between a flying optical photon and a single trapped atom. *Nature*, 508(7495):237–240, 2014.
- [40] T. Wilk, S. C Webster, A. Kuhn, and G. Rempe. Single-Atom Single-Photon Quantum Interface. *Science*, 317(5837):488–490, 2007.
- [41] J. I. Cirac, P. Zoller, H. J. Kimble, and H. Mabuchi. Quantum State Transfer and Entanglement Distribution among Distant Nodes in a Quantum Network. *Physical Review Letters*, 78(16):3221–3224, 1997.
- [42] H. J. Kimble. The quantum internet. *Nature*, 453(7198):1023–1030, 2008.
- [43] L. M. Duan, M. D. Lukin, J. I. Cirac, and P. Zoller. Long-distance quantum communication with atomic ensembles and linear optics. *Nature*, 414(6862):413–418, 2001.
- [44] I. Dotsenko. *Single atoms on demand for cavity QED experiments*. PhD thesis, Universität Bonn, 2007.
- [45] S. Reick. *Internal and external dynamics of a strongly-coupled atom-cavity system*. PhD thesis, Universität Bonn, 2009.
- [46] T. Kampschulte. *Coherently driven three-level atoms in an optical cavity*. PhD thesis, Universität Bonn, 2011.
- [47] R. Reimann. *Cooling and Cooperative Coupling of Single Atoms in an Optical Cavity*. PhD thesis, Universität Bonn, 2014.
- [48] I. Dotsenko, W. Alt, M. Khudaverdyan, S. Kuhr, D. Meschede, Y. Miroshnichenko, D. Schrader, and A. Rauschenbeutel. Submicrometer position control of single trapped neutral atoms. *Physical Review Letters*, 95(3):1–4, 2005.

-
- [49] M. J. Gibbons, C. D. Hamley, C. Y. Shih, and M. S. Chapman. Nondestructive fluorescent state detection of single neutral atom qubits. *Physical Review Letters*, 106(13):2–5, 2011.
- [50] A. Fuhrmanek, R. Bourgain, Y. R.P. Sortais, and A. Browaeys. Free-space lossless state detection of a single trapped atom. *Physical Review Letters*, 106(13):2–5, 2011.
- [51] A. H. Myerson, D. J. Szwer, S. C. Webster, D. T.C. Allcock, M. J. Curtis, G. Imreh, J. A. Sherman, D. N. Stacey, A. M. Steane, and D. M. Lucas. High-fidelity readout of trapped-ion qubits. *Physical Review Letters*, 100(20):2–5, 2008.
- [52] D. Schrader. *A neutral atom quantum register*. PhD thesis, Universität Bonn, 2004.
- [53] J. Bochmann, M. Mücke, C. Guhl, S. Ritter, G. Rempe, and D. L. Moehring. Lossless state detection of single neutral atoms. *Physical Review Letters*, 104(20):2–5, 2010.
- [54] G. Hechenblaikner, M. Gangl, P. Horak, and H. Ritsch. Cooling an atom in a weakly driven high-Q cavity. *Physical Review A - Atomic, Molecular, and Optical Physics*, 58(4):3030–3042, 1998.
- [55] M. H. Anderson, J. R. Ensher, M. R. Matthews, C. E. Wieman, and E. A. Cornell. Observation of Bose-Einstein condensation in a dilute atomic vapor. *Science*, 269(5221):198–201, 1995.
- [56] F. Diedrich, J. C. Bergquist, Wayne M. Itano, and D. J. Wineland. Laser Cooling to the Zero-Point Energy of Motion. *Physical Review Letters*, 62(4):403–406, 1989.
- [57] M. Karski, L. Förster, J. M. Choi, A. Steffen, W. Alt, D. Meschede, and A. Widera. Quantum walk in position space with single optically trapped atoms. *Science*, 325(5937):174–177, 2009.
- [58] X. Li, T. A. Corcovilos, Y. Wang, and D. S. Weiss. 3D projection sideband cooling. *Physical Review Letters*, 108(10):1–4, 2012.
- [59] B. Albrecht, Y. Meng, C. Clausen, A. Dareau, P. Schneeweiss, and A. Rauschenbeutel. Fictitious magnetic-field gradients in optical microtraps as an experimental tool for interrogating and manipulating cold atoms. *Physical Review A*, 94(6), 2016.

- [60] M. Kasevich and S. Chu. Laser cooling below a photon recoil with three-level atoms. *Physical Review Letters*, 69(12):1741–1744, 1992.
- [61] J. Reichel, O. Morice, G. M. Tino, and C. Salomon. Subrecoil raman cooling of cesium atoms. *Europhysics Letters*, 28(7):477–482, 1994.
- [62] C. Monroe, D. M. Meekhof, B. E. King, S. R. Jefferts, W. M. Itano, D. J. Wineland, and P. Gould. Resolved-sideband Raman cooling of a bound atom to the 3D zero-point energy. *Physical Review Letters*, 75(22):4011–4014, 1995.
- [63] R. Reimann, W. Alt, T. Macha, D. Meschede, N. Thau, S Yoon, and L. Ratschbacher. Carrier-free Raman manipulation of trapped neutral atoms. *New Journal of Physics*, 16, 2014.
- [64] K. Bergmann, H. Theuer, and B. W. Shore. Coherent population transfer among quantum states of atoms and molecules. *Reviews of Modern Physics*, 70(3):1003–1025, 1998.
- [65] J. Franck and E. G. Dymond. Elementary processes of photochemical reactions. *Transactions of the Faraday Society*, 21:536, 1926.
- [66] D. Leibfried, R. Blatt, C. Monroe, and D. Wineland. Quantum dynamics of single trapped ions. *Review of Modern Physics*, 75(1):281–324, 2003.
- [67] A. D. Boozer. Theory of Raman transitions in cavity QED. *Physical Review A*, 78(3):033406, 2008.
- [68] M. L. Skolnick and R. J. Freiberg. Laser Injection Locking. *Proceedings of the IEEE*, 61(10):1411–1431, 1973.
- [69] K. Schörner. Ein phasenstabilisiertes Lasersystem für resonatorinduzierte Raman-Prozesse, 2008. Diplom thesis, Universität Bonn.
- [70] S. Chu, L. Hollberg, J. E. Bjorkholm, A. Cable, and A. Ashkin. Three-dimensional viscous confinement and cooling of atoms by resonance radiation pressure. *Physical Review Letters*, 55(1):48, 1985.
- [71] S. Chu, L. Hollberg, J. E. Bjorkholm, A. Cable, and A. Ashkin. A Heterodyne Measurement of the Fluorescence Spectrum of Optical Molasses. *Laser spectroscopy IX*, pages 8–11, 1989.
- [72] L. Förster. *Microwave control of atomic motion in a spin dependent optical lattice*. PhD thesis, Universität Bonn, 2010.

-
- [73] A. Steffen. *Single atom interferometers and Bloch oscillations in quantum walks*. PhD thesis, Universität Bonn, 2013.
- [74] A. Couvert, T. Kawalec, G. Reinaudi, and D. Guéry-Odelin. Optimal transport of ultracold atoms in the non-adiabatic regime. *Europhysics Letters*, 83(1), 2008.
- [75] A Lengwenus, J Kruse, M Schlosser, S Tichelmann, and G Birkel. Coherent Transport of Atomic Quantum States in a Scalable Shift Register. *Physical Review Letters*, 105(17):3–6, 2010.
- [76] D. Barredo, S. de Léséleuc, V. Lienhard, T. Lahaye, and A. Browaeys. An atom-by-atom assembler of defect-free arbitrary two-dimensional atomic arrays. *Science*, 354(6315):1021–1023, 2016.
- [77] H. Kim, W. Lee, H. G. Lee, H. Jo, Y. Song, and J. Ahn. In situ single-atom array synthesis using dynamic holographic optical tweezers. *Nature Communications*, 7:1–8, 2016.
- [78] M. Endres, H. Bernien, A. Keesling, H. Levine, E. R. Anschuetz, A. Krajenbrink, C. Senko, V. Vuletic, M. Greiner, and M. D. Lukin. Atom-by-atom assembly of defect-free one-dimensional cold atom arrays. *Science*, 354(6315):1024–1027, 2016.
- [79] S. Kuhr, W. Alt, D. Schrader, M. Müller, V. Gomer, and D. Meschede. Deterministic delivery of a single atom. *Science*, 293(5528):278–280, 2001.
- [80] A. Steffen, A. Alberti, W. Alt, N. Belmechri, S. Hild, M. Karski, A. Widera, and D. Meschede. A digital atom interferometer with single particle control on a discretized spacetime geometry. *Proceedings of the National Academy of Sciences*, 109:9770, 2012.
- [81] O. Mandel, M. Greiner, A. Widera, T. Rom, T. W. Hänsch, and I. Bloch. Coherent Transport of Neutral Atoms in Spin-Dependent Optical Lattice Potentials. *Physical Review Letters*, 91(1):1–4, 2003.
- [82] D. Jaksch, H. J. Briegel, J. I. Cirac, C. W. Gardiner, and P. Zoller. Entanglement of atoms via cold controlled collisions. *Physical Review Letters*, 82(9):1975–1978, 1999.
- [83] T. Groh. Fast transport of single atoms in optical lattices using quantum optimal control, 2018. Master thesis, University of Bonn.
- [84] A. V. Oppenheim and A. S. Willsky. *Signals and systems*. Pearson, 1996.

- [85] M. Karski, L. Förster, J. Choi, W. Alt, A. Alberti, A. Widera, and D. Meschede. Direct Observation and Analysis of Spin-Dependent Transport of Single Atoms in a 1D Optical Lattice. *Journal of the Korean Physical Society*, 59:2947, 2011.
- [86] N. Belmechri, L. Förster, W. Alt, A. Widera, D. Meschede, and A. Alberti. Microwave control of atomic motional states in a spin-dependent optical lattice. *Journal of Physics B: Atomic, Molecular and Optical Physics*, 46(10), 2013.
- [87] G. G. Balint-Kurti, S. Zou, and A. Brown. *Advances in Chemical Physics*. John Wiley & Sons, Inc., 2008.
- [88] J. M. Longuski, J. J. Guzmán, and J. E. Prussing. *Optimal Control with Aerospace Applications*. Springer-Verlag, 2014.
- [89] J. Zhu, E. Trélat, and M. Cerf. Geometric Optimal Control and Applications to Aerospace. *Pacific Journal of Mathematics for Industry*, 9(8), 2017.
- [90] J. D. Lee. Application of optimal control theory to flexible robotic manipulators. *Robotics and Computer-Integrated Manufacturing*, 7(3):327–335, 1991.
- [91] T. A. Weber. *Optimal Control Theory with Applications in Economics*. The MIT Press.
- [92] J. Werschnik and E. K. U. Gross. Quantum Optimal Control Theory. *Journal of Physics B: Atomic, Molecular and Optical Physics*, 40(18), 2007.
- [93] L. D. Berkovitz. *Optimal Control Theory*. Springer-Verlag, 1974.
- [94] C. Brif, R. Chakrabarti, and H. Rabitz. Control of quantum phenomena: Past, present and future. *New Journal of Physics*, 12, 2010.
- [95] A. Assion, T. Baumert, M. Bergt, T. Brixner, B. Kiefer, V. Seyfried, M. Strehle, and G. Gerber. Control of chemical reactions by feedback-optimized phase-shaped femtosecond laser pulses. *Science*, 282(5390):919–922, 1998.
- [96] T. C. Weinacht, J. Ahn, and P. H. Bucksbaum. Controlling the shape of a quantum wavefunction. *Nature*, 397(6716):233–235, 1999.
- [97] H. Rabitz, R. De Vivie-Riedle, M. Motzkus, and K. Kompa. Whither the future of controlling quantum phenomena? *Science*, 288(5467):824–828, 2000.

-
- [98] C. P. Koch, J. P. Palao, R. Kosloff, and F. Masnou-Seeuws. Stabilization of ultracold molecules using optimal control theory. *Physical Review A - Atomic, Molecular, and Optical Physics*, 70(1):1–14, 2004.
- [99] N. Accanto, P. M. de Roque, M. Galvan-Sosa, S. Christodoulou, I. Moreels, and N. F. van Hulst. Rapid and robust control of single quantum dots. *Light: Science & Applications*, 6(3), 2016.
- [100] P. B. Wigley, P. J. Everitt, A. Van Den Hengel, J. W. Bastian, M. A. Sooriyabandara, G. D. McDonald, K. S. Hardman, C. D. Quinlivan, P. Manju, C. C.N. Kuhn, I. R. Petersen, A. N. Luiten, J. J. Hope, N. P. Robins, and M. R. Hush. Fast machine-learning online optimization of ultra-cold-atom experiments. *Scientific Reports*, 6(25890):1–6, 2016.
- [101] A. M. Childs. Universal computation by quantum walk. *Physical Review Letters*, 102(18):1–4, 2009.
- [102] J. F. Monahan. *Numerical Methods of Statistics*, volume 1. Cambridge University Press, 2011.
- [103] J. A. Fleck, J. R. Morris, and M. D. Feit. Applied Physics Time-Dependent Propagation of High Energy Laser Beams through the Atmosphere. *Applied Physics*, 10:129–160, 1976.
- [104] M. D. Feit, J. A. Fleck, and A. Steiger. Solution of the Schroedinger equation by a spectral method. *Journal of Computational Physics*, 47(3):412–433, 1982.
- [105] T. N. Truong, J. J. Tanner, P. Bala, J. A. Mccammon, D. J. Kouri, B. Lesyng, and D. K. Hoffman. A comparative study of time dependent quantum mechanical wave packet evolution methods. *Journal of Chemical Physics*, 96(3):2077–2084, 1992.
- [106] A. Walther, F. Ziesel, T. Ruster, S. T. Dawkins, K. Ott, M. Hettrich, K. Singer, F. Schmidt-Kaler, and U. Poschinger. Controlling fast transport of cold trapped ions. *Physical Review Letters*, 109(8):1–5, 2012.
- [107] R. Bowler, J. Gaebler, Y. Lin, T. R. Tan, D. Hanneke, J. D. Jost, J. P. Home, D. Leibfried, and D. J. Wineland. Coherent diabatic ion transport and separation in a multizone trap array. *Physical Review Letters*, 109(8):1–4, 2012.
- [108] H. Kaufmann, T. Ruster, C. T. Schmiegelow, M. A. Luda, V. Kaushal, J. Schulz, D. Von Lindenfels, F. Schmidt-Kaler, and U. G. Poschinger.

- Fast ion swapping for quantum-information processing. *Physical Review A*, 95(5):1–9, 2017.
- [109] C. Robens, W. Alt, C. Emary, D. Meschede, and A. Alberti. Atomic ”bomb testing”: The Elitzur-Vaidman experiment violates the Leggett-Garg inequality. *Exploring the World with the Laser: Dedicated to Theodor Hänsch on his 75th Birthday*, 123(1):141–157, 2018.
 - [110] C. Robens, S. Brakhane, D. Meschede, and A. Alberti. Quantum Walks with Neutral Atoms: Quantum Interference Effects of One and Two Particles. *Proceedings of the XXII International Conference ICOLS*, 2015.
 - [111] S. E. Sklarz and D. J. Tannor. Loading a Bose-Einstein condensate onto an optical lattice: An application of optimal control theory to the nonlinear Schrödinger equation. *Physical Review A*, 66(5):053619, 2002.
 - [112] N. Khaneja, T. Reiss, C. Kehlet, T. Schulte-Herbrüggen, and S. J. Glaser. Optimal control of coupled spin dynamics: Design of NMR pulse sequences by gradient ascent algorithms. *Journal of Magnetic Resonance*, 172(2):296–305, 2005.
 - [113] T. Caneva, T. Calarco, and S. Montangero. Chopped random-basis quantum optimization. *Physical Review A - Atomic, Molecular, and Optical Physics*, 84(2), 2011.
 - [114] A. Negretti, C. Robens, D. Meschede, T. Calarco, and A. Alberti. Optimal and fast transport control for coherent splitting of trapped atoms. *In preparation*, 2018.
 - [115] F. Platzer, F. Mintert, and A. Buchleitner. Optimal dynamic control of many-body entanglement. *Physical Review Letters*, 105(2):1–4, 2010.
 - [116] H. A. Rabitz, M. M. Hsieh, and C.M. Rosenthal. Quantum Optimally Controlled Transition Landscapes. *Science*, 303(5666):1998–2001, 2004.
 - [117] N. Rach, M. M. Müller, T. Calarco, and S. Montangero. Dressing the chopped-random-basis optimization: A bandwidth-limited access to the trap-free landscape. *Physical Review A*, 92(6):1–8, 2015.
 - [118] M. Werninghaus. Copy of Controlling atom transport in a two-dimensional state-dependent optical lattice, 2017. Master thesis, University of Bonn.
 - [119] S. Rosi, A. Bernard, N. Fabbri, L. Fallani, C. Fort, M. Inguscio, T. Calarco, and S. Montangero. Fast closed-loop optimal control of ultracold atoms in an

- optical lattice. *Physical Review A - Atomic, Molecular, and Optical Physics*, 88(2):1–5, 2013.
- [120] S. Deffner and S. Campbell. Quantum speed limits: From Heisenberg’s uncertainty principle to optimal quantum control. *Journal of Physics A: Mathematical and Theoretical*, 50(45), 2017.
- [121] L. Mandelstam and I. Tamm. The uncertainty relation between energy and time in nonrelativistic quantum mechanics. *J. Phys. (USSR)*, 9:249–254, 1945.
- [122] S. Lloyd. Ultimate physical limits to computation. *Nature*, 406(6799):1047–1054, 2000.
- [123] J. D. Bekenstein. Energy cost of information transfer. *Physical Review Letters*, 46(10):623–626, 1981.
- [124] M. M. Taddei, B. M. Escher, L. Davidovich, and R. L. De Matos Filho. Quantum speed limit for physical processes. *Physical Review Letters*, 110(5):1–5, 2013.
- [125] A. Del Campo, I. L. Egusquiza, M. B. Plenio, and S. F. Huelga. Quantum speed limits in open system dynamics. *Physical Review Letters*, 110(5), 2013.
- [126] S. Deffner and E. Lutz. Quantum speed limit for non-Markovian dynamics. *Physical Review Letters*, 111(1):1–5, 2013.
- [127] T. Caneva, M. Murphy, T. Calarco, R. Fazio, S. Montangero, V. Giovannetti, and G. E. Santoro. Optimal control at the quantum speed limit. *Physical Review Letters*, 103(24):5–8, 2009.
- [128] S. Deffner and E. Lutz. Energy-time uncertainty relation for driven quantum systems. *Journal of Physics A: Mathematical and Theoretical*, 46(33):1–10, 2013.
- [129] O. Andersson and H. Heydari. Quantum speed limits and optimal Hamiltonians for driven systems in mixed states. *Journal of Physics A: Mathematical and Theoretical*, (21):1–15, 2014.
- [130] S. Van Frank, M. Bonneau, J. Schmiedmayer, S. Hild, C. Gross, M. Cheneau, I. Bloch, T. Pichler, A. Negretti, T. Calarco, and S. Montangero. Optimal control of complex atomic quantum systems. *Scientific Reports*, 6:1–12, 2016.

- [131] B. Lekitsch, S. Weidt, A. G. Fowler, K. Mølmer, S. J. Devitt, C. Wunderlich, and W. K. Hensinger. Blueprint for a microwave trapped-ion quantum computer. *Science Advances*, 3(2):1–12, 2017.
- [132] D. Leibfried, E. Knill, S. Seidelin, J. Britton, R. B. Blakestad, J. Chiaverini, D. B. Hume, W. M. Itano, J. D. Jost, C. Langer, R. Ozeri, R. Reichle, and D. J. Wineland. Creation of a six-atom ‘Schrödinger cat’ state. *Nature*, 438(7068):639–642, 2005.
- [133] J. Chiaverini, D. Leibfried, T. Schaetz, M. D. Barrett, R. B. Blakestad, J. Britton, W. M. Itano, J. D. Jost, E. Knill, C. Langer, R. Ozeri, and D. J. Wineland. Realization of quantum error correction. *Nature*, 432(7017):602–605, 2004.
- [134] D. Kielpinski, C. Monroe, and D. J. Wineland. Architecture for a large-scale ion-trap quantum computer. *Nature*, 417(6890):709–711, 2002.
- [135] C. Monroe and J. Kim. Scaling the Ion Trap Quantum Processor. *Science*, 339(6124):1164, 2013.
- [136] C. A. Sackett, D. Kielpinski, B. E. King, C. Langer, V. Meyer, C. J. Myatt, M. Rowe, Q. A. Turchette, W. M. Itano, D. J. Wineland, and C. Monroe. Experimental entanglement of four particles. *Nature*, 404(6775):256–259, 2000.
- [137] B. E. King, C. S. Wood, C. J. Myatt, Q. A. Turchette, D. Leibfried, W. M. Itano, C. Monroe, and D. J. Wineland. Cooling the collective motion of trapped ions to initialize a quantum register. *Physical Review Letters*, 81(7):1525–1528, 1998.
- [138] D. Chen, H. Zhang, X. Xu, T. Li, and Y. Wang. Nonadiabatic transport of cold atoms in a magnetic quadrupole potential. *Applied Physics Letters*, 96(13):1–4, 2010.
- [139] D. P. Pires, M. Cianciaruso, L. C. Céleri, G. Adesso, and D. O. Soares-Pinto. Generalized geometric quantum speed limits. *Physical Review X*, 6(2):1–19, 2016.
- [140] L. B. Levitin and T. Toffoli. Fundamental limit on the rate of quantum dynamics: The unified bound is tight. *Physical Review Letters*, 103(16):1–4, 2009.
- [141] J. Uffink. The rate of evolution of a quantum state . *American Journal of Physics*, 61(10):935, 1993.

- [142] N. Margolus and L. B. Levitin. The maximum speed of dynamical evolution. *Physica D*, 120:188–195, 1998.
- [143] G. H. Wannier. The structure of electronic excitation levels in insulating crystals. *Physical Review*, 52(3):191–197, 1937.
- [144] K. Busch, S. F. Mingaleev, A. Garcia-Martin, M. Schillinger, and D. Hermann. The Wannier function approach to photonic crystal. *Journal of Physics: Condensed Matter*, 1233, 2003.
- [145] D. M. Whittaker and M. P. Croucher. Maximally localized Wannier functions for photonic lattices. *Physical Review B - Condensed Matter and Materials Physics*, 67(8):1–6, 2003.
- [146] B. Vaucher, S. R. Clark, U. Dorner, and D. Jaksch. Fast initialization of a high-fidelity quantum register using optical superlattices. *New Journal of Physics*, 9, 2007.

PUBLICATIONS

- R. Reimann, W. Alt, T. Kampschulte, T. Macha, L. Ratschbacher, N. Thau, S. Yoon, D. Meschede, Cavity-Modified Super- and Subradiant Rayleigh Scattering of Two Atoms. *Physical Review Letters* 114, 023601 (2015)
- R. Reimann, W. Alt, T. Macha, D. Meschede, N. Thau, S. Yoon, L. Ratschbacher, Carrier-free Raman manipulation of trapped neutral atoms. *New Journal of Physics* 16, 113042 (2014)

ACKNOWLEDGMENTS

Eine aufregende und spannende Zeit, in der ich viel erlebt und gelernt habe, geht dem Ende zu. Ich möchte denen danken, die mich in dieser Zeit unterstützt haben, herzlich danken.

Prof. Meschede hat mir die Möglichkeit gegeben, an zwei grandiosen, teils sehr unterschiedlichen Experimenten zu promovieren. Insbesondere möchte ich mich für seine Unterstützung in entscheidenden Situationen und die Förderungsmöglichkeiten, auch über die Universität Bonn hinaus, bedanken. Mein Dank gilt außerdem Priv-Doz. Elisabeth Soergel für die Übernahme der Korreferats, sowie Prof. Calarco und Prof. Vöhringer als drittes und viertes Mitglied meiner Prüfungskommission.

Mein besondere Dank geht an meine Laborteams, mit denen ich immer gerne zusammen gearbeitet habe. Auf der Cavity Seite möchte ich mich bei meinen Laborpartnern Tobias Macha, Rene Reimann und Soekchan Yoon bedanken. Die unzähligen Stunden im Labor wurden aufgrund der vielen unterhaltsamen Gespräche physikalischer und privater Natur nie langweilig. Die Post-Docs Marcel Spurny und Lothar Ratschbacher standen mir in der Zeit zusätzlich immer mit Rat und Tat zur Seite. Auf der Quantenwalk Seite bedanke ich mich bei meinen Laborpartnern Carsten Robens, Manolo Rivera und Thorsten Groh. Carsten hat trotz des Schreibens seiner Arbeit immer Zeit gefunden, mich in das Experiment einzuweisen und mit vielen konstruktiven Diskussionen Herausforderungen des Experiments zu meistern. Manolo kam gegen Ende meiner Doktorarbeit dazu und war mir sehr schnell eine große Hilfe im Labor. Ihm wünsche ich noch eine erfolgreiche und schöne Zeit seiner Doktorarbeit an diesem Experiment. Thorsten hat das Team perfekt mit seiner Programmierfähigkeit und theoretischem Wissen ergänzt. Besonders möchte ich mich bei meinem Post-Doc Andrea Alberti bedanken, der mich mit seinen unendlichen theoretischen und experimentellen Wissen zum Experiment und seinen Matlab Fähigkeiten optimal unterstützt hat und einen wertvollen Beitrag zu allen Teilen meiner Arbeit leistete. Laborübergreifend möchte ich mich auch bei Wolfgang Alt bedanken, der mich zu jedem physikalischen Problem immer mit seinem unglaublichen Wissensschatz beraten konnte. Ich möchte mich natürlich auch bei den hilfsbereiten Kollegen der anderen Labore bedanken, mit denen ich mich immer über Probleme austauschen konnte.

Außerdem bekam ich viel Unterstützung beim Korrekturlesen meiner Arbeit, wofür ich mich sehr bedanken möchte bei Carsten, Manolo, Thorsten, Wolfgang und Andrea sowie Muhammad Sajid, Miguel Martinez-Dorantes, Stefan Brakhane und besonders meinem Mann Manuel Peter.

Des weiteren möchte ich mich bei der Elektronik- und Feinmechanikwerkstatt, sowie unseren organisatorischen Helferlein im dritten Stock, Annelise Miglo, Fien Latumahina und Dr. Dietmar Haubrich für ihre tolle Unterstützung bedanken.

Genauso wichtig ist die Unterstützung außerhalb des Physik. Mein besonderer Dank gilt da natürlich meinen Eltern, die mir in jeder Lage zur Seite gestanden haben und viel Kraft geschenkt haben. Mein größter Dank gilt meinem Mann, der mich nicht nur als Physiker bei meiner Arbeit begleitet hat, sondern insbesondere als Lebensgefährte die größte Stütze in meinem Leben ist. Er hat mich in schwierigen Situation immer geduldig aufgefangen und die richtigen Worte gefunden, um mich wieder zu motivieren. Genauso ist er auch in schönen Situation der wichtigste Mensch, mit dem ich mich über meine Erfolge freuen möchte.

LEBENS LAUF

NATALIE PETER GEB. THAU

geboren am 03. Dezember 1987
in Wiesbaden-Dotzheim
Familienstand verheiratet
Staatsangehörigkeit deutsch
wohnhaf t Pariser Str. 49a
53117 Bonn

AUSBILDUNG

1994-1995 Johannes-Maaß-Grundschule in Wiesbaden
1995-1998 Grundschule Nierstein
1998-2007 Gymnasium zu St. Katharinen in Oppenheim
Abschluss **Allgemeine Hochschulreife (1,8)**
2007 Physikstudium an der Gutenberg-Universität in Mainz
2007-2010 Physikstudium an der Rheinischen Friedrich-Wilhelms-Universität Bonn
Juli 2010 Bachelorarbeit: *Messung des mikroskopischen Tastverhältnisses an der Beschleunigeranlage ELSA*
September 2010 Abschluss **Bachelor of Science (B.Sc.) (2,3)**
2010-2012 Physikstudium an der Rheinischen Friedrich-Wilhelms-Universität Bonn
Oktober 2012 Masterarbeit: *Optical fiber cavity*
Januar 2013 Abschluss **Master of Science (M.Sc.) (1,4)**
2012-2018 Promotionsstudium an der Rheinischen Friedrich-Wilhelms-Universität Bonn

FÖRDERUNG

2014-2016 Stipendiat der Bonn-Cologne Graduate School of Physics and Astronomy